Ozone Chemistry in the Lower Stratosphere: Drivers, Trends, and Impacts

by

Catherine A. Wilka

B.A., Pomona College (2012)

Submitted to the Department of Earth, Atmospheric and Planetary Sciences
in partial fulfillment of the requirements for the degree of

Doctor of Philosophy in Climate Science

at the

MASSACHUSETTS INSTITUTE OF TECHNOLOGY

June 2021

Author .....
Department of Earth, Atmospheric and Planetary Sciences
May 11, 2021

Certified by .....
Susan Solomon
Lee and Geraldine Martin Professor of Environmental Studies
Thesis Supervisor

Accepted by .....
Robert D. van der Hilst
Schlumberger Professor of Earth and Planetary Sciences
Head of Department of Earth, Atmospheric, and Planetary Sciences

Ozone Chemistry in the Lower Stratosphere: Drivers, Trends, and Impacts

by

Catherine A. Wilka

Submitted to the Department of Earth, Atmospheric and Planetary Sciences
on May 11, 2021, in partial fulfillment of the
requirements for the degree of
Doctor of Philosophy in Climate Science

Abstract

This thesis seeks to improve our understanding of the connections between and the modulations of anthropogenically driven chemical changes in the stratosphere by natural processes. It probes these questions on timescales that range from daily to decadal and on spatial scales ranging from a few kilometers to the global mean, and presents new results improving our understanding of both the chemistry and physics behind these processes and improvements to our ability to represent them in chemistry-climate models. This work is driven by the belief that improved understanding of the fundamentals of stratospheric chemical and physical processes can simultaneously advance science and help society in evaluating past policy decisions and informing future ones.

First, the impact of large and moderate sized volcanic eruptions on anthropogenically driven ozone depletion and recovery trends is explored. Results confirm previous work showing that large volcanic eruptions increased the rate of ozone depletion prior to the mid-1990s, and for the first time quantify how the combination of an unusually volcanically quiescent period from the mid-1990s to the mid-2000s and a flurry of moderate sized volcanic eruptions after the mid-2000s decreased the rate of ozone recovery until at least 2014. This study is the first to show that the timing of moderate sized volcanic eruptions, not just large ones, can significantly alter ozone decadal trends.

Second, the ability of equatorial dynamical flows known as Matsuno–Gill patterns to alter stratospheric chemistry is investigated in the deep tropics for months in the spring and fall for the first time. Results from a chemistry-climate model show these anticyclonic flows both entrain extratropical chlorine and induce cooling, allowing rapid heterogeneous chlorine activation on sulfuric acid aerosols. Perturbations to ClO and NO_2 provide a testable signature for the presence of this activation. This study shows a previously unrecognized mechanism in near-equinox months for dynamical influences on the spatial structures of atmospheric composition changes in the deep tropics.

Third, the success of the Montreal Protocol on Substances that Deplete the Ozone

Layer is examined in the context of the record Arctic ozone depletion of Spring 2020. Results indicate that, in a "World Avoided" where ozone depleting substances had continued to increase, the first true Arctic ozone hole would have occurred in Spring 2020 due to the combined effects of higher chlorine and extreme meteorological conditions, and ozone depletion would have begun earlier and lasted longer than seen in the real world. This study also presents an improved parameterization of polar stratospheric cloud impacts on denitrification for the Whole Atmosphere Community Climate Model v.6 (WACCM6), which was necessary to accurately simulate extreme ozone loss.

Fourth, the importance of temperature perturbations from sub-grid scale gravity waves on chemical rates in WACCM6 is explicitly investigated for the first time via a new connection between the orographic gravity wave parameterization and the chemistry module. Results indicate that several key heterogeneous reaction rates proceed faster on average and that this can have a significant effect on monthly chemistry concentrations. The lifetime of PAN also changes in some areas, affecting the distance this tropospheric pollutant can be transported. Verification of temperature perturbations using the COSMIC satellite array is investigated, and preliminary results show generally good agreement when gravity waves' vertical wavelengths are expected to be small. This study reinforces the importance of accounting for sub-grid scale temperature effects when simulating chemistry.

Finally, some directions for future work are discussed, including continued improvements to the denitrification parameterization in WACCM and preliminary efforts to observe tropical heterogeneous chlorine activation using satellites.

Thesis Supervisor: Susan Solomon
Title: Lee and Geraldine Martin Professor of Environmental Studies

Acknowledgments

All we have to decide is what to do with the time that is given to us.
~ JRR Tolkien

This doctoral thesis has been many things. It has been a labor of love; my job for nearly six years; the product of long days and nights of study; and not a little blood, sweat, and tears. (Well, as a computational theorist, I must swap "blood" for "burns" received from over-taxed laptops.) It is the culmination of my decision to pursue a career that benefits both science and the world in which I live. The finest researcher in the world could not hope to make a full tally of every person who has contributed to my journey, from teachers who gave me a boost into science decades ago to briefly-encountered Camberville residents who gave me a thumbs up in the middle of a trying year.

To my advisor, Susan Solomon, thank you for being a role model, mentor, and fantastic teacher in addition to an amazing advisor. It has been an honor and a privilege to learn from and work with you, and I will forever value your insight into both scientific research and the policy that comes of it. Thank you for giving a jet-lagged prospective student stumbling through the 2015 Snowpocalypse the "hard sell" to come to MIT.

I am deeply grateful for the guidance and advice of the other three members of my thesis committee. Thank you to my second generals' advisor and thesis committee member Tim Cronin for your mentorship over the past several years and for your insights into both tropical dynamics and marathon training. Thank you to Colette Heald for making sure I didn't forget about tropospheric chemistry and for fascinating discussions about wildfire aerosols, and of course for handling the logistics of my virtual defense. Thank you to Qiang Fu for invaluable insights into stratospheric dynamics, for always showing me how to look at my research from a new perspective, and for being excited about every project without fail.

I am also thankful to all of the EAPS faculty I have had the chance to learn from both in and out of the classroom. Thank you especially to Noelle Selin for discussions about science policy and the sometimes grim, sometimes hilarious ways it can succeed or fail in the real world. Thank you so much to all of the staff in EAPS that keep the department running, especially Megan Jordan, Maggie Cedarstrom, and Brandon Milardo in HQ. Roberta Allard and Kayla Bauer, it is no exaggeration to say that I would have been completely lost without you two. Immense thanks goes out to all of my colleagues, collaborators, and coauthors beyond MIT throughout this thesis. Thank you especially to Doug Kinnison, Rolando Garcia, David Tarasick, Mike Mills, and Anja Schmidt for your help with the WACCM model, data analysis, and for always making my writing better.

Without funding, I would not have been able to do a PhD. I would like to acknowledge and thank the National Science Foundation for supporting my research through Grants 1539972 and 1906719 from the Atmospheric Chemistry division, the donors who endowed the EAPS Kerr, Shrock, Carlson, Warren Klein, Norman Rasmussen, and Neil & Anna Rasmussen Departmental Fellowships, and an anonymous donor

who helped fund my Arctic work. Thank you to the Houghton fund for allowing me to travel to international conferences to present my work, and thank you to Angela Ellis, Christine Maglio, and Daisy Caban for helping me with fellowship and funding logistics.

My fellow group members and friends at MIT are part of what made this journey possible. Thank you to every member of the Solomon group, past and present, especially Megan for being a great officemate for five years and a great water polo teammate. Thank you to the other members of my year in PAOC, especially Rohini, Margaret, Charles, Martin, Madeline, Mara, and Mukund. Thank you to the EAPS students who came before me who served as mentors and friends, especially Michael McClellan for after-softball talks at the Muddy Charles and Marianna Linz for helping me to believe I could actually do this thing. Thank you to the crEAPS water polo and softball teams for several unbeatable (if not unbeaten) seasons, especially the one where we won the championship by virtue of having the fewest game cancellations. Thank you to the leaders of ESAC, TIDE, and WiXII, and to all who have worked to make EAPS a better and more inclusive place over the years. Finally, thank you to the Zoom & Loom crowd, especially Mary, Tajana, Clara, and Zahra, for being a bright spot every week in the long stretch of the pandemic.

I am forever grateful to my family and friends who have supported me and cheered me on since long before I set foot in the Green Building. Mom and Dad, thank you for more than I can ever express. Thank you for the endless love and support; for emergency cooking advice and last-minute grammar consultations; for always being enthusiastic about my research no matter how far it is from lawyering. Matt and Chrissy, thank you for being amazing older siblings who make me laugh and remind me not to take anything too seriously, including myself. Elyse, you are also my sister in every way that truly matters: I am so, so excited that we've both ended up scientists. To my partner, Ashe, you have supported me for a decade and been at times the only saving grace of an absolutely insane final year that combined a global pandemic, teetering democracy, and somehow summarizing all I've learned in graduate school in a nearly 200 page document. I will forever be grateful that you are part of my life.

Finally, continuing a tradition I have kept since I was old enough to write acknowledgements, thank you to all of the four-legged friends who have kept me (mostly) sane these past few years, especially Berúthiel, Eraser, and Soldier.

Contents

THIS PAGE INTENTIONALLY LEFT BLANK

List of Figures

List of Tables

THIS PAGE INTENTIONALLY LEFT BLANK

Chapter 1

Introduction

1.1 The Ozone Layer in Our Atmosphere

We spend the vast majority of our lives on Earth in the troposphere, the lowermost layer of the atmosphere that contains 90% of the atmosphere by mass and most of the phenomena we term "weather," and only venture outside it during the occasional aircraft flight. Yet the relatively quiescent layer above, the stratosphere, contains an essential ingredient of our continued existence: the ozone layer, a protective shield of O_3 molecules concentrated between approximately 15 km and 35 km above the surface that blocks high energy ultraviolet light from damaging or destroying terrestrial life.

Prior to the mid-20th century, ozone concentrations in the stratosphere were set by a balance of natural production and loss cycles involving odd oxygen (O_x), nitrogen oxides (NO_x), and hydrogen oxides (HO_x). This steady-state chemical cycling was disrupted by the introduction of chlorine and bromine into the stratosphere from the breakdown of chlorofluorocarbons (CFCs). Designed as inert replacements for the noxious refrigerants in use at that time, and subsequently used in building foams, aerosols, and electronic cleaning agents as well, CFC's stability against reaction in the troposphere allows them to transport their halogens high into the stratosphere, where they are finally broken down by high-energy UV radiation.

The chemists Mario Molina and Sherwood Rowland recognized by 1974 that this new source of stratospheric chlorine could pose a threat to the ozone layer (Molina &

Rowland, 1974. Cl and ClO molecules (ClO_x) deplete ozone via gas-phase catalytic cycles:

$$\begin{array}{l} \mathrm{Cl + O_3 \rightarrow ClO + O_2} \\ \mathrm{ClO + O \rightarrow Cl + O_2} \\ \hline \mathrm{O_3 + O \rightarrow 2O_2} \end{array} \qquad \begin{array}{l} \mathrm{2 \times (Cl + O_3 \rightarrow ClO + O_2)} \\ \mathrm{2ClO + M \rightarrow Cl_2O_2 + M} \\ \mathrm{Cl_2O_2 + h\nu \rightarrow Cl + ClO_2} \\ \mathrm{ClO_2 + M \rightarrow Cl + O_2 + M} \\ \hline \mathrm{2O_3 \rightarrow 3O_2} \end{array}$$

As can be seen by the reaction sums, the chlorine molecules are not destroyed but can repeat the cycle over and over, with a single chlorine atom able to destroy up to 100,000 ozone molecules. Bromine operates similarly, but is approximately sixty times more efficient at ozone destruction; thankfully, smaller absolute amounts of bromine were emitted as bromofluorocarbons.

Molina and Rowland's work predicted that ozone depletion would be a slowly but steadily growing problem over the 21st century, with models in the early 1980s estimating future depletion of total ozone of a few to ten percent (Prather et al., 1996). Measurements of extreme springtime ozone depletion over the Antarctic by the Joseph Farman and the British Antarctic Survey in 1985 came as a shock both to the public and to the scientific community. The mechanism behind this deep depletion, which despite the common moniker of ozone "hole" is in fact an extreme thinning of the ozone layer (Figure 1-1), was successfully fingerprinted by Susan Solomon and colleagues in 1986 as resulting from reactions on the surfaces of very cold particles, as described further in the next sections. Partially due to the increased urgency caused by this dramatic discovery, the international community came together to negotiate the Montreal Protocol on Substances that Deplete the Ozone Layer, described by UN Secretary-General Kofi Annan as "perhaps the single most successful international agreement to date." The Montreal Protocol and its subsequent amendments have phased out the production of ozone depleting substances (ODSs), although the long lifetimes of many of these chemicals means that ozone recovery is a slow process, not

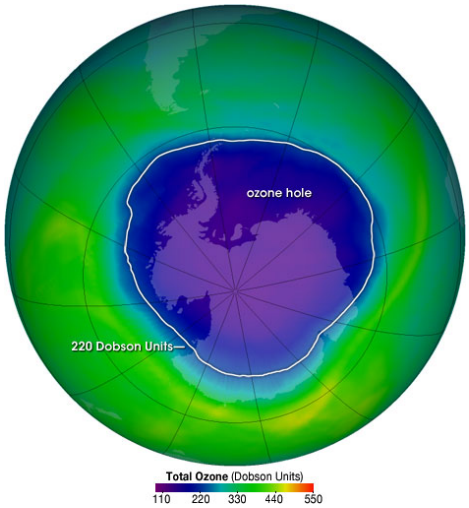

Figure 1-1: NASA's OzoneWatch maps such as this one from October 4th, 2004 are constructed from data using the Ozone Monitoring Instrument aboard the AURA satellite, described further in Chapter 4. Despite technically being a region of extreme thinning rather than a "hole," these striking images are deservedly famous and helped catalyze public support for the Montreal Protocol.

a quick fix, with year-to-year variability from natural processes overlaying the slow healing. Disentangling the signal of ozone recovery from some of these processes is detailed further in Chapters 2 and 4.

1.2 Chlorine in the Stratosphere

The composition of the atmosphere is set by a combination of chemical production and loss processes, and dynamical transport. In the stratosphere, the dominant global circulation is the Brewer-Dobson Circulation (BDC), which is characterized by rising motion in the tropics and sinking at the poles (Brewer, 1949). The BDC transports CFCs from the troposphere to above the ozone layer where, no longer shielded against high-energy ultraviolet light, they photolyze into their constituent components. Once freed from the CFC precursors, most chlorine in the stratosphere enters into the form of reservoir compounds, particularly HCl and $ClONO_2$. The BDC continues to transport these compounds poleward, resulting in concentration gradients that increase with latitude.

Reservoir species of chlorine are incapable of destroying ozone; in order to do so,

chlorine must be converted to "active" chlorine compounds such as ClO and Cl which can participate in catalytic cycles as described in Section 1.1. This process, known as chlorine activation, takes place via heterogeneous reactions on the surfaces of particles (Solomon, 1999 and references therein). The three main activation reactions are:

$$\mathrm{ClONO_2 + HCl \rightarrow Cl_2 + HNO_3} \tag{1.1}$$

$$\mathrm{ClONO_2 + H_2O \rightarrow HOCl + HNO_3} \tag{1.2}$$

$$\mathrm{HOCl + HCl \rightarrow Cl_2 + H_2O} \tag{1.3}$$

These three reactions can take place on multiple types of surfaces, which vary depending on geographic location. At the extremely cold temperatures found near the poles, polar stratospheric clouds (PSCs) are the dominant surface. Type 1 PSCs can be composed of solid nitric acid dihydrate (NAD), trihydrate (NAT), solid sulfuric acid tetrahydryte (SAT), or supercooled liquid ternary solutions of nitric acid, sulfuric acid, and water (STS). Type 2 PSCs are made of water ice, and can only form at temperatures below the frost point. These reactions can also take place on liquid binary solutions of sulfuric acid and water, which are ubiquitous in the lower stratosphere across the globe. Reactions 1.1 – 1.3 on such sulfuric acid aerosols are very dependent on the water content of the particle, allowing them to take place at slightly higher temperatures than traditional PSC reactions.

The rate of a heterogeneous reaction is defined as:

$$R_{rxn} = \frac{1}{4}\gamma n_g \overline{v}_g A_p \tag{1.4}$$

where n_g and $\overline{v}_g$ are the concentration and mean molecular speed, respectively, of the gas-phase species in question, A_p is the available surface area, and γ is the reaction efficiency. The dependency on surface area of equation 1.4 means that the presence of more sulfuric acid aerosol in the stratosphere, such as from a volcanic eruption, will enhance the rates of Reactions 1.1 – 1.3. This is explored in greater depth in

1.3 Modeling Heterogeneous Chemistry

This thesis uses multiple methods to investigate stratospheric chemistry, including radiosondes and ozonesondes which provide high resolution profile measurements and stratosphere-focused satellites which provide more complete spatial and temporal coverage. These observations are compared to those simulated by a general circulation model (GCM). The GCM used for all studies is the Whole Atmosphere Community Climate Model (WACCM), a component of the Community Earth System Model (CESM) run by the National Center for Atmospheric Research. WACCM is a highly regarded model for stratospheric studies and can be run in a range of configurations and with various forcings added or eliminated (Gettelman et al., 2019; Froidevaux et al., 2019). The specific model version and configuration used for each study in this thesis is detailed in Section 2 of each chapter, but as the same heterogeneous reaction parameterization is common to all and of significant importance to the results, some additional details are provided here.

WACCM calculates the reaction efficiencies of Reactions 1.1–1.3 on sulfate aerosols using the Shi et al., 2001 kinetic model. This parameterization approximates the reaction efficiencies in terms of a resistor model:

$$\frac{1}{\gamma} = \frac{1}{\alpha} + \frac{a}{\Gamma_b + \Gamma_s} \tag{1.5}$$

Here α is the mass accommodation coefficient, which determines the likelihood of a gas particle entering into the liquid phase during a collision with the aerosol, and at stratospheric temperatures and pressures can be taken as unity. Γ_b and Γ_s are the uptake coefficients of bulk phase processes and surface reaction, respectively. Reaction 1.3 between HCl and HOCl is solely dependent upon Γ_b, whereas Reactions 1.1 and 1.2 contain a dependency upon Γ_s as well.

A key feature of the reaction efficiencies of Reactions 1.1–1.3 is their strong nonlinearity with temperature. This nonlinearity is the fundamental reason that gravity

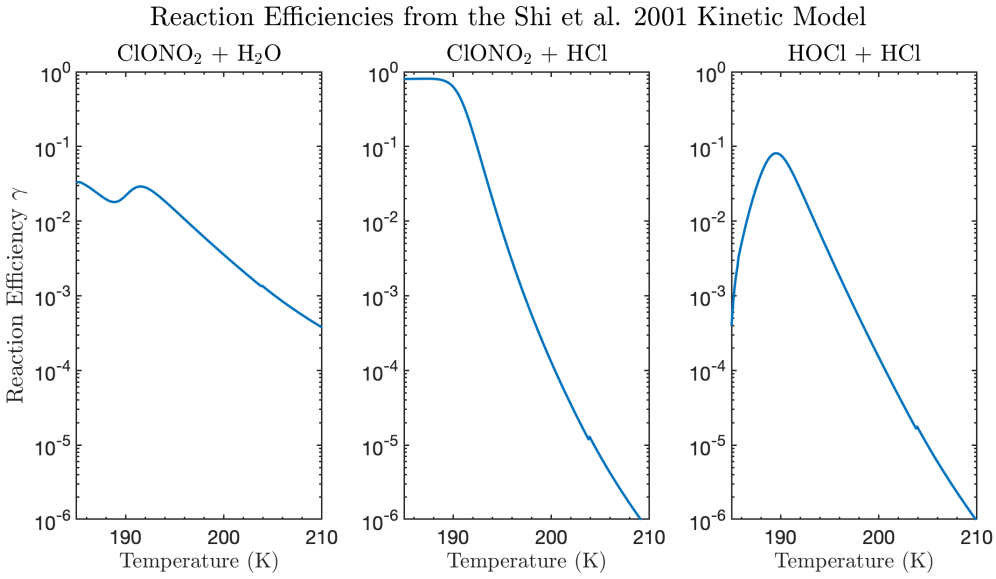

Figure 1-2: Reaction Efficiencies as functions of temperature for Reactions (1-3) using the Shi et al. 2001 kinetic model. Other parameters are: pressure = 55 hPa, aerosol radius = 0.1μm, [H_2O] = 5 ppmv, [HCl] = 150 pptv, [$ClONO_2$] = 50 pptv. Modified from Figure 6 of Shi et al., 2001.

waves are important to heterogeneous chemistry, as detailed further in Chapter 5, and is an important component of reaction rate sensitivity in both the tropics (Chapter 3) and Arctic (Chapter 4). The variation with temperature of these reactions using the Shi et al., 2001 model is shown in Figure 1-2. Note that Reaction 1.1 in particular drops off steeply in likelihood at temperatures above 195 K, and all three reactions diminish to negligible values as temperatures rise above 200 K.

The Shi et al., 2001 model followed in the footsteps of experimental lab work throughout the 1980s and 1990s (Hanson et al., 1994; Tolbert et al., 1998) and extended their findings, but to the author's knowledge it was the last full experimental investigation of these reactions. Stratospheric conditions can be logistically challenging to reproduce in laboratory experiments, and the low temperature end of this parameterization is more poorly constrained than the high end. Given the importance of the rapid change in reaction efficiency at the lowest temperatures (185 K - 195 K), it is important to recognize these uncertainties. In particular, the impact of internal mixing of sulfuric acid aerosols with organics may be important for tropical regions, where polluted air masses from highly populated regions can be lofted into

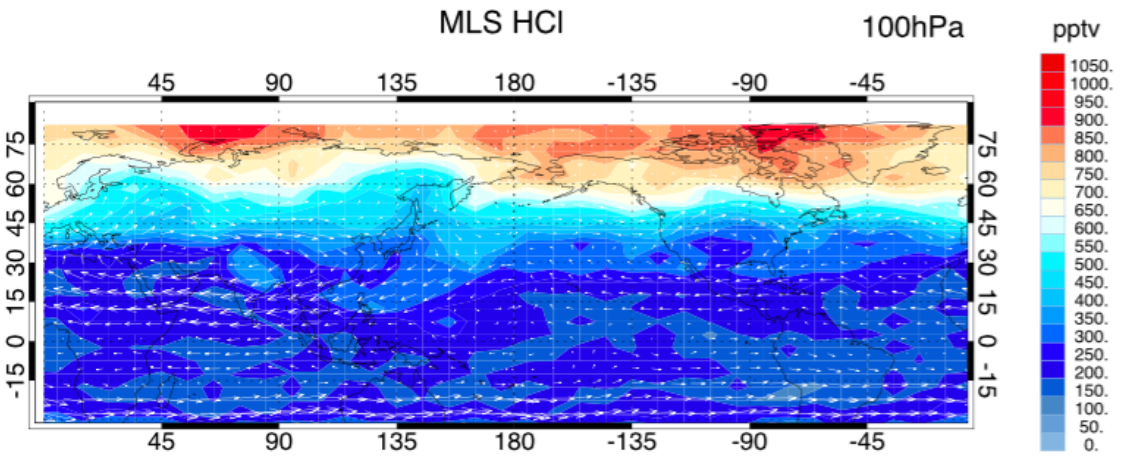

Figure 1-3: Reproduced from Figure 1a of Solomon et al., 2016.

the stratosphere (Randel et al., 2010; Hopfner et al., 2019; Kremser et al., 2016), but laboratory experiments have not yet addressed these impacts for the reactions under consideration and so representation in models is inherently limited.

1.4 Activation in the Monsoon

Until recently, it was thought that heterogeneous chemistry was absent from the tropics and subtropics outside of extreme conditions, such as occurred after the eruption of Mt. Pinatubo, and that all ozone trends near the tropical tropopause were purely due to dynamical effects such as changes in upwelling. This conventional wisdom was changed by the Solomon et al., 2016 study, which is briefly summarized here due to its direct relevance to Chapters 3 and 5. As a coauthor on this work, I analyzed output of SD-WACCM4 runs with and without heterogenous chlorine and bromine chemical reactions present in the tropics to isolate the signature of in situ chlorine activation in $ClONO_2$, and tested the sensitivity of Reactions 1.1–1.3 to perturbations in temperature and water vapor concentrations.

While the lower stratosphere in these regions has long been known to be extremely cold, the only chlorine in the ascending branch of the Brewer-Dobson circulation is still tied up in CFCs. Solomon et al., 2016 recognized that the large anticyclones of

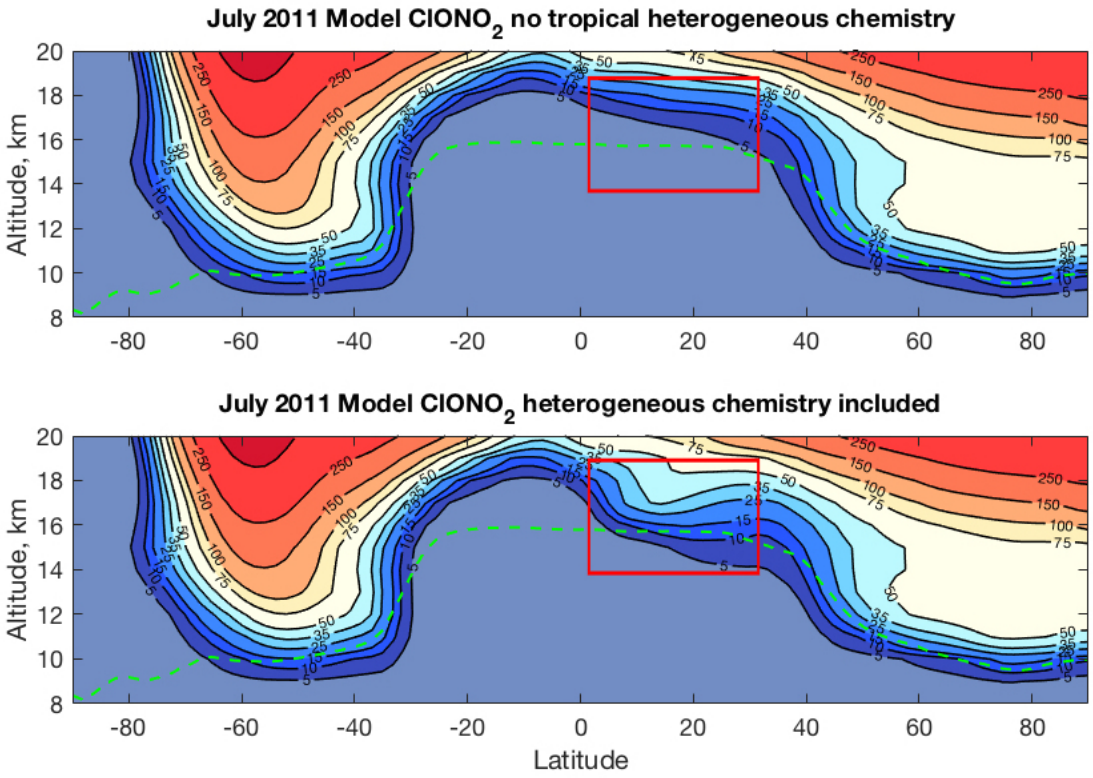

Figure 1-4: Reproduced from Figure 3 of Solomon et al., 2016.

the East Asian Summer Monsoon (EASM) and the North American Monsoon (NAM) might provide a method of transporting reservoir chlorine species such as HCl and $ClONO_2$ from the midlatitudes into the subtropics. As shown in Figure 1-3 (top panel of their Figure 1) by the curling of high levels of HCl around the anticyclonic winds near the EASM and NAM, this can indeed be seen in both satellite observations and model fields (not shown). Further calculations revealed that, at least in the SD-WACCM model, there exists a tongue of enhanced $ClONO_2$ in the monsoon region that vanishes in the absence of heterogeneous chemistry, as shown in Figure 1-4 (their Figure 3). This study represented the first significant demonstration of a signature of in situ chemical activation in the subtropics outside of extremely volcanically-perturbed years, demonstrated that chemical changes might be the cause behind up to a third of the ozone trends in that region, and inspired the study of the deep tropics detailed in Chapter 3.

1.5 Thesis Outline

In this thesis, I examine several important factors driving the rates of heterogeneous chlorine activation reactions and accompanying ozone depletion in the lower stratosphere, including aerosol surface area, dynamical transport of reactants, and wave-driven temperature perturbations. I also consider how anthropogenic trends can seem to vary due to natural variability, such as stochastically timed volcanic eruptions and unusually cold winters, and provide results that disentangle those variations from our continued success in healing the ozone layer via adherence to the Montreal Protocol. More generally, this thesis has improved our knowledge about and our ability to model the chemistry of the stratosphere via new understanding of processes and updated model parameterizations.

In Chapter 2, I examine how the natural variability in the stratospheric sulfate aerosol layer, which determines the surface area available for heterogeneous chlorine activation, impacts anthropogenic ozone trends. In this study I use a suite of WACCM simulations from 1979 to 2014 to show that eruptions increased ozone loss rates over the depletion era from 1980 to 1998 and impeded the recovery rates from 1999 to 2014. My findings show the importance of considering clusters of moderate volcanic eruptions, not just lone large eruptions as has been traditionally considered, in accurately modeling ozone changes. This chapter reinforces the need to carefully account for changing aerosol surface area when attempting to identify the early signs of global ozone recovery.

In Chapter 3, I demonstrate that heterogeneous chlorine activation can occur in the deep tropics in months without monsoons (fall and spring). In this study I systematically track the effects of symmetric Matsuno–Gill circulation patterns on stratospheric chemistry, starting with the latent heating signature in precipitation observations, finding the corresponding diabatic heating signal in reanalysis, and tracing the resulting anticyclonic winds and cold temperature perturbations in the lower stratosphere in WACCM to their impact on chemical rates. I use the difference between runs with and without heterogeneous chemistry to isolate the in situ chemical

activation from transport effects and find that ClO can be enhanced by a factor of ten or more in months with symmetric Matsuno–Gill circulation responses. This chapter's findings expand the regions over which heterogeneous chemistry is known to occur in models and provides a distinct chemical pattern for future aircraft missions to target.

In Chapter 4, I compare the extreme Arctic ozone depletion in the spring of 2020 to a hypothetical world in which ozone depleting substances had continued to increase at mid-1980s rates rather than being successfully regulated by the Montreal Protocol. In this study I find that an Antarctic-style ozone hole would have appeared over the Arctic in a world without the Montreal Protocol (a "World Avoided"), potentially exposing large portions of the Arctic biosphere and population to increased levels of UV radiation. I use both a long-running network of ozonesondes and the WACCM model to show how unusual Spring 2020 already was, and by comparison how much more extreme a World Avoided Spring 2020 would have been. This study has also improved the simulation of denitrification in WACCM for extreme meteorological conditions, resulting in a better match in both nitric acid and ozone concentrations to observations for Spring 2020. This chapter reinforces the conclusion that temporary extreme ozone depletion is not a cause for concern about the Montreal Protocol's effectiveness, but should instead be seen as a glimpse of a grimmer world we successfully avoided.

In Chapter 5, I investigate the impact of temperature perturbations caused by small-scale gravity waves on stratospheric chemistry reaction rates and composition. I present results from a new connection between WACCM's chemistry module and orographic gravity wave parameterization that highlight how nonlinearities in reaction efficiencies can compound over time into large signals. I focus on stratospheric heterogeneous chlorine reactions, but also discuss the potential for changes to troposphere transport of pollutants such as PAN. I finish by discussing ways to verify and improve the derivation of temperature perturbations that are passed to the chemistry. This chapter demonstrates the importance of accurately accounting for small scale temperature perturbations when studying nonlinear chemical reactions, even when it is not possible to simulate the perturbations directly within the resolution of a model.

Finally, in Chapter 6, I consider some direction for future work, with a dual focus on how to refine the new denitrification parameterization in WACCM and on how we might observe tropical heterogeneous chemistry.

THIS PAGE INTENTIONALLY LEFT BLANK

References

[1] Brewer, A. W. (1949). Evidence for a world circulation provided by the measurements of helium and water vapour distribution in the stratosphere. *Quarterly Journal of the Royal Meteorological Society, 75*(326), 351–363. https://doi.org/10.1002/qj.49707532603

[2] Farman, J. C., Gardiner, B. G., & Shanklin, J. D. (1985). Large losses of total ozone in Antarctica reveal seasonal ClO_x/NO_x interaction. *Nature, 315*(6016), 207–210. https://doi.org/10.1038/315207a0

[3] Froidevaux, L., Kinnison, D. E., Wang, R., Anderson, J., & Fuller, R. A. (2019). Evaluation of CESM1 (WACCM) free-running and specified dynamics atmospheric composition simulations using global multispecies satellite data records. *Atmospheric Chemistry and Physics, 19*(7), 4783–4821. https://doi.org/10.5194/acp-19-4783-2019

[4] Gettelman, A., Mills, M. J., Kinnison, D. E., Garcia, R. R., Smith, A. K., Marsh, D. R., ... & Randel, W. J. (2019). The whole atmosphere community climate model version 6 (WACCM6). *Journal of Geophysical Research: Atmospheres, 124*(23), 12380–12403.https://doi.org/10.1029/2019JD030943

[5] Hanson, D. R., Ravishankara, A. R., & Solomon, S. (1994). Heterogeneous reactions in sulfuric acid aerosols: A framework for model calculations. *Journal of Geophysical Research: Atmospheres, 99*(D2), 3615–3629. https://doi.org/10.1029/93JD02932

[6] Höpfner, M., Ungermann, J., Borrmann, S., Wagner, R., Spang, R., Riese, M., ... & Wohltmann, I. (2019). Ammonium nitrate particles formed in upper troposphere from ground ammonia sources during Asian monsoons. *Nature Geoscience, 12*(8), 608–612. https://doi.org/10.1038/s41561-019-0385-8

[7] Kremser, S., Thomason, L. W., von Hobe, M., Hermann, M., Deshler, T., Timmreck, C., ... & Meland, B. (2016). Stratospheric aerosol — Observations, processes, and impact on climate. *Reviews of Geophysics, 54*(2), 278–335. https://doi.org/10.1002/2015RG000511

[8] Molina, M. J., & Rowland, F. S. (1974). Stratospheric sink for chlorofluoromethanes: Chlorine atom-catalysed destruction of ozone. *Nature, 249*(5460), 810–812. https://doi.org/10.1038/249810a0

[9] Prather, M., Midgley, P., Rowland, F. S., & Stolarski, R. (1996). The ozone layer: The road not taken. *Nature, 381*(6583), 551–554. https://doi.org/10.1038/381551a0

[10] Randel, W. J., Park, M., Emmons, L., Kinnison, D., Bernath, P., Walker, K. A., ... & Pumphrey, H. (2010). Asian monsoon transport of pollution to the stratosphere. *Science, 328*(5978), 611–613. https://doi.org/10.1126/science.1182274

[11] Shi, Q., Jayne, J. T., Kolb, C. E., Worsnop, D. R., & Davidovits, P. (2001). Kinetic model for reaction of $ClONO_2$ with H_2O and HCl and HOCl with HCl in sulfuric acid solutions. *Journal of Geophysical Research: Atmospheres, 106*(D20), 24259–24274. https://doi.org/10.1029/2000JD000181

[12] Solomon, S. (1999). Stratospheric ozone depletion: A review of concepts and history. *Reviews of Geophysics, 37*(3), 275–316. https://doi.org/10.1029/1999RG900008

[13] Solomon, S., Garcia, R. R., Rowland, F. S., & Wuebbles, D. J. (1986). On the depletion of Antarctic ozone. *Nature, 321*(6072), 755–758. https://doi.org/10.1038/321755a0

[14] Solomon, S., Kinnison, D., Garcia, R. R., Bandoro, J., Mills, M., Wilka, C., ... & Höpfner, M. (2016). Monsoon circulations and tropical heterogeneous chlorine chemistry in the stratosphere. *Geophysical Research Letters, 43*(24), 12–624. https://doi.org/10.1002/2016GL071778

[15] Tolbert, M. A., Rossi, M. J., & Golden, D. M. (1988). Heterogeneous interactions of chlorine nitrate, hydrogen chloride, and nitric acid with sulfuric acid surfaces at stratospheric temperatures. *Geophysical Research Letters, 15*(8), 847–850. https://doi.org/10.1029/GL015i008p00847

Chapter 2

On the Role of Heterogeneous Chemistry in Ozone Depletion and Recovery

Abstract

We demonstrate that identification of stratospheric ozone changes attributable to ozone depleting substances and actions taken under the Montreal Protocol requires evaluation of confounding influences from volcanic eruptions. Using a state-of-the-art chemistry-climate model, we show that increased stratospheric aerosol loading from volcanic eruptions after 2004 impeded the rate of ozone recovery post-2000. In contrast, eruptions increased ozone loss rates over the depletion era from 1980 to 1998. We also present calculations without any aerosol chemistry to isolate contributions from gas-phase chemistry alone. While the impact of large-scale volcanic eruptions on ozone depletion is well documented, this study demonstrates the importance of also considering moderate sized volcanos, and quantifies for the first time how statistical recovery trends in the SD-WACCM model are impacted by such previously-overlooked eruptions. This study reinforces the need for accurate information regarding strato-

This chapter was published in *Geophysical Research Letters* (Wilka et al., 2018). The publication and its supplement are available at `https://doi.org/10.1029/2018GL078596`. Used with permission.

spheric aerosol loading when modeling ozone changes, particularly for the challenging task of accurately identifying the early signs of ozone healing distinct from other sources of variability.

2.1 Introduction

The potential of anthropogenic chlorofluorocarbons to deplete ozone via gas-phase photochemistry was recognized in the 1970s (Molina and Rowland, 1974). This chemistry was expected to cause a small decrease in total ozone by 2100 if chlorofluorocarbon production continued. The urgency of the problem increased dramatically when Antarctic observations showed a sharp, unexpected ozone decline in the 1980s (Farman et al., 1985). Referred to as the ozone hole, this dramatic thinning of the ozone layer is the result of heterogeneous reactions on cold polar stratospheric cloud surfaces that activate chlorine from the reservoir species $ClONO_2$ and HCl to form reactive species capable of catalytic ozone destruction (Solomon et al., 1986). Laboratory studies along with observations of ozone losses following the 1982 El Chichón volcanic eruption prompted examination of heterogeneous processes on liquid sulfuric acid/water aerosols, including the hydrolysis of N_2O_5; this reaction was found to display little temperature sensitivity and to be of importance for the smaller ozone losses occurring in the global lower stratosphere (Hofmann and Solomon, 1989; Rodriguez et al., 1991). Measurements not only of ozone but also of other species including NO and ClO following the 1991 eruptions of Mt. Pinatubo and Cerro Hudson confirmed that the stratospheric sulfuric acid aerosol enhancements from volcanic eruptions can perturb atmospheric composition even under warm conditions at midlatitudes via N_2O_5 hydrolysis (Solomon, 1999, and references therein). Recently, it has been suggested that stratospheric sulfate aerosols can also cause chlorine activation in the tropics, with recent eruptions such as Nabro in 2011 enhancing this effect (Solomon et al., 2016b). Trends are expected to vary based on future stratospheric aerosol burdens in the 21st century (Klobas et al., 2017; Naik et al., 2017).

Concerns about ozone depletion led the world to adopt the Montreal Protocol to phase out ozone depleting substances, and observations do show a decline in HCl from the peak values around the year 2000 (Mahieu et al., 2014; Rinsland et al., 2003), in good agreement with the model used here (Douglass et al., 2014). In accordance with models, observations suggest that ozone recovery is emerging (Chehade et al., 2014; Sofieva et al., 2017; Solomon et al., 2016a), although the significance of trends depends strongly on the magnitude of the background atmospheric variability (Keeble et al., 2018) and varies with latitude and season.

In this paper, we use observations of volcanic sulfur loading together with model calculations to analyze how heterogeneous chemistry has affected ozone trends in both the depletion and recovery eras. The contribution of gas-phase chemistry alone has not been often revisited since the discovery of heterogeneous chemistry in the 1980s, and here we also evaluate gas-phase depletion with a state-of-the-art chemistry-climate model.

2.2 Materials and Methods

2.2.1 Model Description

To examine ozone trends in runs with different forcings we use the Whole Atmosphere Community Climate Model, version 4 (WACCM4). WACCM is a component of the Community Earth System Model, version 1 from the National Center for Atmospheric Research. It is a high-top model with fully interactive gas-phase and heterogeneous chemistry that has been evaluated via multiple comparisons with data and other models (Garcia et al., 2017; Marsh et al., 2013; Solomon et al., 2015; Wegner et al., 2013). It has a spatial resolution of 1.9° by 2.5° latitude-longitude grid with 88 pressure levels up to 140 km. We use the specified dynamics mode in which the model below 50 km is nudged to temperature, wind, and surface pressure fields from the National Aeronautics and Space Administration's Modern-Era Retrospective Analysis for Research and Applications (MERRA) with a relaxation time of 50 hr. The aerosol

microphysics scheme was updated, and the volcanic sulfur emissions are taken from a database of eruptions developed by Neely III and Schmidt (2016), implemented in a modal aerosol model, which compares favorably to available observations for both high and low aerosol loadings (Mills et al., 2016).

We present results that incorporate different forcings to test the relative impacts of (i) our best representation of both background and volcanic aerosols since 1979 (Chem-Dyn-Vol), (ii) background aerosols under volcanically clean conditions (Vol-Clean), (iii) omission of low-latitude heterogeneous chlorine chemistry (NoHet40NS), and (iv) gas-phase chemistry only. We include volcanic aerosols but turn off all heterogeneous chlorine chemistry between 40°N and 40°S in the run labeled NoHet40NS; N_2O_5 hydrolysis is, however, included in this case. Every run includes historical anthropogenic emissions of ozone depleting substances and greenhouse gases and is spun up using a repeating series of the 1979–1982 meteorological fields beginning in 1952 before being nudged to MERRA dynamics beginning in 1979, when the MERRA reanalysis starts; the calculations extend to 2014, based upon availability of consistent MERRA and solar flux input data sets that drive the model.

2.2.2 SBUV and NIWA-BS Total Column Ozone

We compare the total column ozone (TCO) trends simulated by WACCM against observational data from both the Solar Backscatter Ultraviolet (SBUV) MOD v8.6 and the National Institute of Water and Atmospheric Research-Bodeker Scientific (NIWA-BS) data sets for the depletion era of 1979–1998 and the recovery era of 1999–2014. The SBUV data set is derived from multiple backscatter instruments, and the TCO product agrees with ground-based ozone measurements to better than 1% after 1978 (McPeters et al., 2013). NIWA-BS is a merged data set, which incorporates multiple satellite-based measurements, including SBUV, corrected for biases and drifts through comparisons with ground-based spectrophotometer networks (Bodeker et al., 2005).

2.2.3 SWOOSH Vertical Ozone

To examine vertically resolved trends, we use the 2.5° resolution combined product from the Stratospheric Water and OzOne Homogenized (SWOOSH) data set (Davis et al., 2016). The SWOOSH data set begins in 1984, so for all vertically resolved trend analysis we use the period 1984–1998 to represent what we refer to as the SWOOSH depletion era, with the recovery era defined as before. We present the SWOOSH data only as a general point of comparison, recognizing that there are substantial differences in trends among different data sets and the quantification of satellite ozone trends across different data sets is a topic of current research (see, e.g., Steinbrecht et al., 2017).

2.3 Global Trends

We first examine trends in total ozone for both the depletion and recovery eras. The top panel of Figure 2-1 shows model and data time series anomalies over the entire run, and for the depletion and recovery eras in the lower left and right panels, respectively. Figure 2-S1 in the supporting information shows the same for absolute TCO. The comparison of the gas-phase only run to the other cases illustrates the impact of heterogeneous chemistry (note that all runs use the same prescribed MERRA dynamics); however, any dynamical trends along with gas-phase chemistry will influence all the runs (see below). We use a 3-year running mean to smooth the quasi-biennial oscillation (QBO) and other high-frequency variability, then take an average from 60°N to 60°S and zero each time series to its 1998 value before fitting the anomalies in the depletion era and the recovery era separately with a linear least squares model. Volcanic eruptions are indicated by triangles at the bottom of the panels, with the larger triangles indicating eruptions of magnitude 5 and 6 on the Volcanic Explosivity Index scale. Chem-Dyn-Vol shows distinct departures from Vol-Clean during times of increased volcanic aerosol loading. The influence of volcanic eruptions on these long-term (10–20 years) ozone trends depends on their magnitudes and timing. The calculated depletion from Mt. Pinatubo and Cerro Hudson lingers

into the mid-1990s, and those enhanced ozone losses (Chem-Dyn-Vol vs. Vol-Clean in Figure 2-1) toward the end of the depletion era imply steeper depletion over that period. In the recovery era, very low stratospheric aerosol loads characterize the start of the period near 1999, followed by several moderate eruptions after about 2005 (Solomon et al., 2011; Vernier et al., 2011), implying ozone losses in Chem-Dyn-Vol compared to Vol-Clean that flatten trends in the recovery era. The slopes and 95% confidence intervals for linear fits are given in Table 2.1 in Dobson units per year, along with the percentage differences of each trend from Chem-Dyn-Vol. Tables 2-S1 and 2-S2 show the same for the Northern and Southern Hemispheres. Table S3 (available online) lists eruptions that transported SO_2 amounts greater than 0.03 Tg to 10 km or higher.

Figure 2-1 and Table 2.1 show that the evolution of the TCO has been strongly dominated by heterogeneous chemistry. Vol-Clean trends are about 16% less negative than Chem-Dyn-Vol in the depletion era and 52% more positive in the recovery era (Table 2.1), showing how volcanoes have increased the ozone loss in the depletion era and delayed the recovery according to this model. NoHet40NS trends are about 5% less negative than Chem-Dyn-Vol in the depletion era and 12% more positive in the recovery era, showing how heterogeneous chemistry in the tropics and subtropics has also contributed to global trends. Chem-Dyn-Vol, Vol-Clean, and NoHet40NS trends in the depletion era show less depletion but greater variability in the Northern Hemisphere, while in the recovery era these trends show stronger recovery but greater variability in the Southern Hemisphere.

Some ozone trend studies using both observations (Chehade et al., 2014; Weber et al., 2018) and models (Keeble et al., 2018) employ multiple linear regression (MLR) to deal with contributions including the 11-year solar cycle, El Niño–Southern Oscillation, the QBO, and volcanic influences. While MLR can reduce error bars (e.g., by accounting for QBO variability), it generally does not change the magnitude or structure of absolute trends (e.g., Ball et al., 2018). Figure 2-S2 shows SWOOSH trends for the recovery era using a multiple regression including a representation of solar, QBO, El Niño–Southern Oscillation, and aerosol terms (described further

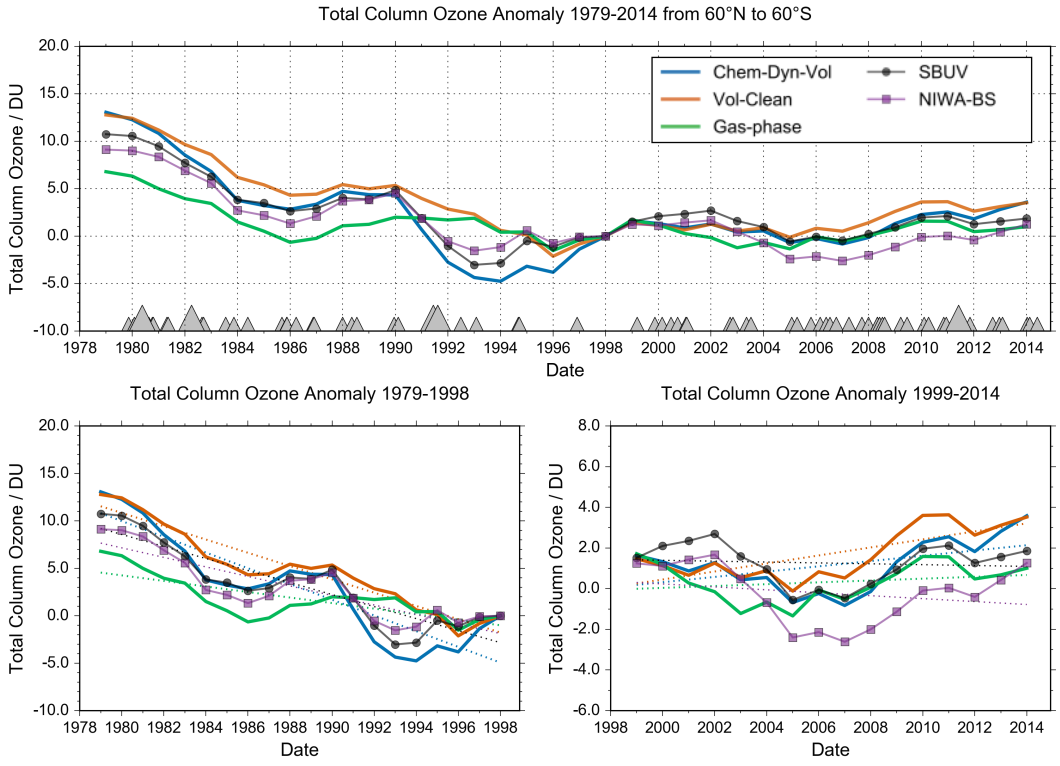

Figure 2-1: **(top)** Time series of 3-year running mean of 60°N–60°S total column ozone anomalies with respect to 1998 values from 1979 to 2014 with gas-phase, Vol-Clean, and Chem-Dyn-Vol runs shown as green, orange, and blue solid lines. Solar Backscatter Ultraviolet and National Institute of Water and Atmospheric Research-Bodeker Scientific total column ozone data are shown by the black line with circles and the purple line with squares, respectively. Gray triangles at the bottom indicate volcanic eruptions, with the larger triangles indicating eruptions of Volcanic Explosivity Index 5 and 6. **(bottom)** Time series of anomalies in global mean total column ozone and their respective linear fits for the (left) depletion era and for the (right) recovery era. Fit parameters are given in Table 2.1.

in Supporting Text 2.6.1; see also Stone et al., 2018), and the differences between Figure 2-S2 and Figure 2-3 (linear regression) are minimal. We note that time lags and relationships between volcanoes and ozone vary in latitude and altitude, impeding identification of a simple regression index such as integrated aerosol columns. Further, it is clear that volcanic aerosols are especially effective for ozone loss under cold conditions, and such temperature-aerosol coupling is not accounted for in simple linear regressions. While it may be possible to formulate a nonlinear and/or mixed-

Table 2.1: Total Column Ozone Trends (Dobson Units/Year) for the Depletion and Recovery Eras and Percentage Differences From Chem-Dyn-Vol for 60°N to 60°S

	1979-1998 (DU per year)	1979-1998 (Δ Chem-Dyn-Vol)	1999-2014 (DU per year)	1999-2014) (Δ Chem-Dyn-Vol)
Chem-Dyn-Vol	-0.829 (-1.030, -0.628)	–	0.130 (-0.005, 0.265)	–
Vol-Clean	-0.700 (-0.806, -0.595)	-15.6%	0.197 (0.097, 0.297)	+51.5%
NoHet40NS	-0.790 (-0.952, -0.627)	-4.7%	0.145 (0.019, 0.270)	+11.5%
Gas-Phase	-0.292 (-0.416, -0.168)	-64.8%	0.045 (-0.068, 0.158)	-65.4%
SBUV	-0.633 (-0.790, -0.477)	-23.6%	-0.021 (-0.141, 0.098)	-116.2%
NIWA-BS	-0.502 (-0.643, -0.361)	-39.4%	-0.072 (-0.243, 0.098)	-155.4%

term regression model that fully accounts for aerosol impacts, in this paper our goal is to assess how aerosols have impacted the raw data, so we have chosen to perform simple linear trends rather than a multiple regression. In addition, quantifying the calculated influence of volcanic aerosols on ozone trends is important for its own sake and can inform studies seeking to account for it using multiple regression methods.

Comparison of the model to the SBUV and NIWA-BS total column time series shows good general agreement. The two observational data sets track each other closely in anomaly space in the depletion era, although Figure 2-S1 shows that NIWA-BS is lower overall, except in the years immediately after Pinatubo. The discrepancy between them may be due to NIWA-BS's prioritization of other instruments over SBUV, particularly its assimilation of Microwave Limb Sounder data beginning in 2004. Both data series display somewhat less depletion from Pinatubo/Hudson than Chem-Dyn-Vol in the early 1990s but more than Vol-Clean or the gas-phase run. Note that the gas-phase run best shows the variations associated with the solar cycle, whose effect maximizes in the upper stratosphere. Trend lines show that the gas-phase-only run fails to capture the trend in the depletion era. While the Chem-Dyn-Vol and Vol-Clean results are closer to the observations, their depletion era trends are somewhat steeper than the data (although only Chem-Dyn-Vol is different at the 95% confidence level).

In the recovery era, both observational data sets suggest trends that display less recovery (positive trends) than the Chem-Dyn-Vol or Vol-Clean means, although Chem-Dyn-Vol is closer to the observations and all overlap at the 95% confidence interval as given in Table 2.1. The NIWA-BS data set shows a deeper negative

anomaly in the mid-2000s than the model and is again lower overall in Figure 2-S1, whereas the SBUV data track Chem-Dyn-Vol closely there. In contrast, both the NIWA-BS and Chem-Dyn-Vol show an uptick of similar magnitude after 2012, whereas the SBUV data set stays mostly flat for the last few years.

2.4 Trends in Latitude and Height

Figures 2-2 and 2-3 show contour plots of linear trends during the SWOOSH depletion (1984–1998) and recovery (1999–2014) eras, respectively. Each figure shows the annual average linear trends for the Chem-Dyn-Vol, Vol-Clean, and gas-phase model runs and the SWOOSH data set. For each panel, the time series has had high-frequency variability removed before trend calculation by applying a 3-year running mean, as in Figure 2-1. Our results are similar to those over nearly the same years based on SAGE II and GOMOS data (Kyrölä et al., 2013, their Figures 13 and 14). Trends are fitted separately at each latitude-pressure point and then expressed as percent per decade relative to the mean of the ozone mixing ratio for each era. Figures 2-S3 and 2-S4 show the differences between the Chem-Dyn-Vol run and the three other runs (Vol-Clean, gas-phase, and NoHet40NS) for the selected depletion and recovery eras, respectively.

Gas-phase chemistry is expected to dominate upper stratospheric changes, and Figure 2-2 shows that observed depletion for pressures lower than 20 hPa broadly agrees with the gas-phase only run (the other simulations are similar since there is no significant heterogeneous chemistry in the upper stratosphere). Turning to the lower stratosphere in Figure 2-2, the greatest depletion occurs in the high-latitude lower stratospheres of both hemispheres where PSCs can form, with the Antarctic showing deeper depletion than the Arctic due to its lower temperatures and more stable polar vortex. Figure 2-2 shows that depletion also extends out through the midlatitudes and into the tropics when heterogeneous chemistry is included in the model. Ozone losses in the tropical lower stratosphere during the depletion era initially came as a surprise (Randel et al., 1999), but in recent years, potential contributions from

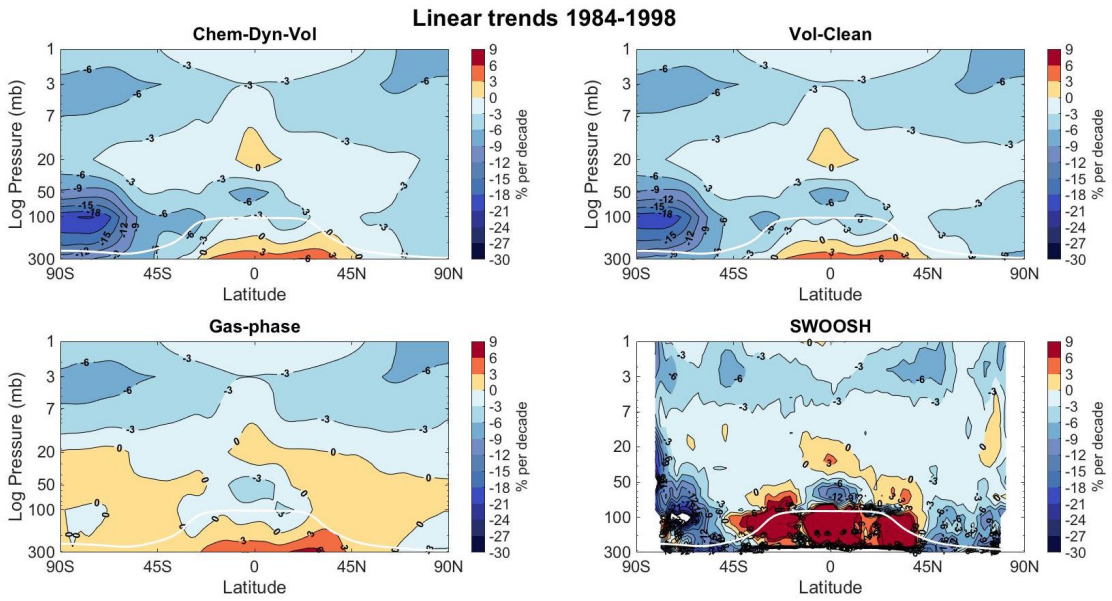

Figure 2-2: Contour plots of linear trends during the SWOOSH depletion era (1984–1998) expressed as percent per decade for the (a) Chem-Dyn-Vol, (b) Vol-Clean, (c) gas-phase runs, and (d) SWOOSH data set. The white line indicates the location of the tropopause in the model. SWOOSH = Stratospheric Water and OzOne Homogenized.

enhanced upwelling as well as chemical drivers have been much discussed (Randel and Thompson, 2011; Solomon, 1999; Solomon et al., 2016b). The patterns of ozone loss in the tropical and subtropical lower stratosphere of the Chem-Dyn-Vol and Vol-Clean runs in Figure 2-2 show that heterogeneous chemistry plays a substantial role in this region according to WACCM; note that the gas-phase case shows ozone decreases near 50 hPa in the deep tropics as well that are likely linked to enhanced upwelling. We elaborate on this in Section 2.5.

Lobe-shaped patterns of increased depletion in the middle to lower stratosphere extending from the tropics to the subtropics are similar in both the Chem-Dyn-Vol and NoHet40NS (see Figure 2-S3) runs, indicating that much of the low-latitude depletion is not produced in situ but rather is the result of horizontal transport of ozone-depleted air from higher latitudes in this model. Looking at the effects of volcanic aerosols on the tropics in the model as a function of pressure and time (Figure 2-S5) also shows both the dramatic increases in depletion after large-magnitude eruptions and

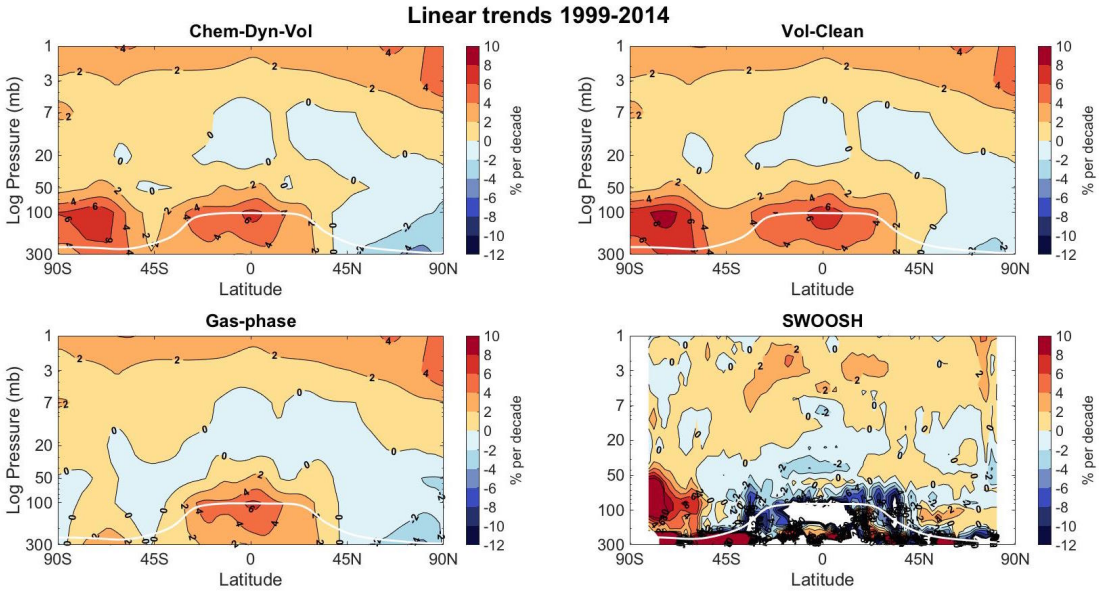

Figure 2-3: As in Figure 2-2 but for the recovery era (1999–2014).

the smaller effects after moderate-sized eruptions.

Comparison with SWOOSH shows broad areas of agreement in Figure 2-2, albeit with differences in detail, with deep depletion in the Antarctic and less depletion in the upper stratosphere. There is a large increase in modeled ozone near and just below the tropopause in the tropics that reaches more than 15% per decade; while part of this may reflect changing tropical dynamics or tropospheric chemistry, SWOOSH is not intended for tropospheric analysis, and some of the trends near the tropopause may be spurious.

In the recovery era shown in Figure 2-3, SWOOSH generally agrees with the model for all runs in the upper stratosphere, further supporting that the gas-phase chemistry is well represented in models. However, in the lower stratosphere the Chem-Dyn-Vol and Vol-Clean runs suggest positive trends over much of the globe apart from the Arctic that differ from those observed. Large negative trends in SWOOSH near the tropopause in the recovery era in the tropics (see Ball et al., 2018) are not reproduced in these model runs. The basic model pattern (particularly the positive trends in the lower stratosphere seen in all runs including gas-phase) partly

reflects dynamical changes in the MERRA fields used to drive specified dynamics WACCM, which are highly uncertain. Previous work found that differences between data sets in the lowermost stratosphere were larger than trends in ozone (Steinbrecht et al., 2017), and tropical trends in circulation have been shown to vary significantly depending on the reanalysis product used (Abalos et al., 2015; Wargan et al., 2018). Analysis of the simulations suggests that an accelerating Brewer-Dobson circulation in MERRA contributed to the tropical depletion seen directly above the tropopause in the gas-phase run in Figure 2-2, while the opposite occurred in the recovery era (Figure 2-3). Increases in ozone at and below the tropopause in this model also trace to tropospheric chemical production and subsequent transport into the lowermost stratosphere. Further analysis of tropospheric ozone trends is beyond the scope of this paper.

The difference between the Chem-Dyn-Vol and Vol-Clean runs is useful in showing where and by how much volcanoes have impeded recovery; this is especially noticeable in the Antarctic and Arctic lower stratosphere but is also significant in the midlatitudes (see also Figures 2-S4 and 2-S6). SWOOSH shows somewhat weaker recovery in the middle stratosphere (30 to 10 hPa) than the model; however, in all cases the trends here are very small, and natural dynamical variability is likely to be important (Stone et al., 2018).

Figures 2-S6 and 2-S7 show profile trends in more detail for different regions: 90° to 70° for the poles, 60° to 45° for the midlatitudes, 30° to 15° for the subtropics, and 15° to 0° for the tropics. Comparing the difference between starting dates for the depletion era in 1979 versus 1984 (Figure 2-S8) shows that the volcanic influence is sensitive to the timeframe chosen. As the latter start date begins during the influence of El Chichón, when ozone is already depleted from that eruption, the volcanic impacts over the time period appear smaller, whereas beginning in 1979 before the El Chichón eruption captures that volcano's effect. Removing tropical heterogeneous chemistry shows a slight difference of order 1% locally at the levels nearest the tropopause in the subtropics and tropics in this model.

2.5 Discussion and Conclusions

We have presented simulations using the WACCM model for both the ozone depletion (1979–1998) and recovery (1999–2014) eras to investigate the relative global impacts of heterogeneous chemistry, stratospheric volcanic aerosol loading, and gas-phase chemistry. We compared model-simulated TCO trends against both the SBUV and NIWA-BS data sets, and latitude-vertical ozone trends against the SWOOSH data set.

As is well known, heterogeneous chemistry dominates ozone depletion not only in the Antarctic but also in the global lower stratosphere and total column; here we quantified the contributions to ozone trends from heterogeneous chemistry using a state-of-the-art chemistry-climate model. Volcanoes are shown to have increased the depth of the depletion and have delayed the recovery (at least to 2014 as evaluated here) according to the best current chemical understanding, underscoring the necessity of including changes in aerosol content when analyzing recovery trends. Ozone trends in the tropics contributed to the global trends in the model in both the depletion and recovery eras, as shown in Table 2.1. Mixing between latitudes appears significant within this model, with our results indicating that ozone depleted air is transported from higher latitudes into the subtropics (i.e., cf. Figures 2-2 and 2-S3). Within the tropics themselves, in situ heterogeneous chemistry has small impacts on ozone as well, especially in the depletion era. All of the WACCM runs use the same underlying specified MERRA dynamics, making the contribution from changing chemistry easy to identify but also limiting the analysis that can be performed on changing dynamics.

Observational data broadly agree with our TCO analysis within their respective large uncertainties. Lack of satellite coverage for ozone observations before the 1980s, and limited coverage for much of that decade, makes constraining precise pre-depletion values difficult. The Chem-Dyn-Vol run shows a deeper depletion during the 1991–1997 era of elevated volcanic aerosol from Mt. Pinatubo and Cerro Hudson but tracks the data well for the rest of the depletion era, and for much of the recovery. SWOOSH latitude-pressure plot comparisons show general agreement with the model

runs, but with divergence near the tropopause and where percentage changes are small. Overall, comparison of the data and model after 1999 suggests that recovery trends are dominated by natural variability in the global lower stratosphere, with volcanic eruptions likely playing a role in this variability. Should the current period of moderate volcanic activity change to a quiescent one similar to that seen between Mt. Pinatubo and 2004, future ozone recovery can be expected to be easier to discern. The differences between our model runs demonstrate the effects due to changes in sulfate aerosols or heterogeneous chemistry schemes and underscore the importance of accurate representation of sulfate aerosols. Careful observations and analysis will be necessary to discern and attribute significant trends amid the noise of natural variability as the ozone layer evolves during the 21st century.

2.6 Supplemental Information

2.6.1 Regression Methods

Ozone data were preprocessed as monthly ozone anomalies. The ozone anomalies are then reconstructed using multiple linear regression. This requires regression functions that act as proxies for known short and long term ozone variations. The regression functions that we use are: constant, linear, QBO_{10}, QBO_{30} (winds at 10 and 30 hPa from Singapore radiosonde data,[1] Multivariate ENSO index,[2] solar cycle,[3] and aerosols[4] applied as

$$O'_3(t) = b_0 + \sum_{i=1}^{N} b_i x_i(t) + R(t)$$

Where $O'_3(t)$ represents the ozone anomaly, b_0 is the constant term, b_i are the coefficients corresponding to the regression functions $x_i(t)$, and $R(t)$ are the residuals. The QBO terms are expanded into two Fourier pairs to account for seasonal dependence of ozone on the QBO.

[1] http://www.geo.fu-berlin.de/en/met/ag/strat/produkte/qbo/index.html
[2] https://www.esrl.noaa.gov/psd/enso/mei/
[3] ftp://ftp.geolab.nrcan.gc.ca/data/solar_flux
[4] https://data.giss.nasa.gov/modelforce/strataer

2.6.2 Supplementary Figures

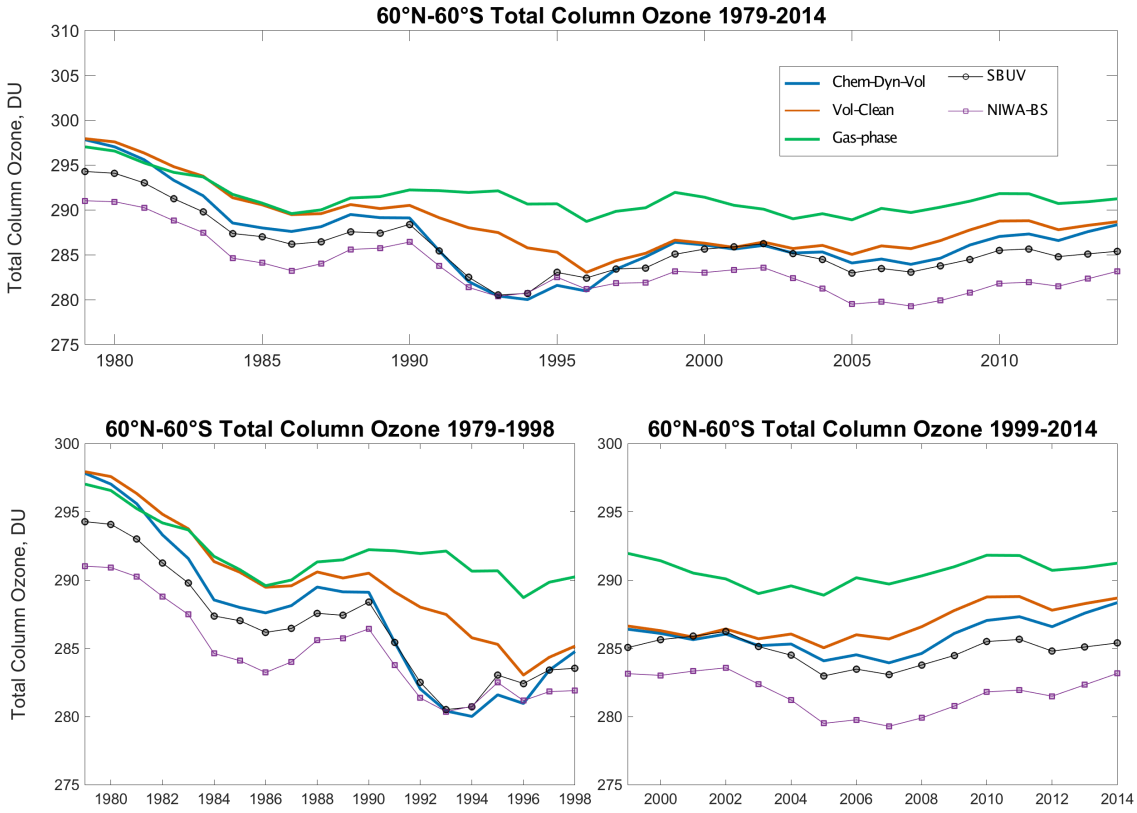

Figure 2-S1: **Top:** Time series of three year running mean of global mean (60°N–60°S) absolute values of total column ozone from 1979 to 2014 with gas-phase only, volcanically clean, and standard SD-WACCM runs including volcanoes shown as green, orange, and blue solid lines. SBUV and NIWA-BS total column ozone data are shown by the black line with circles and the purple line with squares, respectively. **Bottom left and right:** time series of global mean (60°N–60°S) total column ozone for the depletion era (left), here defined as 1979 to 1998 and for the recovery era (right), defined as 1999 to 2014.

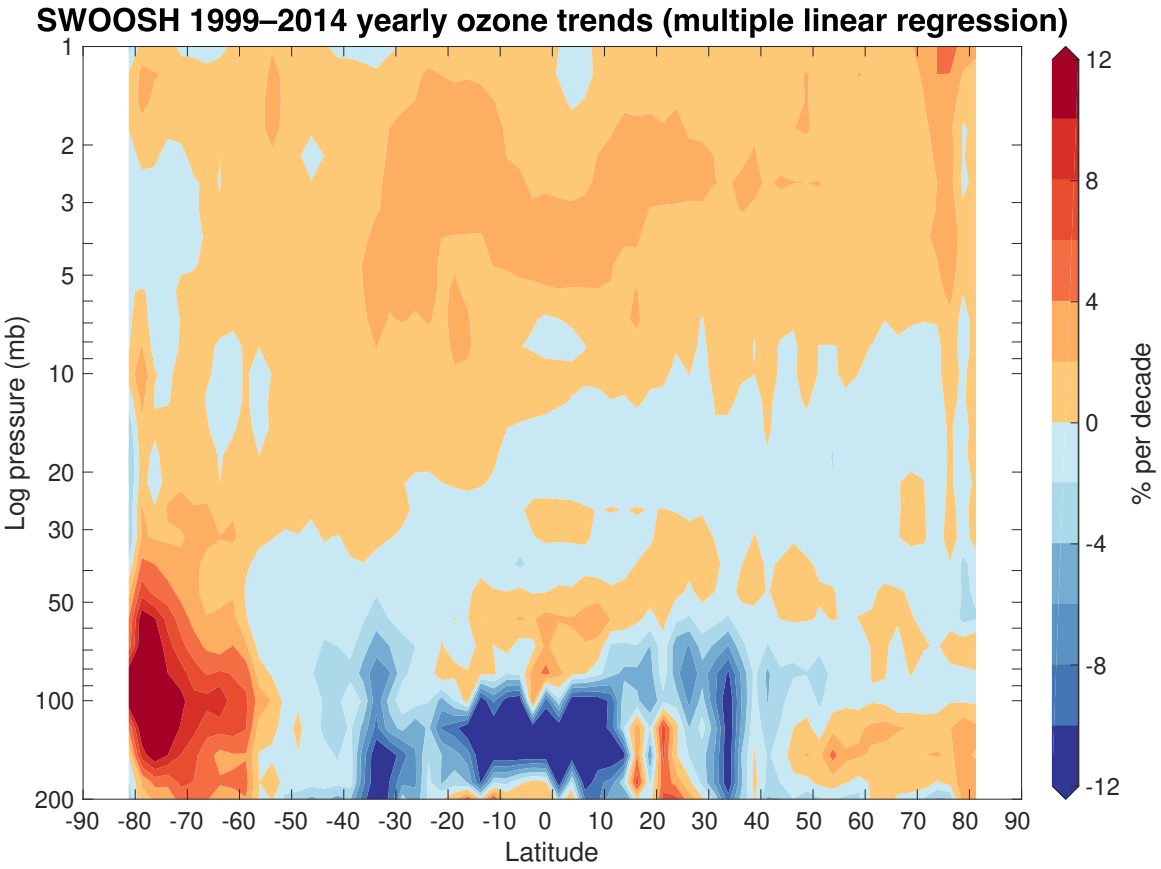

Figure 2-S2: SWOOSH recovery era trends with a full regression applied, for comparison to the simple linear trends in Figure 2-2 of the main text.

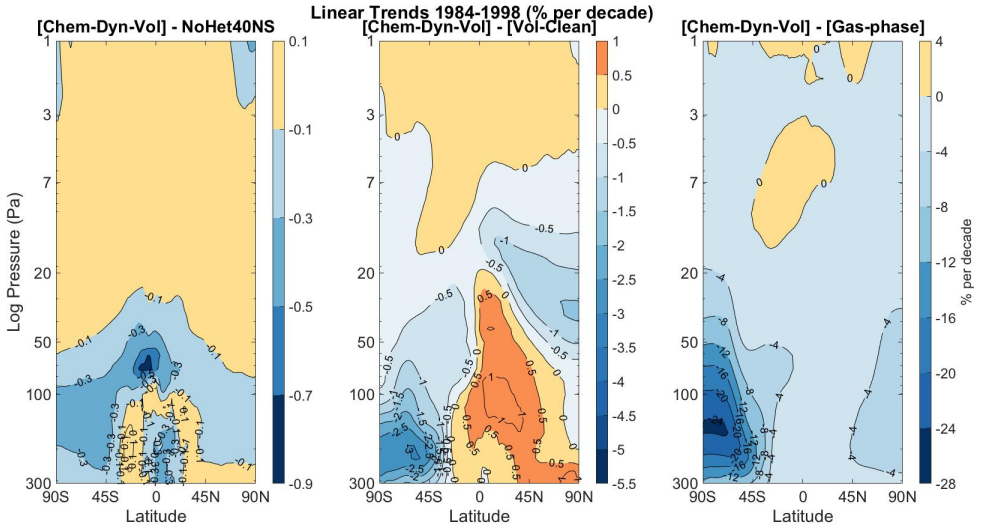

Figure 2-S3: Contour plots of differences in linear ozone trends during the SWOOSH depletion (1984–1998) era expressed as percent per decade relative to the Chem-Dyn-Vol run.

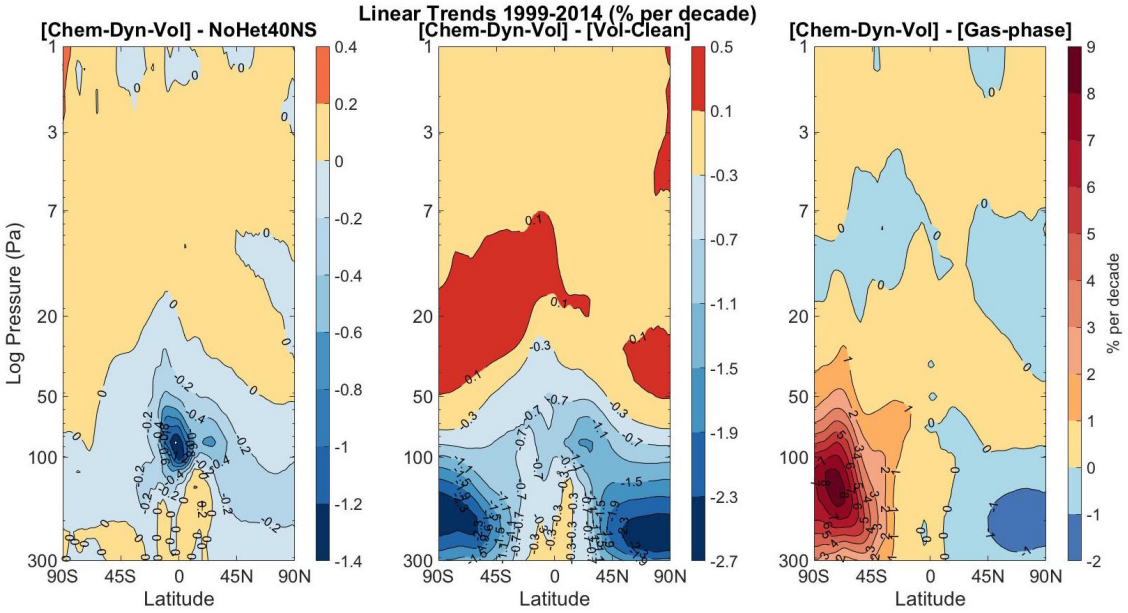

Figure 2-S4: As in 2-S3, but for the recovery (1999–2014) era.

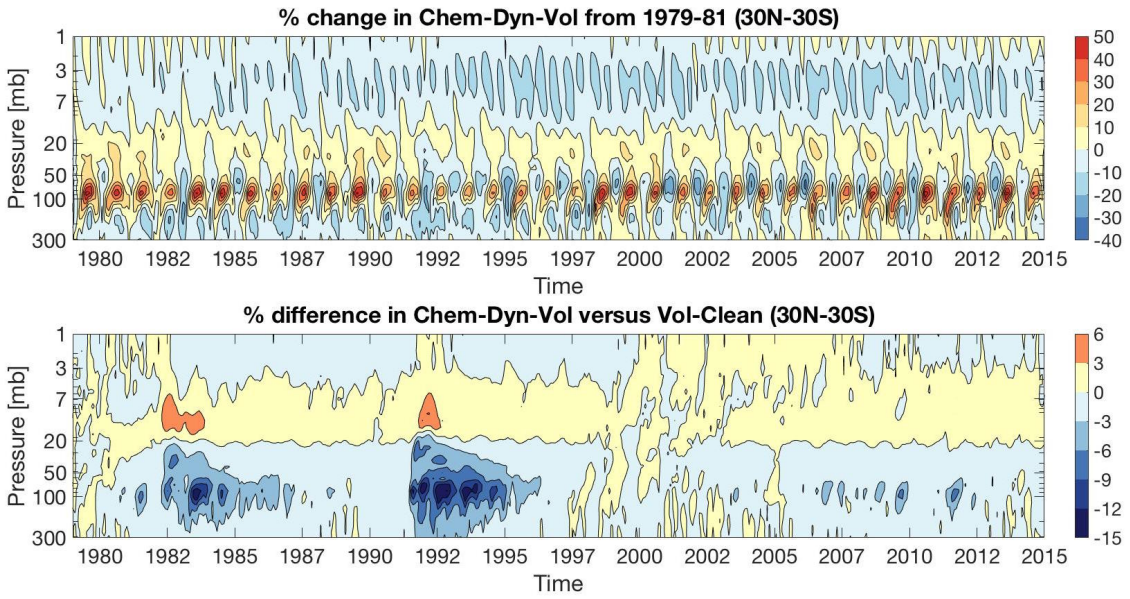

Figure 2-S5: Vertical changes in ozone as a function of time for 30°N–30°S expressed as a percentage change relative to the 1979–1981 average for Chem-Dyn-Vol (top), and percentage changes in Vol-Clean relative to Chem-Dyn-Vol (bottom). High frequency dynamical variability dominates trends in the lower stratosphere, but effects of large volcanoes can also be seen.

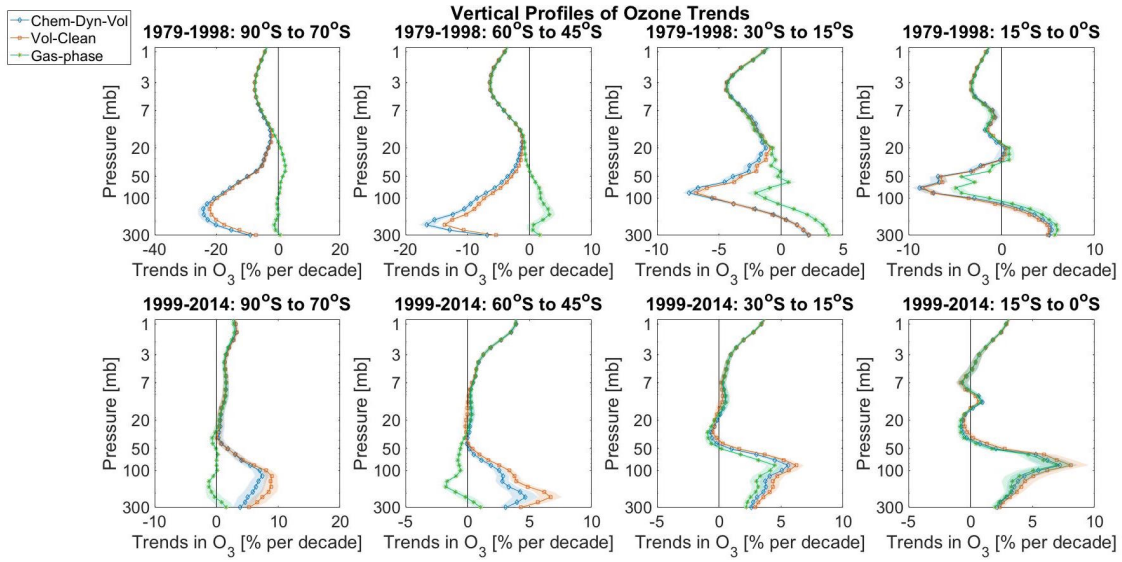

Figure 2-S6: Trends in ozone profiles expressed as percent per decade for Chem-Dyn-Vol (blue), Vol-Clean (red), and Gas-phase (green). Shading indicates 90% confidence intervals. The top row shows the depletion era (1979–1998) trends and the bottom row the recovery era (1999–2014) trends for, from left to right, the southern polar region, the southern mid-latitudes, the southern subtropics, and the southern deep tropics. Figure 2-S7 shows the northern hemisphere case.

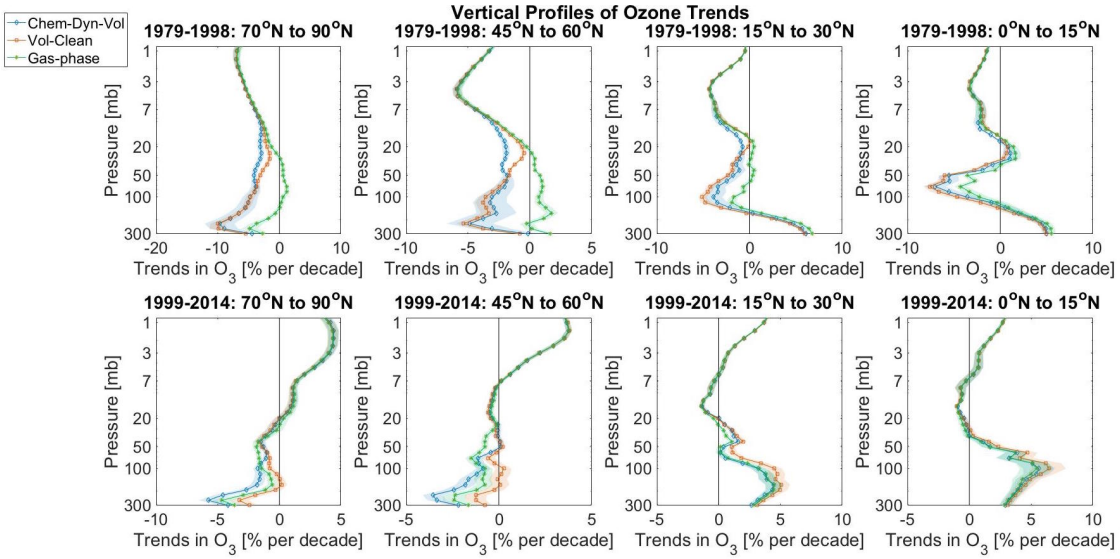

Figure 2-S7: As in Figure 2-S6, but for the northern hemisphere. Similar trends are seen as described in the body of the paper, although the Arctic trends are smaller.

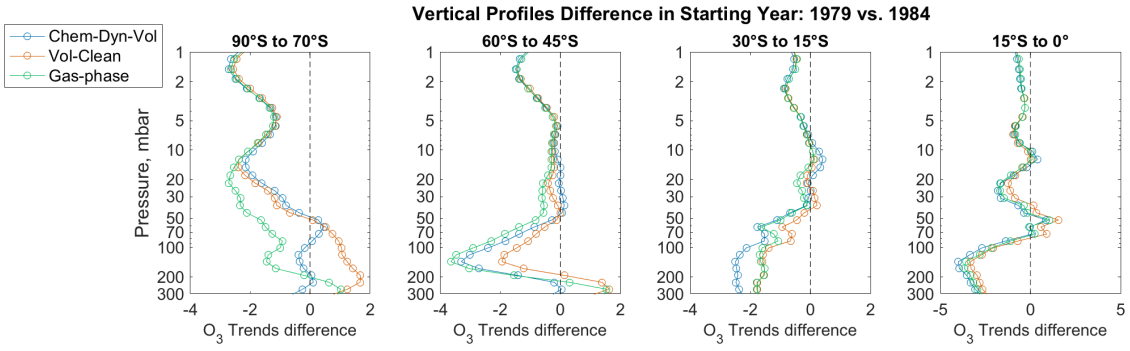

Figure 2-S8: Difference between vertical profile trends of ozone when using 1979–1998 as the depletion period and 1984–1998 as the depletion period in the model runs.

2.6.3 Supplementary Tables

Table 2-S1: Trends in Total Column Ozone in DU per Year for the Depletion and Recovery Eras and Percentage Differences from Chem-Dyn-Vol for 0 to 60°N

	1979-1998 (DU per year)	1979-1998 (Δ Chem-Dyn-Vol)	1999-2014 (DU per year)	1999-2014) (Δ Chem-Dyn-Vol)
Chem-Dyn-Vol	-0.645 (-0.908, -0.381)	–	0.070 (-0.060, 0.200)	–
Vol-Clean	-0.563 (-0.703, -0.422)	-12.7%	0.157 (0.059, 0.255)	+124.3%
NoHet40NS	-0.609 (-0.823, -0.395)	-5.6%	0.088 (-0.029, 0.204)	+25.7%
Gas-Phase	-0.228 (-0.360, -0.097)	-64.7%	0.045 (-0.070, 0.160)	-35.7%
SBUV	-0.598 (-0.786, -0.409)	-7.3%	-0.041 (-0.131, 0.048)	-158.6%
NIWA-BS	-0.530 (-0.703, -0.357)	-17.8%	0.070 (-0.100, 0.239)	0.0%

Table 2-S2: Trends in Total Column Ozone in DU per Year for the Depletion and Recovery Eras and Percentage Differences from Chem-Dyn-Vol for 0 to 60°S

	1979-1998 (DU per year)	1979-1998 (Δ Chem-Dyn-Vol)	1999-2014 (DU per year)	1999-2014) (Δ Chem-Dyn-Vol)
Chem-Dyn-Vol	-1.013 (-1.171, -0.855)	–	0.190 (0.010, 0.370)	–
Vol-Clean	-0.838 (-0.955, -0.720)	-17.3%	0.237 (0.089, 0.386)	+24.7%
NoHet40NS	-0.970 (-1.107, -0.834)	-4.2%	0.202 (0.026, 0.378)	+6.3%
Gas-Phase	-0.356 (-0.520, -0.192)	-64.9%	0.046 (-0.113, 0.205)	-75.8%
SBUV	-0.720 (-0.878, -0.562)	-28.9%	0.007 (-0.168, 0.181)	-96.3%
NIWA-BS	-0.473 (-0.622, -0.324)	-53.3%	-0.214 (-0.408, -0.021)	-212.6%

References

[1] Abalos, M., Legras, B., Ploeger, F., & Randel, W. J. (2015). Evaluating the advective Brewer-Dobson circulation in three reanalyses for the period 1979–2012. *JJournal of Geophysical Research: Atmospheres, 120*(15), 7534–7554. https://doi.org/10.1002/2015JD023182

[2] Ball, W. T., Alsing, J., Mortlock, D. J., Staehelin, J., Haigh, J. D., Peter, T., ... & Rozanov, E. V. (2018). Evidence for a continuous decline in lower stratospheric ozone offsetting ozone layer recovery. *Atmospheric Chemistry and Physics, 18*(2), 1379–1394.https://doi.org/10.5194/acp-18-1379-2018

[3] Bodeker, G. E., Shiona, H., & Eskes, H. (2005). Indicators of Antarctic ozone depletion. *Atmospheric Chemistry and Physics, 5*(10), 2603–2615. https://doi.org/10.5194/acp-5-2603-2005

[4] Chehade, W., Weber, M., & Burrows, J. P. (2014). Total ozone trends and variability during 1979–2012 from merged data sets of various satellites. *Atmospheric Chemistry and Physics, 14*(13), 7059–7074. https://doi.org/10.5194/acp-14-7059-2014

[5] Davis, S. M., Rosenlof, K. H., Hassler, B., Hurst, D. F., Read, W. G., Vömel, H., ... & Damadeo, R. (2016). The Stratospheric Water and Ozone Satellite Homogenized (SWOOSH) database: a long-term database for climate studies. *Earth System Science Data, 8*(2), 461–490. https://doi.org/10.5194/essd-8-461-2016

[6] Douglass, A. R., Strahan, S. E., Oman, L. D., & Stolarski, R. S. (2014). Understanding differences in chemistry climate model projections of stratospheric ozone. *Journal of Geophysical Research: Atmospheres, 119*(8), 4922–4939. https://doi.org/10.1002/2013JD021159

[7] Farman, J. C., Gardiner, B. G., & Shanklin, J. D. (1985). Large losses of total ozone in Antarctica reveal seasonal ClO_x/NO_x interaction. *Nature, 315*(6016), 207–210. https://doi.org/10.1038/315207a0

[8] Garcia, R. R., Smith, A. K., Kinnison, D. E., Cámara, Á. D. L., & Murphy, D. J. (2017). Modification of the gravity wave parameterization in

the Whole Atmosphere Community Climate Model: Motivation and results. *Journal of the Atmospheric Sciences, 74*(1), 275–291. https://doi.org/10.1175/JAS-D-16-0104.1

[9] Hofmann, D. J., & Solomon, S. (1989). Ozone destruction through heterogeneous chemistry following the eruption of El Chichón. *Journal of Geophysical Research, 94*(D4), 5029–5041. https://doi.org/10.1029/JD094iD04p05029

[10] Keeble, J., Brown, H., Abraham, N. L., Harris, N. R., & Pyle, J. A. (2018). On ozone trend detection: Using coupled chemistry-climate simulations to investigate early signs of total column ozone recovery. *Atmospheric Chemistry and Physics, 18*(10), 7625–7637. https://doi.org/10.5194/acp-18-7625-2018

[11] Klobas, E. J., Wilmouth, D. M., Weisenstein, D. K., Anderson, J. G., & Salawitch, R. J. (2017). Ozone depletion following future volcanic eruptions. *Geophysical Research Letters, 44*(14), 7490–7499. https://doi.org/10.1002/2017GL073972

[12] Kyrölä, E., Laine, M., Sofieva, V., Tamminen, J., Päivärinta, S. M., Tukiainen, S., ... & Thomason, L. (2013). Combined SAGE II–GOMOS ozone profile data set for 1984–2011 and trend analysis of the vertical distribution of ozone. *Atmospheric Chemistry and Physics, 13*(21), 10645–10658. https://doi.org/10.5194/acp-13-10645-2013

[13] Mahieu, E., Chipperfield, M. P., Notholt, J., Reddmann, T., Anderson, J., Bernath, P. F., ... & Walker, K. A. (2014). Recent Northern Hemisphere stratospheric HCl increase due to atmospheric circulation changes. *Nature, 515*(7525), 104–107.. https://doi.org/10.1038/nature13857

[14] Marsh, D. R., Mills, M. J., Kinnison, D. E., Lamarque, J. F., Calvo, N., & Polvani, L. M. (2013). Climate change from 1850 to 2005 simulated in CESM1 (WACCM). *Journal of Climate, 26*(19), 7372–7391. https://doi.org/10.1175/JCLI-D-12-00558.1

[15] McPeters, R. D., Bhartia, P. K., Haffner, D., Labow, G. J., & Flynn, L. (2013). The version 8.6 SBUV ozone data record: An overview. *Journal of Geophysical Research: Atmospheres, 118*(14), 8032–8039. https://doi.org/10.1002/jgrd.50597

[16] Mills, M. J., Schmidt, A., Easter, R., Solomon, S., Kinnison, D. E., Ghan, S. J., ... & Gettelman, A. (2016). Global volcanic aerosol properties derived from emissions, 1990–2014, using CESM1 (WACCM). *Journal of Geophysical Research: Atmospheres, 121*(5), 2332–2348. https://doi.org/10.1002/2015JD024290

[17] Molina, M. J., & Rowland, F. S. (1974). Stratospheric sink for chlorofluoromethanes: Chlorine atom-catalysed destruction of ozone. *Nature, 249*(5460), 810–812. https://doi.org/10.1038/249810a0

[18] Naik, V., Horowitz, L. W., Daniel Schwarzkopf, M., & Lin, M. (2017). Impact of volcanic aerosols on stratospheric ozone recovery. *Journal of Geophysical Research: Atmospheres, 122*(17), 9515–9528. https://doi.org/10.1002/2016JD025808

[19] Neely III, R. R., & Schmidt, A. (2016). VolcanEESM: Global volcanic sulphur dioxide (SO_2) emissions database from 1850 to present—Version 1.0. Centre for Environmental Data Analysis, 4 February 2016.

[20] Randel, W. J., Stolarski, R. S., Cunnold, D. M., Logan, J. A., Newchurch, M. J., & Zawodny, J. M. (1999). Trends in the vertical distribution of ozone. *Science, 285*(5434), 1689–1692. https://doi.org/10.1126/science.285.5434.1689

[21] Randel, W. J., & Thompson, A. M. (2011). Interannual variability and trends in tropical ozone derived from SAGE II satellite data and SHADOZ ozonesondes. *Journal of Geophysical Research: Atmospheres, 116*(D7). https://doi.org/10.1029/2010JD015195

[22] Rinsland, C. P., Mahieu, E., Zander, R., Jones, N. B., Chipperfield, M. P., Goldman, A., ... & Blumenstock, T. (2003). Long-term trends of inorganic chlorine from ground-based infrared solar spectra: Past increases and evidence for stabilization. *Journal of Geophysical Research: Atmospheres, 108*(D8).https://doi.org/10.1029/2002JD003001

[23] Rodriguez, J. M., Ko, M. K., & Sze, N. D. (1991). Role of heterogeneous conversion of N_2O_5 on sulphate aerosols in global ozone losses. *Nature, 352*(6331), 134–137. https://doi.org/10.1038/352134a0

[24] Sofieva, V. F., Kyrölä, E., Laine, M., Tamminen, J., Degenstein, D., Bourassa, A., ... & Bhartia, P. K. (2017). Merged SAGE II, Ozone_cci and OMPS ozone profile dataset and evaluation of ozone trends in the stratosphere. *Atmospheric Chemistry and Physics, 17*(20), 12533–12552. https://doi.org/10.5194/acp-17-12533-2017

[25] Solomon, S. (1999). Stratospheric ozone depletion: A review of concepts and history. *Reviews of Geophysics, 37*(3), 275–316. https://doi.org/10.1029/1999RG900008

[26] Solomon, S., Daniel, J. S., Neely, R. R., Vernier, J. P., Dutton, E. G., & Thomason, L. W. (2011). The persistently variable "background" stratospheric aerosol layer and global climate change. *Science, 333*(6044), 866–870. https://doi.org/10.1126/science.1206027

[27] Solomon, S., Garcia, R. R., Rowland, F. S., & Wuebbles, D. J. (1986). On the depletion of Antarctic ozone. *Nature, 321*(6072), 755–758. https://doi.org/10.1038/321755a0

[28] Solomon, S., Ivy, D. J., Kinnison, D., Mills, M. J., Neely, R. R., & Schmidt, A. (2016a). Emergence of healing in the Antarctic ozone layer. *Science, 353*(6296), 269–274. https://doi.org/10.1126/science.aae0061

[29] Solomon, S., Kinnison, D., Garcia, R. R., Bandoro, J., Mills, M., Wilka, C., ... & Höpfner, M. (2016). Monsoon circulations and tropical heterogeneous chlorine chemistry in the stratosphere. *Geophysical Research Letters, 43*(24), 12-624. https://doi.org/10.1002/2016GL071778

[30] Solomon, S., Kinnison, D. E., Bandoro, J., & Garcia, R. R. (2015). Simulation of polar ozone depletion: An update. *Journal of Geophysical Research: Atmospheres, 120*(15), 7958–7974. https://doi.org/10.1002/2015JD023365

[31] Steinbrecht, W., Froidevaux, L., Fuller, R., Wang, R., Anderson, J., Roth, C., ... & Tummon, F. (2017). An update on ozone profile trends for the period 2000 to 2016. *Atmospheric Chemistry and Physics, 17*(17), 10675–10690. https://doi.org/10.5194/acp-17-10675-2017

[32] Stone, K. A., Solomon, S., & Kinnison, D. E. (2018). On the identification of ozone recovery. *Geophysical Research Letters, 45*(10), 5158–5165. https://doi.org/10.1029/2018GL077955

[33] Vernier, J. P., Thomason, L. W., Pommereau, J. P., Bourassa, A., Pelon, J., Garnier, A., ... & Vargas, F. (2011). Major influence of tropical volcanic eruptions on the stratospheric aerosol layer during the last decade. *Geophysical Research Letters, 38*(12). https://doi.org/10.1029/2011GL047563

[34] Wargan, K., Orbe, C., Pawson, S., Ziemke, J. R., Oman, L. D., Olsen, M. A., ... & Emma Knowland, K. (2018). Recent decline in extratropical lower stratospheric ozone attributed to circulation changes. *Geophysical Research Letters, 45*(10), 5166-5176. https://doi.org/10.1029/2018GL077406

[35] Weber, M., Coldewey-Egbers, M., Fioletov, V. E., Frith, S. M., Wild, J. D., Burrows, J. P., ... & Loyola, D. (2018). Total ozone trends from 1979 to 2016 derived from five merged observational datasets–the emergence into ozone recovery. *Atmospheric Chemistry and Physics, 18*(3), 2097-2117. https://doi.org/10.5194/acp-18-2097-2018

[36] Wegner, T., Kinnison, D. E., Garcia, R. R., & Solomon, S. (2013). Simulation of polar stratospheric clouds in the specified dynamics version of the Whole Atmosphere Community Climate Model. *Journal of Geophysical Research: Atmospheres, 118*(10), 4991–5002. https://doi.org/10.1002/jgrd.50415

Chapter 3

Atmospheric Chemistry Signatures of an Equatorially Symmetric Matsuno–Gill Circulation Pattern

Abstract

Matsuno–Gill circulations have been widely studied in tropical meteorology, but their impact on stratospheric chemistry has seldom been explicitly evaluated. This study demonstrates that, in a model nudged to reanalysis, anticyclonic Rossby wave gyres that form near the tropopause as a result of equatorially symmetric heating in the troposphere provide a dynamical mechanism to influence tropical and subtropical atmospheric chemistry during near-equinox months. The anticyclonic flow entrains extratropical air from higher latitudes into the deep tropics of both hemispheres and induces cooling in the already cold upper-troposphere/lower-stratosphere (UTLS) region. Both of these aspects of the circulation allow heterogeneous chlorine activation on sulfuric acid aerosols to proceed rapidly, primarily via the $HCl + ClONO_2$ reaction. Precipitation rates and heating rates from reanalysis are shown to be consistent with these heating and circulation response patterns in the months of interest. This study

This chapter was published in *Journal of the Atmospheric Sciences* (Wilka et al., 2021). The publication and its supplement are available at `https://doi.org/10.1175/JAS-D-20-0025.1`

analyzes specified dynamics simulations from the Whole Atmosphere Community Climate Model (SD-WACCM) with and without tropical heterogeneous chemistry to demonstrate that these circulations influence substantially the distributions of, for example, NO_2 and ClO in the UTLS tropics and subtropics of both hemispheres. This provides a previously unrecognized dynamical influence on the spatial structures of atmospheric composition changes in the UTLS during near-equinox months.

3.1 Introduction

Matsuno (1966) studied the equatorial waves produced in response to equatorial heating in the context of a linearized, beta-plane model, successfully identifying the equatorially trapped Kelvin wave and the off-equator Rossby wave gyre responses. Gill (1980) imposed both symmetric and asymmetric heating across the equator and calculated the response of the tropical atmosphere to these idealized perturbations using linear theory. Both papers show variants of a “bull’s eye" pattern in pressure perturbations (Figure 9 in Matsuno 1966; Figure 1b in Gill 1980), which are now seen as indicative of the Matsuno–Gill response. While the real atmosphere is more complicated than these simplified models, and the assumptions of steady heating and time-invariance are never perfectly valid, the basic patterns have been identified in multiple dynamical studies (Jin and Hoskins 1995; Adames and Wallace 2017; Rodwell and Hoskins 2001; among others). The wind response takes the form of two Rossby cyclones in the lower troposphere and is overlain by anticyclones in the upper troposphere/lower stratosphere (UTLS), which are located to the northwest and southwest of the heating maximum, as well as an equatorially trapped Kelvin wave to the east over the Pacific, with easterly flow in the lower troposphere and westerly flow aloft. These zonal asymmetries in the Matsuno–Gill pattern decay upward into the stratosphere, with ascent and anomalously cold air in the lower stratosphere overlying regions of deep convection and greatest tropopause heights. The dynamics of this pattern have been widely studied in the decades since its description; here we examine some of its impacts on UTLS chemistry, which result from the combination

of winds and temperature anomalies.

The importance of heterogenous chlorine activation reactions to ozone depleting chemistry has been well established for decades (Solomon et al. 1986; Solomon 1999, and references therein) and is known to be the key driver of the so-called ozone hole. Heterogeneous reactions on stratospheric aerosols convert chlorine from the reservoir species HCl and $ClONO_2$ to active forms that can destroy ozone in catalytic cycles. Of particular importance are the HCl + $ClONO_2$ $\rightarrow$ Cl_2 + HNO_3, H_2O + $ClONO_2$ $\rightarrow$ HOCl + HNO_3, and HCl + HOCl $\rightarrow$ H_2O + Cl_2 reactions. Multiple factors influence the rates of these reactions, including temperature, water vapor levels, chlorine precursor levels, and aerosol surface area. The HCl + $ClONO_2$ reaction, which is in many regions the dominant source of activation, has an extremely strong inverse temperature dependence, with reaction efficiencies that decrease by six orders of magnitude between 190 K and 205 K. This dependence is due to multiple factors, but below 200 K is dominated by the increasing solubility of HCl with decreasing temperature (Shi et al. 2001). The importance of these reactions has been extensively studied in the Arctic and Antarctic for decades, and in recent years there has been an increased focus on the potential for this chemistry to proceed outside the polar regions, specifically on liquid sulfuric acid aerosols that are ubiquitous in the lower stratosphere (Anderson et al. 2017; Robrecht et al. 2019).

Solomon et al. (2016) showed that the strong anticyclone of the East Asian summer monsoon (EASM) is capable of entraining chlorine (in the form of HCl) from higher latitudes. This chlorine enters the UTLS region above the EASM anticyclone, where temperatures are anomalously cold due to the response to convective heating (Highwood and Hoskins 1998). This combination of increased chlorine mixing ratios and cold temperatures drives chlorine activation. This work motivates us to consider additional conditions for moving chlorine into cold regions in the tropics that are difficult to describe in a zonally averaged framework, such as has often been used in the past to study meridional gradients in stratospheric chemical species. An overall goal is to contribute to a growing body of research that considers the effect of eddies and other longitudinally asymmetric features on stratospheric composition and chem-

istry. Identifying such features would provide an improved understanding of coupling between chemistry and transport, and a potential target for future observational campaigns in the tropical UTLS.

Matsuno–Gill tropical circulation patterns have seldom been studied in connection with stratospheric chemistry until recently. Solomon et al. (2016) was one of the first studies to investigate the response of stratospheric chlorine to equatorially asymmetric heating of this type, and this work extends that by looking at the equatorially symmetric case, which is more typically found in near-equinox months. Relative to the EASM anticyclone, the equatorially symmetric Matsuno–Gill anticyclones are somewhat weaker and situated deeper in the tropics, so they advect less chlorine from higher latitudes. However, since the tropopause temperatures in the deep tropics are lower on average than those at the latitude of the EASM anticyclone, the negative temperature perturbations from this type of Matsuno–Gill circulation nonetheless drive very swift chlorine activation. As explored below, this circulation pattern provides a pathway for chlorine activation in the deep tropics in months where activation has not previously been considered.

3.2 Methods

3.2.1 Rainfall data

We use NOAA's Global Precipitation Climatology Project (GPCP), version 2.3, to investigate precipitation patterns, which are a good observable proxy for heating due to latent heat release. The GPCP combines observations from rain gauge stations and soundings with satellite precipitation data to produce a $2.5^\circ \times 2.5^\circ$ resolution global product that covers land and ocean at monthly resolution from 1979 to present day (Adler et al. 2003).

3.2.2 Model

We use NCAR's Community Earth System Model with a "specified dynamics" (SD) version of the Whole Atmosphere Community Climate Model, version 4, as the atmospheric component. This model configuration is formally denoted CESM(SD-WACCM4), but throughout this paper we refer to it simply as SD-WACCM. Below 50 km, SD-WACCM is nudged to externally specified temperature, zonal and meridional wind, and surface pressure fields from the Modern-Era Retrospective Analysis for Research and Applications (MERRA), with a relaxation time of 50h. MERRA is a global atmospheric reanalysis beginning in 1979 and continuing through 2016 that is produced and maintained by NASA (Rienecker et al. 2011). To investigate heating rates, we present monthly means derived from the daily mean output files for each pressure level of interest for the diabatic heating.

WACCM is a high-top model with detailed gas-phase and heterogeneous chemistry schemes that include the O_x, NO_x, HO_x, ClO_x, and BrO_x reaction families. The chemistry is fully interactive, with a time step of 30 min, and the model has been extensively evaluated for use in stratospheric studies (Marsh et al. 2013; Mills et al. 2017; Froidevaux et al. 2019). About 5 pptv of very short-lived substances (VSLS) are included in the total bromine loading, but chlorine from VSLS is not included. Heterogeneous reactions on cirrus ice particles are not included. SD-WACCM has 1.9°× 2.5° (latitude–longitude) horizontal resolution, with 88 pressure levels from the surface up to 140 km. Stratospheric sulfate aerosols are modeled as three lognormal modes and include the effect of nucleation, condensation, coagulation, and sedimentation in a microphysics scheme described in detail in Mills et al. (2016). The background sulfur loading from volcanic eruptions is taken from a database developed by Neely and Schmidt (2016) that specifies plume injection height and the amount of sulfur injected.

We consider two different runs of SD-WACCM over four years from 2009 to 2012. In the first run, labeled Chem-Dyn-Vol, the effects of chemistry, dynamics, and volcanic eruptions are all included. This run is the standard and, in SD-WACCM,

represents the best attempt to simulate the real world for those years. Note, however, that the chemical scheme in Chem-Dyn-Vol does not include water ice chemistry; the implications of this are discussed below, in Section 3.4. The second run, labeled NoHet40NS, turns off all heterogeneous reactions involving chlorine and bromine between 40°N and 40°S but permits heterogeneous reactions not involving these species. Temperatures at midlatitudes are too warm to drive the heterogeneous chemistry of interest here. Comparing these two runs allows us to isolate the signature of in situ tropical heterogeneous chlorine and bromine chemistry as distinct from polar regions. We examine monthly-mean output for this study and discuss the potential influence of more transient behavior in Section 3.4.

We focus on near-equinox months for this analysis, so the influence from summer monsoonal patterns in either hemisphere should be limited. As an example, we present results below for November 2009 (a month without a major stratospheric-impacting volcanic eruption) but note that equatorially symmetric Matsuno–Gill patterns are identified in other months as well. The impacts of these Matsuno–Gill patterns are manifested in chemical responses in low latitudes of both hemispheres, whereas responses to heating displaced from the equator, such as the EASM, are confined to the warm season hemisphere of active monsoon rainfall. We find similar results in several other near-equinox months in the 4-year time series we looked at, including April 2009 and 2011, November 2011, and March 2012. We expect that in a longer time series there would be many more examples.

3.3 Results

Figure 3-1a shows the mean precipitation rate for November 2009 from 40°N to 40°S from the GPCP. The highest rates occur over the equatorial Indian Ocean and over the western Pacific Ocean between 15°N and 15°S. These areas are therefore regions of strong latent heat release and are a better marker of tropical diabatic heating locations than sea surface temperature would be. We examine the diabatic heating rates at multiple levels in MERRA, which provides the meteorological fields for SD-WACCM

as described above, and find that the heating tendency (K day^{-1}) due to physics is at a maximum near 400 hPa, as shown in Figure 3-1b for November 2009. Although the real-world response is more varied, this resembles the vertical profile of the heating prescribed in the Gill model. The maximum in the deep tropics and the north-and-southward extending lobes track the observed precipitation patterns closely, as we would expect given the close linkage between diabatic heating rates and latent heat release. While the heating itself extends further into the Southern Hemisphere than the Northern Hemisphere, anomalies are clearly visible in both hemispheres. These heating rates decay higher in the troposphere, and at and above the tropopause there is little remnant in the diabatic heating signal. By 100 hPa (Figure 3-S1), the signal has vanished.

Figure 3-2a shows the vector winds and temperatures in SD-WACCM on the 85-hPa level for November 2009. The wind response to the heating pattern consists of cyclonic behavior in the lower troposphere and mirrored anticyclonic behavior in the lower stratosphere. Anticyclones can be seen in Figure 3-2a on the poleward flanks of the heating pattern, specifically east of Taiwan and off the northeast coast of Australia. The eastward-propagating Kelvin wave characteristic of the Matsuno–Gill is manifested by the pattern of eastward winds visible in the equatorial Pacific east of the date line, toward the eastern part of the 192 K temperature contour. The anticyclones provide a mechanism, analogous to the anticyclone of the EASM, to entrain chlorine in reservoir form from higher latitudes. We see this when we examine SD-WACCM's November 2009 HCl distribution at 85 hPa in Figure 3-2b. Higher volume mixing ratios track the anticyclone near 160°E in the Northern Hemisphere and 140°E in the Southern Hemisphere, enhancing HCl by 50–100 pptv above what is seen in the rest of the Pacific Ocean at those latitudes. The other main form of reservoir chlorine, $ClONO_2$, is also enhanced by this effect, as can be seen in Figure 3-S2.

At temperatures below 194 K, the $ClONO_2$ + HCl reaction proceeds extremely efficiently, whereas above 195 K the reaction rate drops so steeply that chlorine enhancement potential is minimal. We see this expected general relationship in Figure

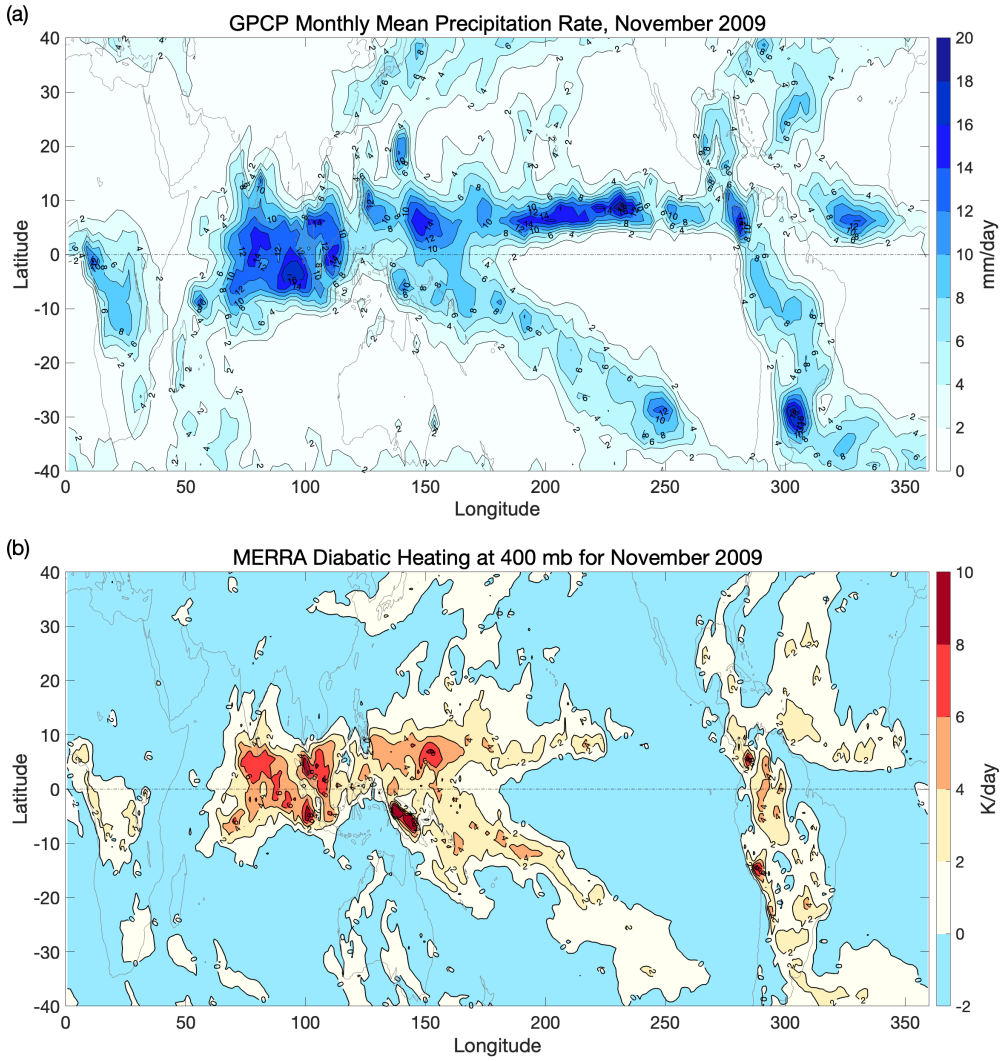

Figure 3-1: **(a)** Precipitation (mm day^{-1}) from the GPCP and **(b)** diabatic heating rates (K day^{-1}) at 400 hPa from MERRA reanalysis from 40°N to 40°S, averaged for November 2009.

3-3, where we compare the tropics in November 2009 (Figure 3-3a) to the southern high latitudes in October 2009 (Figure 3-3b), when the ozone depletion in Antarctica peaks for the year. Although there is greater scatter in the tropics because some cold regions are isolated from any entrained chlorine, and the enhancement levels in Antarctica reach an order of magnitude higher, we can see that in both cases it is only possible to get enhanced ClO at colder temperatures. Temperature histories can also induce scatter: for example, air at 195 K on one day may contain chlorine activated

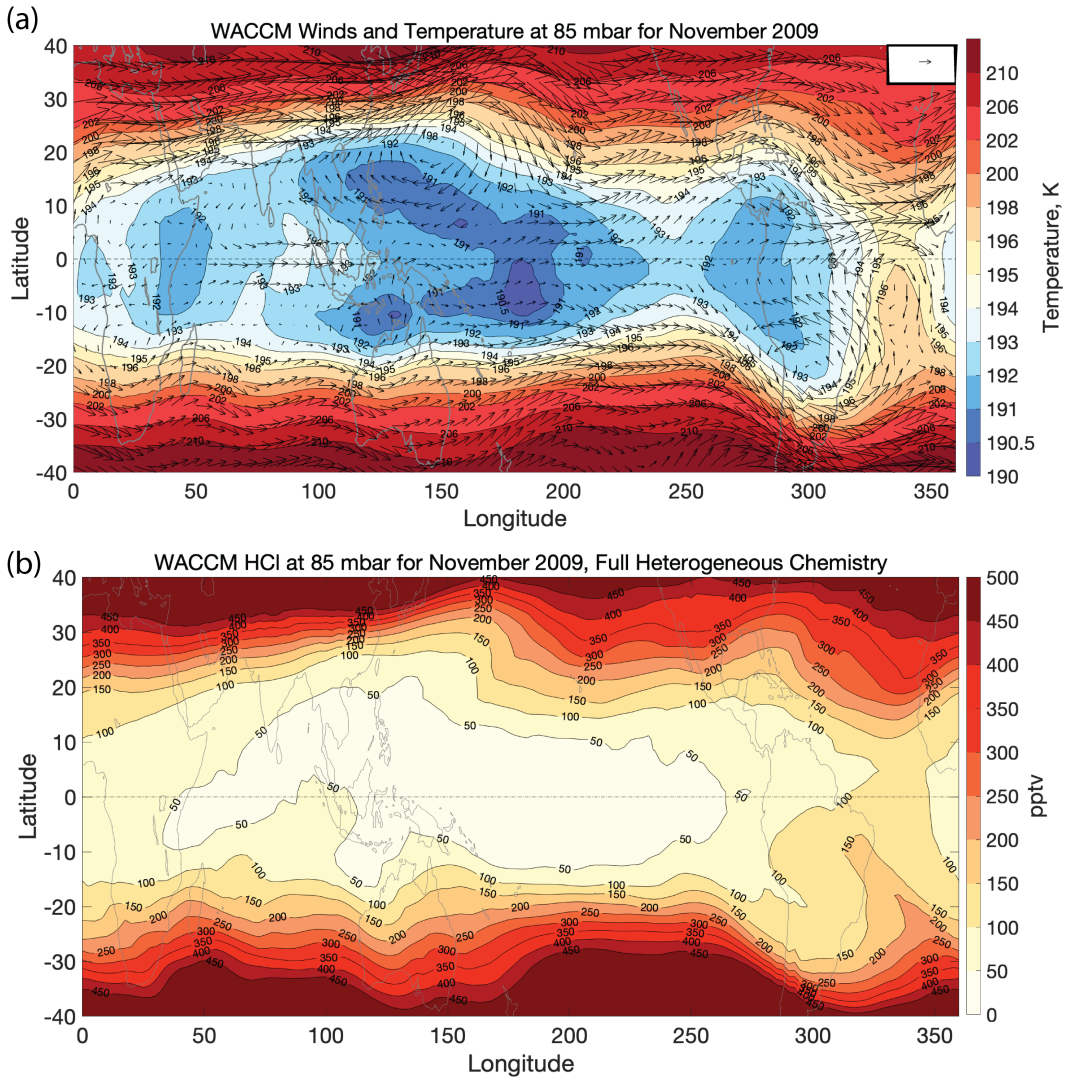

Figure 3-2: **(a)** Monthly mean WACCM horizontal flow and temperature (K) at 85 hPa from 40°N to 40°S for November 2009. The winds are shown as vectors, with the length of the tail corresponding to the strength of the wind. A 5 m/s vector is displayed in the upper right for scale. **(b)** Monthly mean WACCM HCl volume mixing ratios at 85 hPa in the tropics for November 2009. Heterogeneous chemistry is turned on at all latitudes.

a day or two earlier when the air was 192 K. A Lagrangian back-trajectory analysis could be used to further evaluate this question, but Figure 3-3 is sufficient to show that the highest levels of ClO are associated with temperatures below 192 K for both the Antarctic and the tropics.

The coldest temperatures (< 192 K) in Figure 3-2a occur over a broad region of

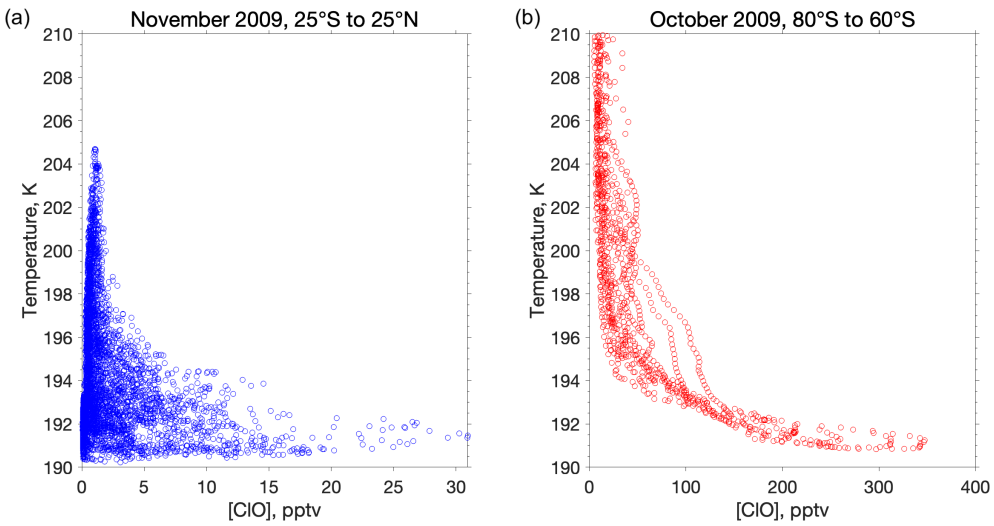

Figure 3-3: Distribution of ClO mixing ratios and associated temperatures in **(a)** the tropics for November 2009 and **(b)** the Antarctic for October 2009. Both plots are at 85 hPa for all longitudes.

the western Pacific and are qualitatively consistent with the concept of a stratospheric fountain first described by Newell and Gould-Stewart (1981). Highwood and Hoskins (1998) linked these stratospheric thermal anomalies to the pressure anomalies found in the upper troposphere that form part of the classic response to equatorially symmetric Matsuno–Gill heating perturbations. This circulation pattern therefore enhances chlorine activation in two ways: by entraining reservoir chlorine in the form of HCl and $ClONO_2$ from higher latitudes (Figure 3-2b and Figure 3-S2) and by lowering temperatures such that activation proceeds more rapidly (Figure 3-2a). In addition to the broad region where temperatures are below 192 K, there is a smaller but still substantial region in both hemispheres where they drop below 191 K. This region is roughly symmetric about the equator, but with a greater extent in the Northern Hemisphere. There are other, smaller regions of extremely cold temperatures to the west and east of the main response pattern which may be associated with convection over land, such as over the Amazon basin.

SD-WACCM's chemistry fields demonstrate the impacts of these cold temperatures and circulation patterns. We focus on two different chemical features at 85

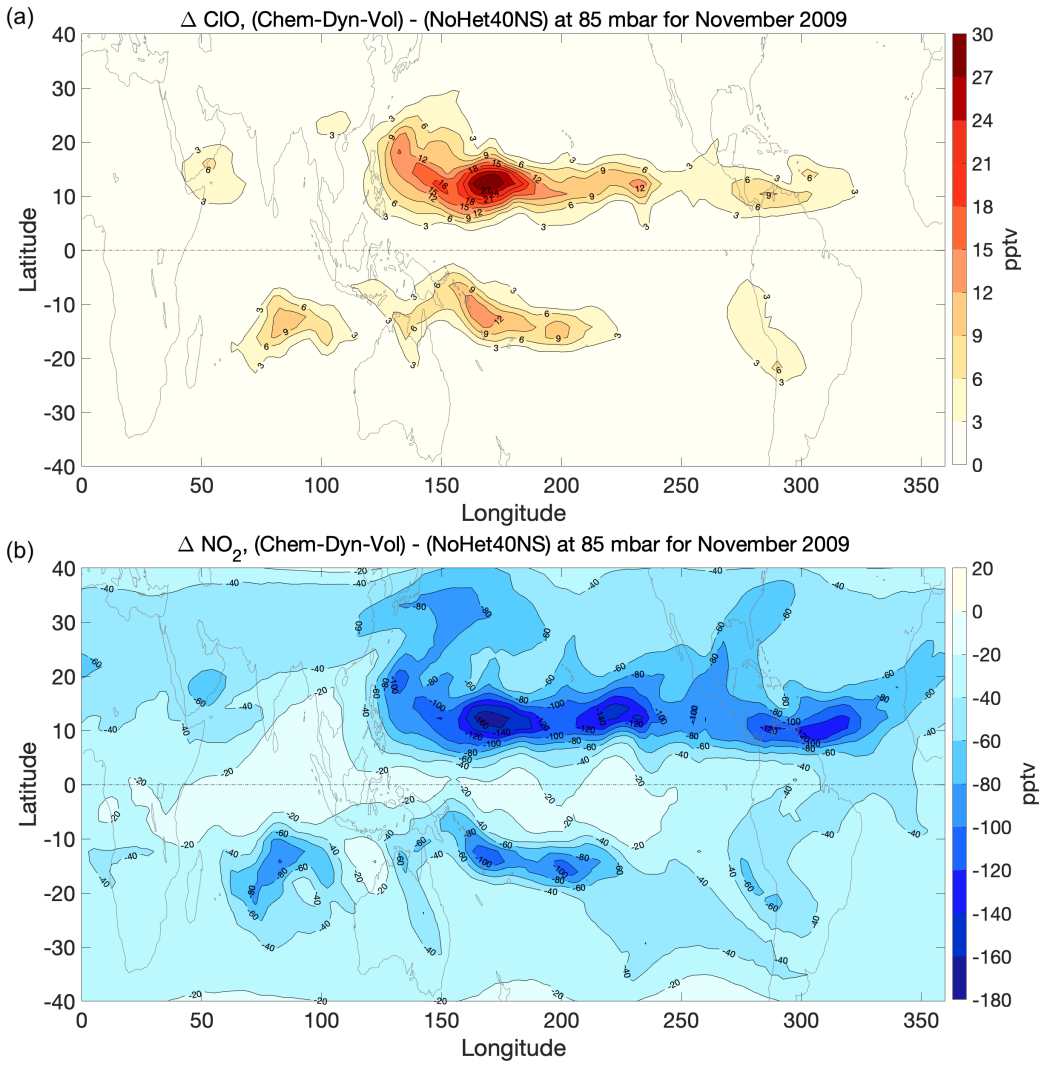

Figure 3-4: Differences in the monthly mean distribution of **(a)** ClO and **(b)** NO_2 at 85 hPa in SD-WACCM between the runs with and without heterogeneous chlorine and bromine chemistry turned on in the tropics. Red values indicate relative enhancement, and blue values indicate relative depletion.

hPa for November 2009: enhancement in ClO in Figure 3-4a and depletion in NO_2 in Figure 3-4b. As ClO is both a product of the heterogeneous reactions of interest and has very low background levels in the tropics and subtropics, it presents the clearest view of the activation response. Figure 3-S3 compares calculations with heterogeneous chemistry turned on and off to isolate the in situ chemical enhancement from dynamical transport; the figure shows that heterogeneous chemistry enhances ClO from unperturbed levels of 1 pptv or less in the tropics in the absence of

heterogeneous chemistry to above 25 pptv in the Northern Hemisphere lobe and above 12 pptv in the Southern Hemisphere lobe; such high levels of ClO are not normally present equatorward of about $\pm 60^\circ$ in the months in question. While ClO provides the cleanest signal for chemical activation, NO_2 is a more commonly observable species due to its higher background mixing ratios. Figure 3-4b shows the expected response in NO_2, of opposite sign to that of ClO, due to the recombination of NO_2 with ClO and subsequent conversion to HNO_3. It is especially illuminating to note how the pattern of chlorine activation curls around with the winds of the anticyclones. In the Southern Hemisphere in particular, there is a marked decrease in activation near the center of the anticyclone off the northeast coast of Australia. We see continued but decreasing elevated levels in a west–east band across the Pacific. Examination of the reaction rates of the three main heterogeneous chlorine activation reactions described above ($HCl + ClONO_2 \rightarrow Cl_2 + HNO_3$, $H_2O + ClONO_2 \rightarrow HOCl + HNO_3$, and $HCl + HOCl \rightarrow H_2O + Cl_2$) in Figure 3-S4 confirms that the in situ activation is driven by a combination of available chlorine and cold temperatures, with the former limiting activation on the equatorward side and the later limiting it on the poleward side. Both ClO and NO_2 changes span somewhat larger regions than the chemical rates; this is likely associated with advection by the equatorward edges of the subtropical jets or the Kelvin wave part of the Matsuno–Gill wind response. NO_2 changes show a broader pattern than ClO, reflecting the former's longer lifetime in the stratosphere and thus ability to be carried by the circulation. There is more activation in the Northern Hemisphere than in the Southern Hemisphere, consistent with the more extensive region of cold temperatures there. It is notable that there is little enhancement of chlorine activation over the equator proper despite the cold temperatures, as the meridional transport of chlorine from higher latitudes weakens dramatically there, in accordance with the Matsuno–Gill meridional wind response vanishing at the equator for symmetric heating.

Although the longitudinally resolved plots give the clearest demonstration of the implications of a Matsuno–Gill type flow for stratospheric chemistry, this activation signal can also be seen in the zonal mean in both ClO and NO_2. Figures 3-5a and 3-5b

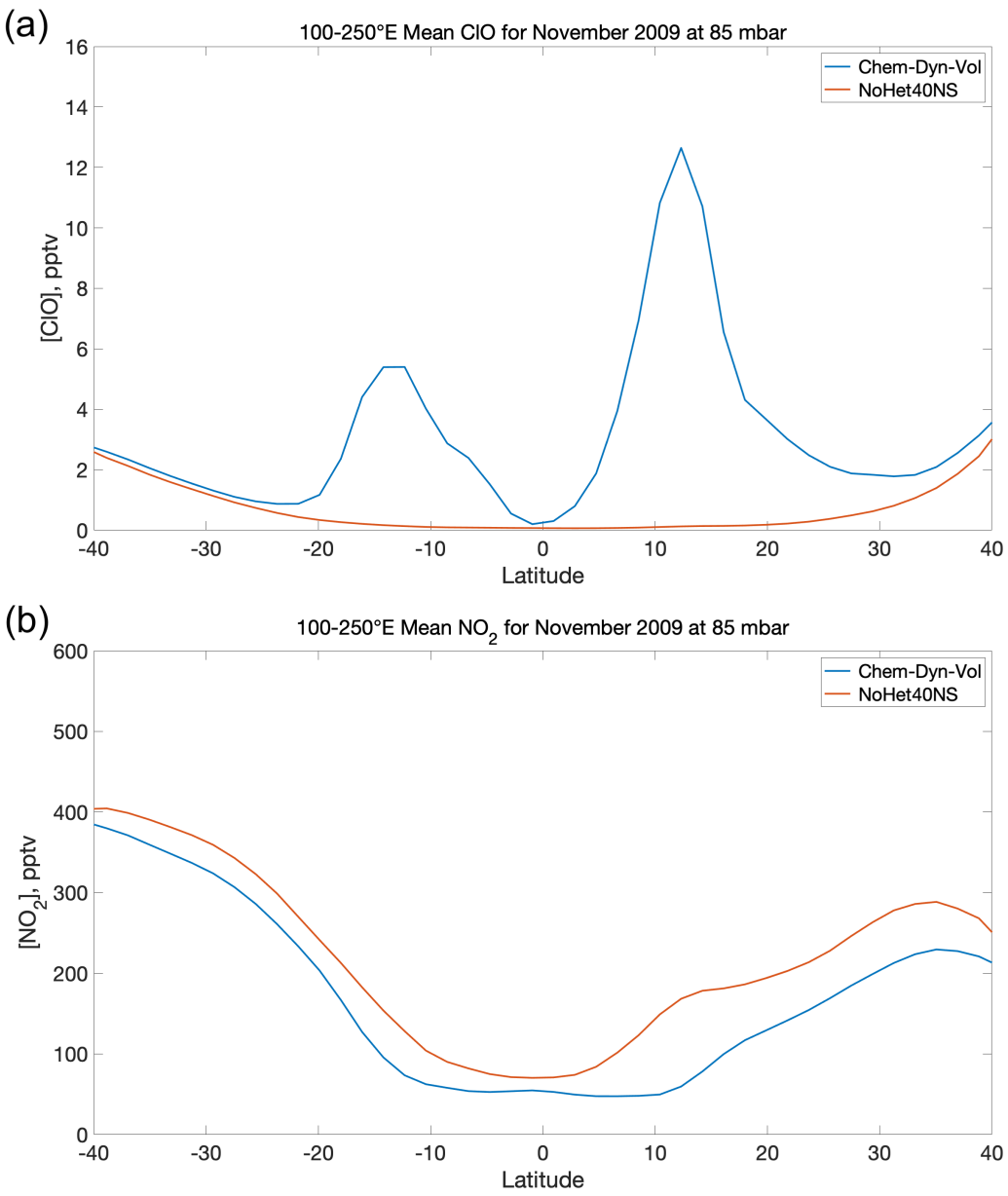

Figure 3-5: Monthly longitudinal means from 100° to 250°E for **(a)** ClO and **(b)** NO_2 in SD-WACCM at 85 hPa from 40°S to 40°N for November 2009. The blue line is the Chem-Dyn-Vol run with full heterogeneous chemistry turned on, and the red line is the NoHet40NS run with heterogeneous chlorine and bromine chemistry turned off in the tropics.

show the ClO and NO_2 mixing ratios for November 2009 at 85 hPa for the Chem-Dyn-Vol run and the NoHet40NS run. A partial zonal mean from 100° to 250°E emphasizes the region of interest while excluding the influence of the continental landmasses, but

the same features are present in the full zonal mean (Figure 3-S5) despite dilution from chemically quiescent longitudes. ClO shows an extremely clear dual hemisphere enhancement, stronger in the Northern Hemisphere, with background levels nearly zero in the absence of heterogeneous chemistry. NO_2 has a more pronounced hemispheric asymmetry, although the signal is present in both. The feature in NO_2 near 10°N is especially significant, as the Chem-Dyn-Vol mixing ratio of ∼60 pptv, compared to the NoHet40NS concentration of ∼200 pptv, should be observable. Perturbations are even larger at some longitudes as shown in Figure 3-4.

3.4 Discussion

We find clear signals of enhancement in ClO and depletion in NO_2 in SD-WACCM in the tropical lower stratosphere in months near the equinoxes due to the presence of heterogeneous chemistry on liquid sulfuric acid aerosols. We present results from November 2009 and find similar patterns in several other months as well, as shown in the ClO differences over the entire time series (Figure 3-S6). In particular, November 2011 (Figure 3-S6d), December 2011 (Figure 3-S6a), April 2009 (Figure 3-S6b), and April 2011 (Figure 3-S6b) show double bull's-eyes. Boreal summer (Figure 3-S6c) and austral summer (Figure 3-S6a) are both dominated by single-hemisphere enhancements associated with their monsoons. The strong East Asian summer monsoon anticyclone leads to the largest chlorine enhancement of these asymmetric heating responses, supporting what was previously found in Solomon et al. (2016). It is worth noting that, while November 2010–January 2011 have very high enhancement, the Merapi volcano erupted at the end of October 2010, increasing the aerosol surface areas and heterogeneous reaction rates, and likely dominates the signal for months.

We have systematically traced the chlorine activation back to the effects of a Matsuno–Gill circulation pattern caused by diabatic heating in equatorial regions of the western Pacific. This circulation pattern includes anticyclones in the lower stratosphere of both hemispheres that entrain chlorine to lower latitudes, as well as very cold lower-stratospheric temperatures overlying regions where the tropopause

is high. Winds and temperatures combine to drive efficient heterogeneous chlorine activation. The changes in ClO and NO_2 background mixing ratios provide a testable signature of this mechanism that should be visible to future measurement campaigns in the region, particularly using airborne instruments. Unfortunately, the current generation of chemistry-focused satellites does not measure ClO in the tropical UTLS, but, should that change, this pattern should also be visible on a large scale as seen in the model. While the differences between the SD-WACCM runs we present successfully isolate the signal of chlorine activation due to heterogenous reactions, the underlying meteorological fields and thus the Matsuno–Gill circulations are the same for all runs. To quantify the importance of these for transporting chlorine, runs with modified dynamics that suppress the Matsuno–Gill response would be required. While such comparisons are beyond the scope of the present study, they could be a useful component of future ones.

Although the years we look at in this study were devoid of major volcanic eruptions, in the past decade numerous studies have shown that aerosols from the more frequent, moderate-sized volcanoes have a discernible impact on many aspects of stratospheric chemistry (Solomon et al. 2011; Naik et al. 2017; Adams et al. 2017; Wilka et al. 2018). Sarychev Peak erupted in June 2009 and lofted measurable sulfur to the stratosphere, so November 2009 was not "volcanically clean." Nor was 2011, due to the Nabro eruption in June of that year. However, as volcanically clean years seem to be more the exception than the rule (Mills et al. 2016; Vernier et al. 2011), at least in recent decades, 2009 may be a fairly typical year in terms of tropical sulfate levels.

The model chemistry relies on several assumptions about heterogeneous chemistry whose validity could impact our results. The parameterized heterogeneous activation rates are based on laboratory studies that contain few direct measurements at the coldest temperatures and have not been updated for almost two decades. Furthermore, these studies assumed pure liquid H_2O/H_2SO_4 mixtures, so that the effects of freezing and of any doping with pollutant nitrates or organics are poorly constrained. The extent to which these matter in the real world depends on both the

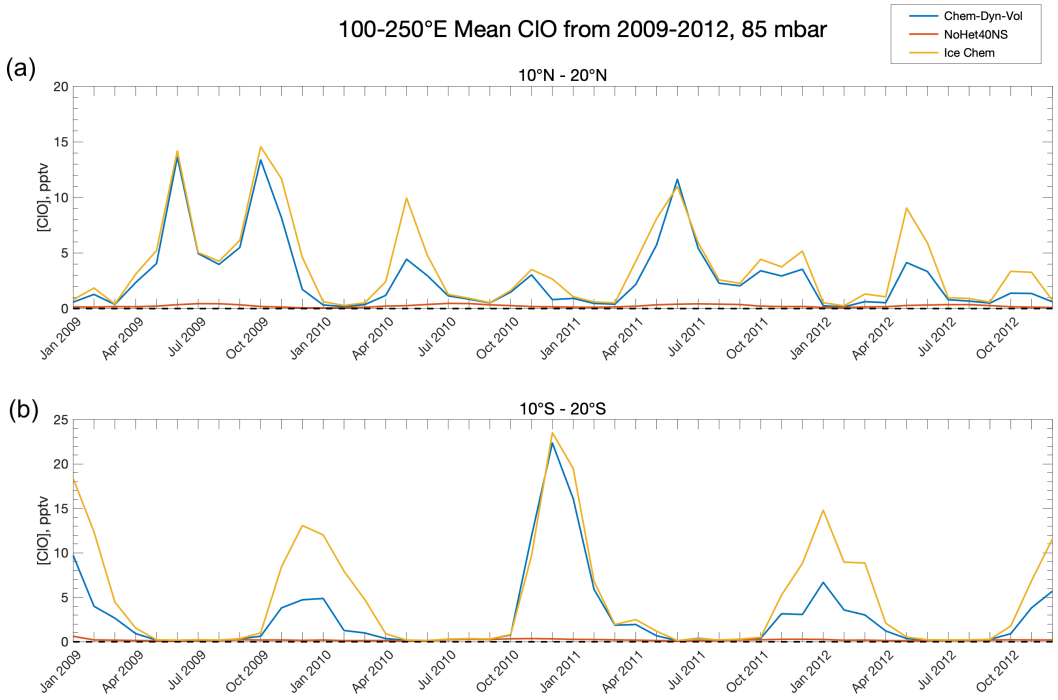

Figure 3-6: Time series of monthly mean ClO over the Pacific Ocean in the **(a)** Northern Hemisphere and **(b)** Southern Hemisphere tropics. Latitude bands are chosen to maximize the activation signal and isolate inter-hemispheric differences. The blue line is the Chem-Dyn-Vol run with full heterogeneous chemistry turned on but no ice chemistry, the red line is the NoHet40NS run with heterogeneous chlorine and bromine chemistry turned off in the tropics, and the yellow line is the Ice Chem run with full heterogeneous chemistry and an additional ice chemistry parameterization included.

aerosol composition of the tropical lower stratosphere and the degree to which sulfates are internally versus externally mixed with other species. The degree of accuracy with which models capture relevant stratospheric aerosol processes and composition changes is an area of active research (Kremser et al. 2016, and references therein). One recent study (Höpfner et al. 2019) found elevated levels of solid ammonium nitrate in the upper troposphere during the Asian summer monsoon due to convective uplift of NH_3. However, they did not find elevated ammonium nitrate outside of the summer monsoon months, that is, for the months of interest here. Further, sulfate aerosols can be expected to be dominant in volcanically perturbed periods.

While the version of SD-WACCM we use does not account for heterogeneous

chemistry on cirrus ice cloud particles, we expect such reactions to enhance our modeled activation. Cirrus chemistry parameterizations are subject to large uncertainties, but we test our expectation by running SD-WACCM with an ice chemistry parameterization implemented for the four years of interest and plot the ClO mixing ratios in Figure 3-6 along with the Chem-Dyn-Vol and NoHet40NS runs for the same Pacific region of interest as Figure 3-5. We see in Figure 3-6 that ice chemistry increases activation, as expected, but the magnitude of its impact varies greatly both among years and between hemispheres. For November 2009, ice chemistry appears to enhance ClO more in the Southern Hemisphere (Figure 3-6b) than the Northern Hemisphere (Figure 3-6a), but in November 2010 there is little effect in either hemisphere. The relative importance of cirrus clouds is an ongoing area of study, but it is important to note that the enhancements seen in Figure 3-6, regardless of season, occur in addition to activation caused by liquid sulfuric acid aerosols, and we do not see any significant enhancements in the absence of liquid sulfuric acid aerosol-driven activation. Thus, we feel confident that our results capture the main features of chlorine activation in the tropical UTLS, even without considering cirrus input.

An additional source of uncertainty in the model results comes from the adopted temperature profiles. MERRA temperatures near the tropopause, to which SD-WACCM is relaxed, assimilate both satellite and in situ observations, so we expect that they capture the mean structure well. However, the number of levels in the UTLS is relatively small, and may fail to capture some of the variance in temperature structure often seen in higher vertical resolution radiosondes, especially due to situations such as a double-peaked cold point tropopause or small-scale wave activity. We recognize that this smoothing of the temperature structure will mute some of the corresponding vertical structure in the chemistry, and in particular may underestimate activation if the cold point occurs between model levels. This is an active area for further research and the importance of temperature resolution for chemistry could inform considerations of future subgrid-scale modeling parameterizations, as well as be a target of investigation for higher-resolution models.

Another promising direction for further exploration is the role that wave activity on different time scales has on the likelihood and lifetime of the patterns that we investigate here. Tropical winds, temperatures, and resultant chemistry patterns are influenced from year-to-year by El Niño–Southern Oscillation and the Quasi-Biennial Oscillation, and on subseasonal time scales by the Madden–Julian Oscillation (MJO) and mixing from midlatitude eddies. As we have examined only a monthly-mean response, we recognize that on shorter time scales the activation could be both stronger and more localized. This is especially likely in the case of modulation of convection by the MJO, which varies in location over its cycle and in strength between different events. While it is intriguing that 2009 and 2011 both seem to display more activation in fall and spring (Figure 3-S6), the current study does not span enough years to determine what dynamical phases or combinations thereof are most responsible for influencing chemistry. A systematic investigation of a longer time series could also help quantify the influence of summer monsoonal circulations of varying strength on this chemistry. Quantifying how both the background state of the atmosphere and the activity of more transient phenomena influence the likelihood of finding these patterns is an area of ongoing investigation.

3.5 Conclusions

This study has expanded our knowledge of where heterogeneous chlorine activation chemistry can take place in months near the equinoxes and has revealed new connections between tropical meteorology and stratospheric chemistry. The ClO and NO_2 levels that we have modeled provide observable targets for future aircraft campaigns or satellites focused on the tropical UTLS. For example, measurements of the anomalies seen in both hemispheres (as in Figure 3-4) would serve as a characteristic signature of the response as described here. Such campaigns could also use this chemistry to deepen our understanding of the stratospheric equatorially symmetric Matsuno–Gill circulation and transport patterns, with chemical enhancements providing observable indicators for dynamical studies.

Furthermore, while we have focused on the heterogeneous chlorine reactions most relevant for ozone depletion in this region, it is notable that other chemical constituents and processes will also be affected. For example, all reactants with a steep equator-to-pole concentration gradient are expected to be affected by the Matsuno–Gill wind pattern described here. Reactions with a sufficiently strong temperature sensitivity will also be influenced. For both chlorine-dependent and other reactions, continuing to investigate the impacts of zonally asymmetric circulation patterns on atmospheric chemistry is an area that is ripe for further research.

3.6 Supplemental Figures

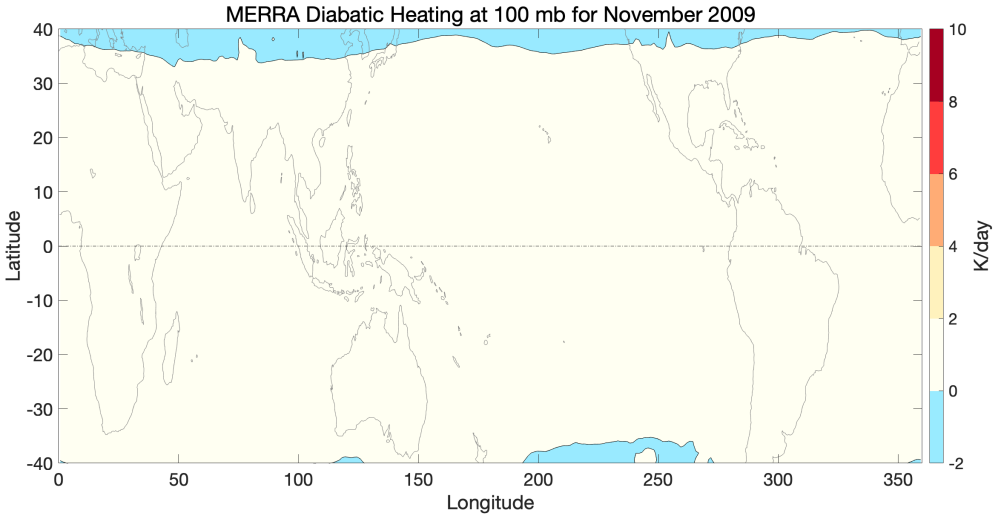

Figure 3-S1: Same as Figure 3-1b, but for 100 mbar.

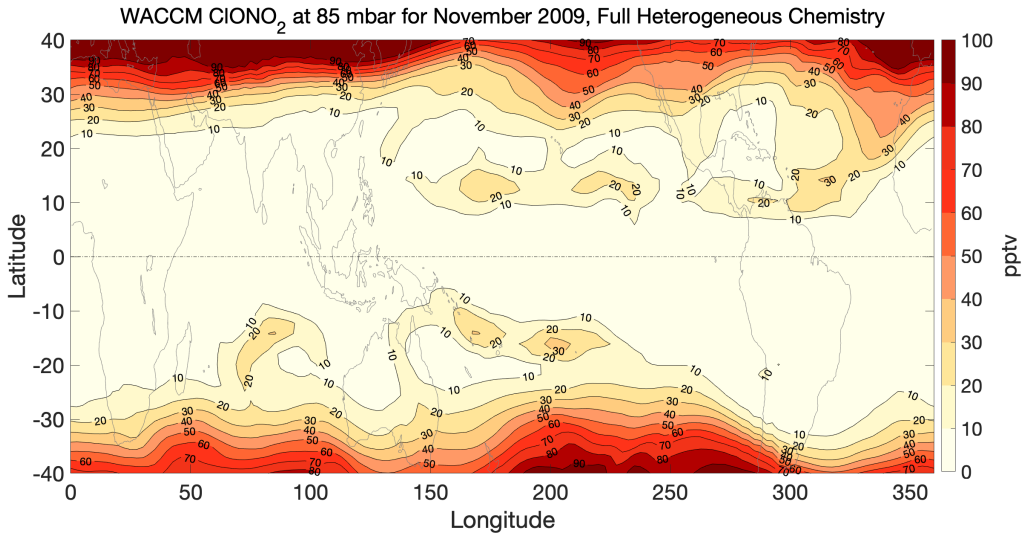

Figure 3-S2: Monthly mean SD-WACCM $ClONO_2$ volume mixing ratios at 85 mbar in the tropics for November 2009. Heterogeneous chemistry is turned on at all latitudes.

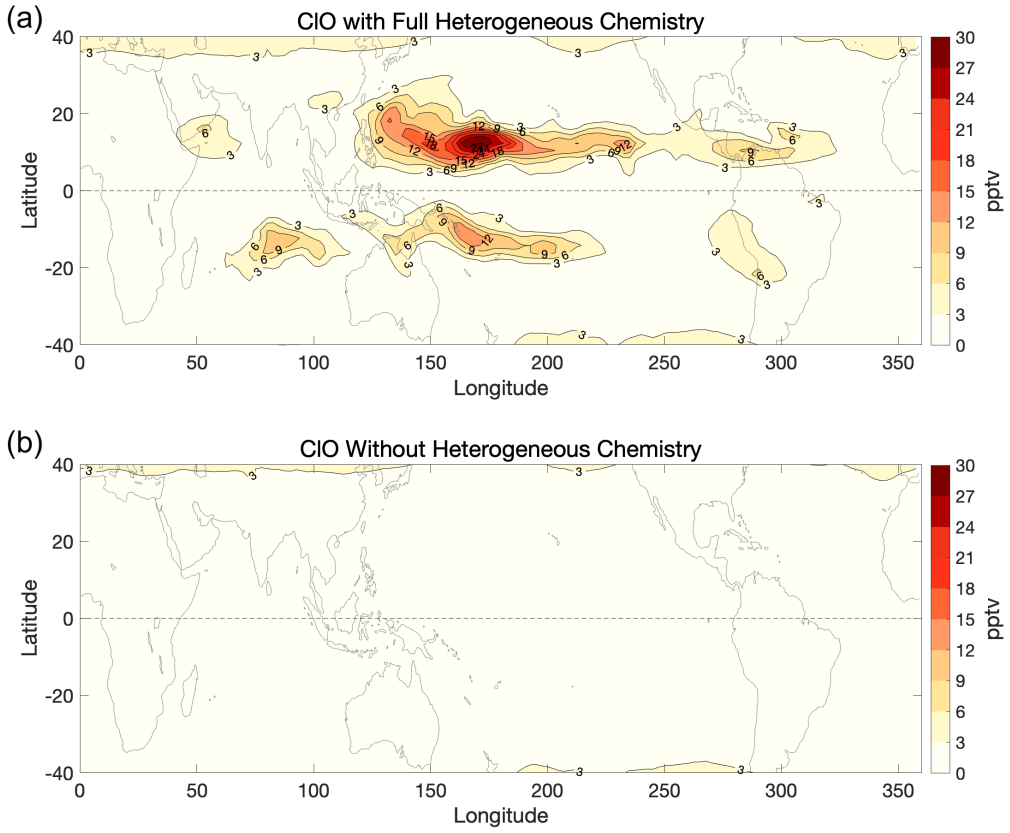

Figure 3-S3: ClO mixing ratios in pptv from 40°N to 40°S for November 2009 at 85 mbar for **(a)** the Chem-Dyn-Vol run with full heterogeneous chemistry and **(b)** the NoHet40NS run with heterogeneous chlorine and bromine chemistry turned off in the tropics.

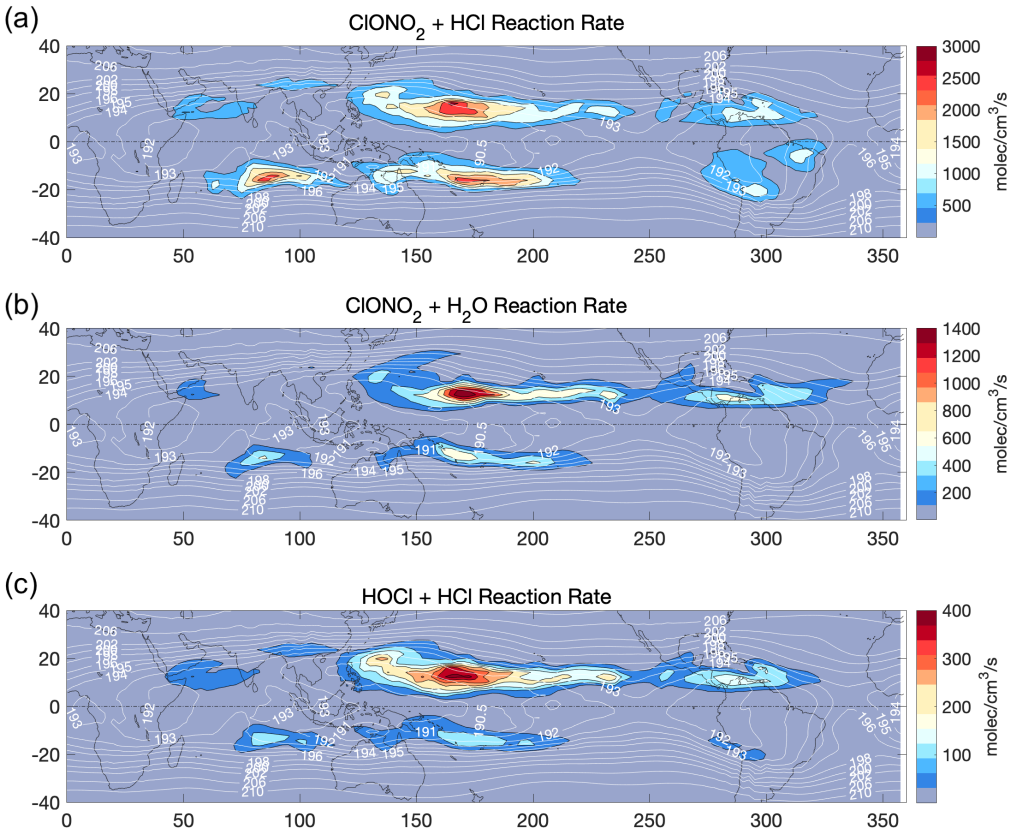

Figure 3-S4: Monthly mean reaction rates for **(a)** $HCl + ClONO_2 \rightarrow Cl_2 + HNO_3$, **(b)** $H_2O + ClONO_2 \rightarrow HOCl + HNO_3$, and **(c)** $HCl + HOCl \rightarrow H_2O + Cl_2$ reactions for the tropics for November 2009 at 85 mbar. The thin white background lines show temperature contours. Note the different scales on the colorbars.

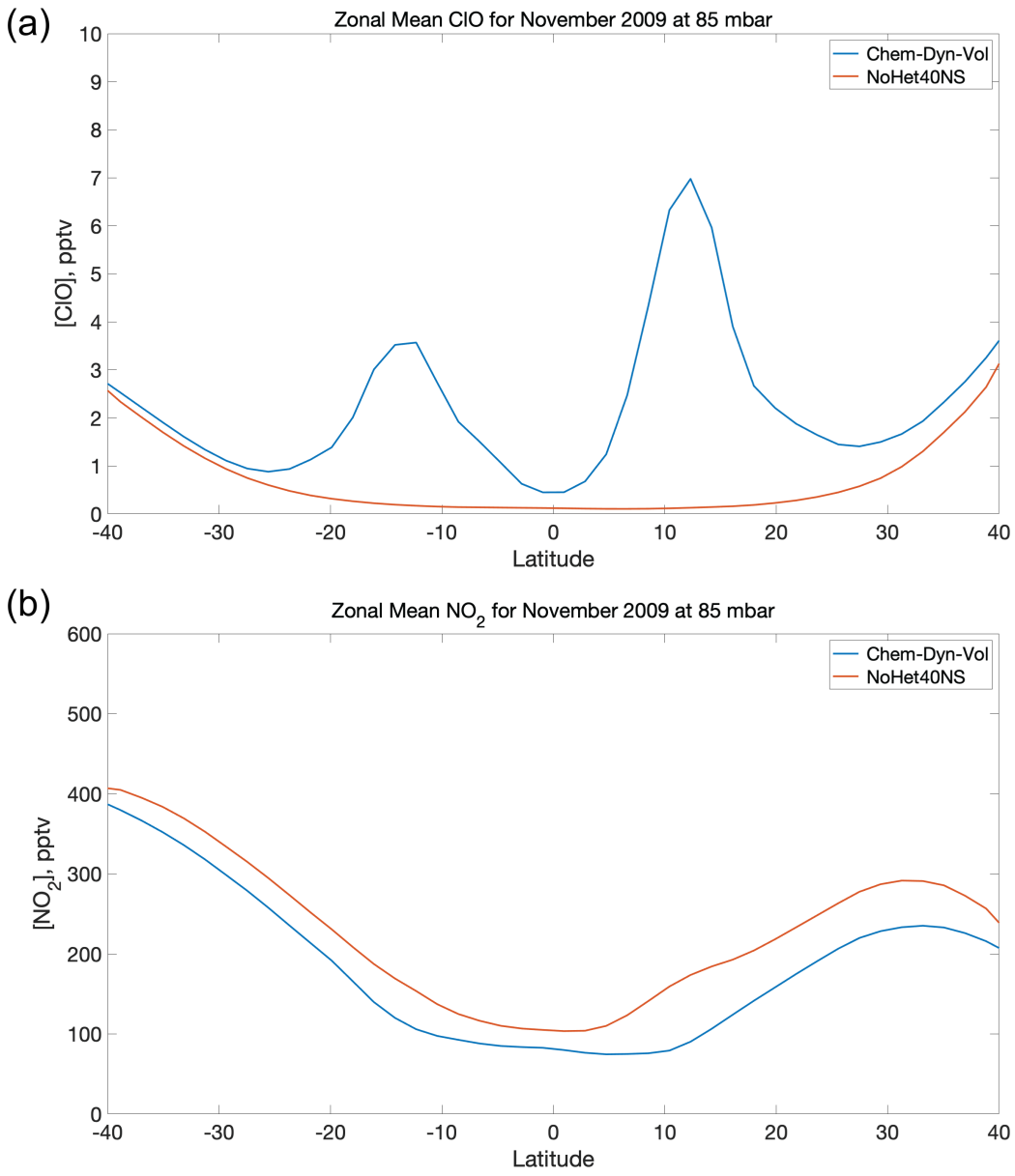

Figure 3-S5: Same as Figure 3-5, but for the full zonal mean.

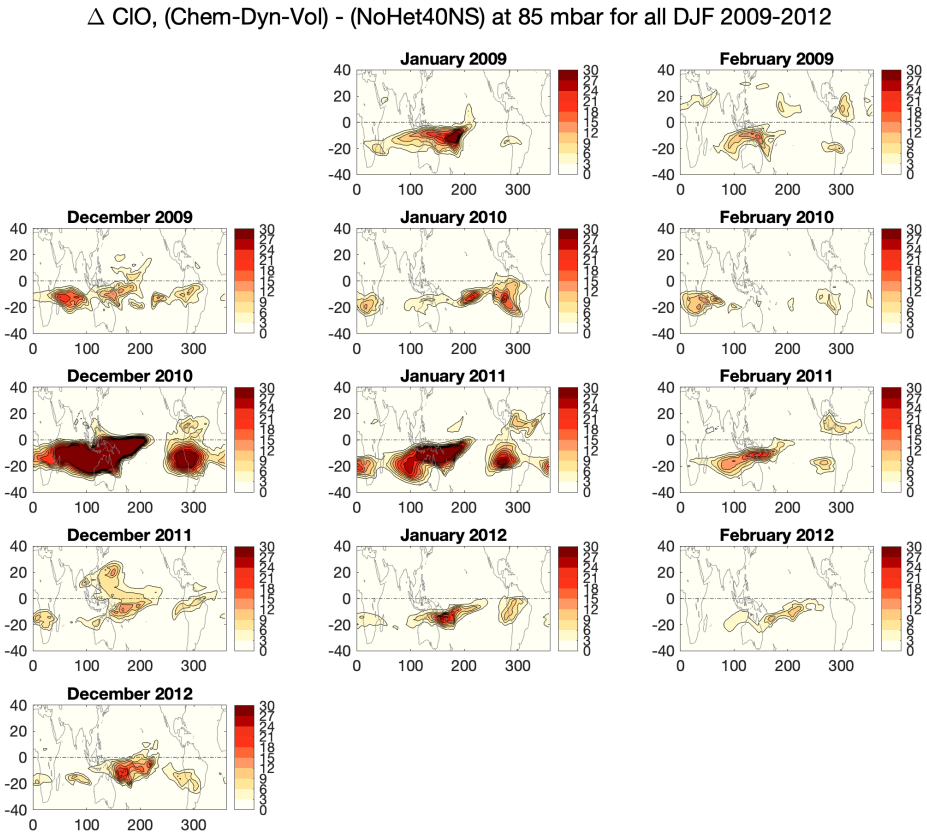

Figure 3-S6a: Same as Figure 3-4a, but for every month in DJF.

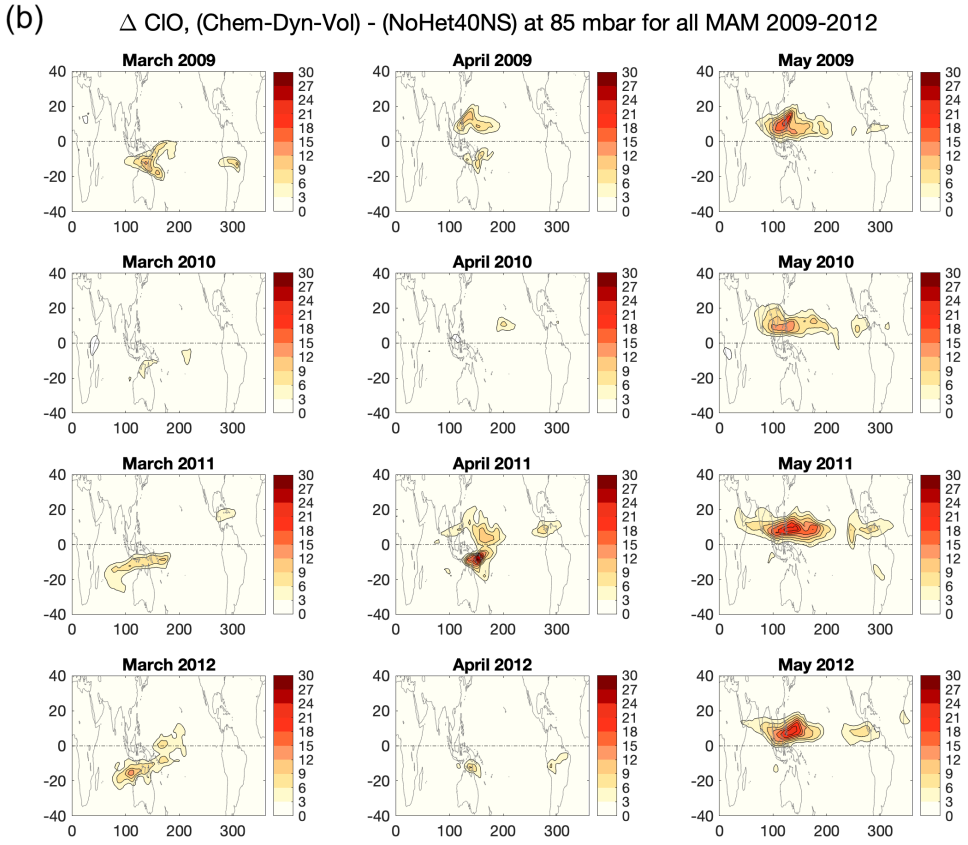

Figure 3-S6b: Same as Figure 3-4a, but for every month in MAM.

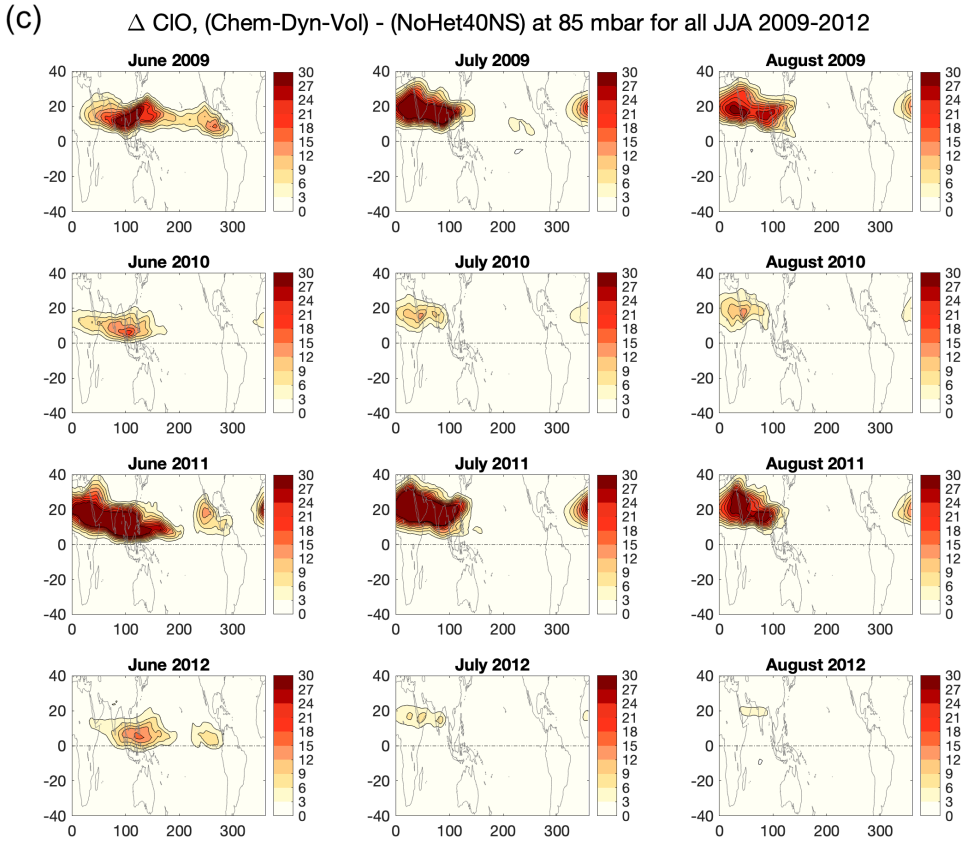

Figure 3-S6c: Same as Figure 3-4a, but for every month in JJA.

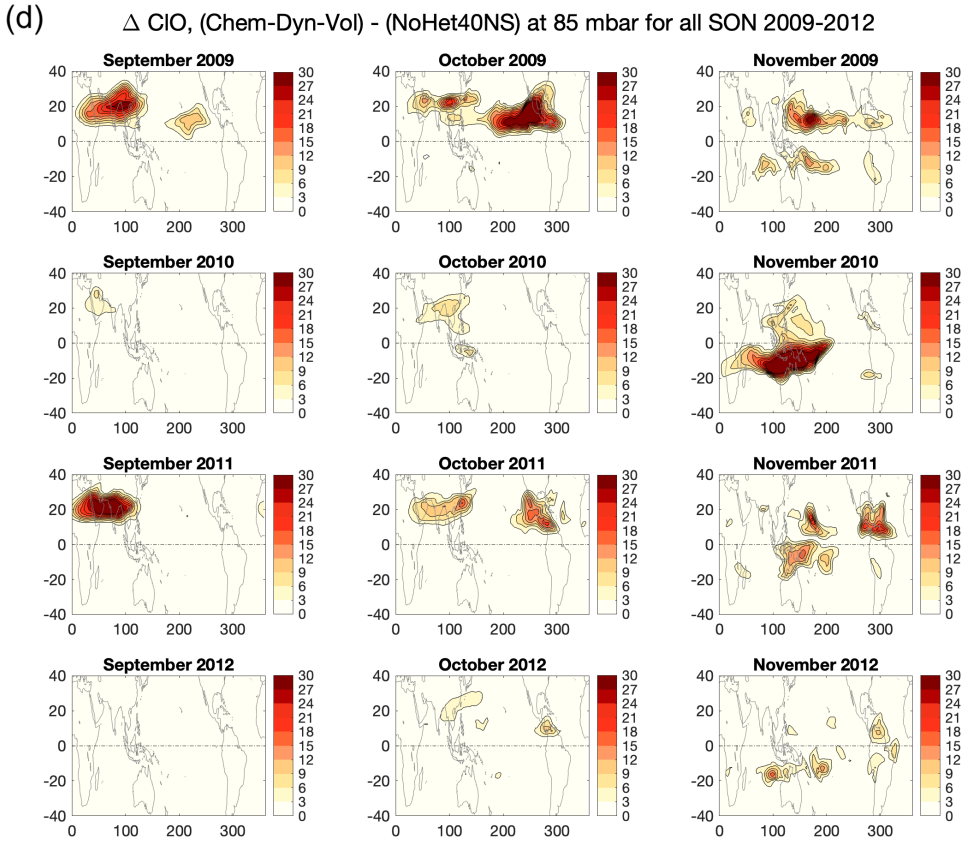

Figure 3-S6d: Same as Figure 3-4a, but for every month in SON.

References

[1] Adames, Á. F., & Wallace, J. M. (2017). On the tropical atmospheric signature of El Niño. *Journal of the Atmospheric Sciences, 74*(6), 1923–1939. https://doi.org/10.1175/JAS-D-16-0309.1

[2] Adams, C., Bourassa, A. E., McLinden, C. A., Sioris, C. E., Clarmann, T. V., Funke, B., ... & Degenstein, D. A. (2017). Effect of volcanic aerosol on stratospheric NO_2 and N_2O_5 from 2002–2014 as measured by Odin-OSIRIS and Envisat-MIPAS. *Atmospheric Chemistry and Physics, 17*(13), 8063–8080. https://doi.org/10.5194/acp-17-8063-2017

[3] Adler, R. F., Huffman, G. J., Chang, A., Ferraro, R., Xie, P. P., Janowiak, J., ... & Nelkin, E. (2003). The version-2 global precipitation climatology project (GPCP) monthly precipitation analysis (1979–present). *Journal of Hydrometeorology, 4*(6), 1147–1167. https://doi.org/10.1175/1525-7541(2003)004<1147:TVGPCP>2.0.CO;2

[4] Anderson, J. G., Weisenstein, D. K., Bowman, K. P., Homeyer, C. R., Smith, J. B., Wilmouth, D. M., ... & Wofsy, S. C. (2017). Stratospheric ozone over the United States in summer linked to observations of convection and temperature via chlorine and bromine catalysis. *Proceedings of the National Academy of Sciences, 114*(25), E4905–E4913. https://doi.org/10.1073/pnas.1619318114

[5] Froidevaux, L., Kinnison, D. E., Wang, R., Anderson, J., & Fuller, R. A. (2019). Evaluation of CESM1 (WACCM) free-running and specified dynamics atmospheric composition simulations using global multispecies satellite data records. *Atmospheric Chemistry and Physics, 19*(7), 4783–4821. https://doi.org/10.5194/acp-19-4783-2019

[6] Gill, A. E. (1980). Some simple solutions for heat-induced tropical circulation. *Quarterly Journal of the Royal Meteorological Society, 106*(449), 447–462. https://doi.org/10.1002/qj.49710644905

[7] Highwood, E. J., & Hoskins, B. J. (1998). The tropical tropopause. *Quarterly Journal of the Royal Meteorological Society, 124*(549), 1579–1604. https://doi.org/10.1002/qj.49712454911

[8] Höpfner, M., Ungermann, J., Borrmann, S., Wagner, R., Spang, R., Riese, M., ... & Wohltmann, I. (2019). Ammonium nitrate particles formed in upper troposphere from ground ammonia sources during Asian monsoons. *Nature Geoscience, 12*(8), 608–612. https://doi.org/10.1038/s41561-019-0385-8

[9] Jin, F., & Hoskins, B. J. (1995). The direct response to tropical heating in a baroclinic atmosphere. *Journal of the Atmospheric Sciences, 52*(3), 307–319. https://doi.org/10.1175/1520-0469(1995)052<0307:TDRTTH>2.0.CO;2

[10] Kremser, S., Thomason, L. W., von Hobe, M., Hermann, M., Deshler, T., Timmreck, C., ... & Meland, B. (2016). Stratospheric aerosol — Observations, processes, and impact on climate. *Reviews of Geophysics, 54*(2), 278–335. https://doi.org/10.1002/2015RG000511

[11] Marsh, D. R., Mills, M. J., Kinnison, D. E., Lamarque, J. F., Calvo, N., & Polvani, L. M. (2013). Climate change from 1850 to 2005 simulated in CESM1 (WACCM). *Journal of Climate, 26*(19), 7372–7391. https://doi.org/10.1175/JCLI-D-12-00558.1

[12] Matsuno, T. (1966). Quasi-geostrophic motions in the equatorial area. *Journal of the Meteorological Society of Japan. Ser. II, 44*(1), 25–43. https://doi.org/10.2151/jmsj1965.44.1_25

[13] Mills, M. J., Schmidt, A., Easter, R., Solomon, S., Kinnison, D. E., Ghan, S. J., et al. (2016). Global volcanic aerosol properties derived from emissions, 1990–2014, using CESM1 (WACCM). *Journal of Geophysical Research: Atmospheres, 121*(5), 2332–2348. https://doi.org/10.1002/2015JD024290

[14] Mills, M. J., Richter, J. H., Tilmes, S., Kravitz, B., MacMartin, D. G., Glanville, A. A., ... & Kinnison, D. E. (2017). Radiative and chemical response to interactive stratospheric sulfate aerosols in fully coupled CESM1 (WACCM). *Journal of Geophysical Research: Atmospheres, 122*(23), 13–061. https://doi.org/10.1002/2017JD027006

[15] Naik, V., Horowitz, L. W., Daniel Schwarzkopf, M., & Lin, M. (2017). Impact of volcanic aerosols on stratospheric ozone recovery. *Journal of Geophysical Research: Atmospheres, 122*(17), 9515–9528. https://doi.org/10.1002/2016JD025808

[16] Neely III, R. R., & Schmidt, A. (2016). VolcanEESM: Global volcanic sulphur dioxide (SO_2) emissions database from 1850 to present—Version 1.0. Centre for Environmental Data Analysis, 4 February 2016.

[17] Newell, R. E., & Gould-Stewart, S. (1981). A stratospheric fountain?. *Journal of Atmospheric Sciences, 38*(12), 2789–2796. https://doi.org/10.1175/1520-0469(1981)038<2789:ASF>2.0.CO;2

[18] Rienecker, M. M., Suarez, M. J., Gelaro, R., Todling, R., Bacmeister, J., Liu, E., ... & Woollen, J. (2011). MERRA: NASA's modern-era retrospective analysis for research and applications. *Journal of Climate, 24*(14), 3624–3648. https://doi.org/10.1175/JCLI-D-11-00015.1

[19] Robrecht, S., Vogel, B., Grooß, J. U., Rosenlof, K., Thornberry, T., Rollins, A., ... & Müller, R. (2019). Mechanism of ozone loss under enhanced water vapour conditions in the mid-latitude lower stratosphere in summer. *Atmospheric Chemistry and Physics, 19*(9), 5805–5833. https://doi.org/10.5194/acp-19-5805-2019

[20] Rodwell, M. J., & Hoskins, B. J. (2001). Subtropical anticyclones and summer monsoons. *Journal of Climate, 14*(15), 3192–3211. https://doi.org/10.1175/1520-0442(2001)014<3192:SAASM>2.0.CO;2

[21] Shi, Q., Jayne, J. T., Kolb, C. E., Worsnop, D. R., & Davidovits, P. (2001). Kinetic model for reaction of $ClONO_2$ with H_2O and HCl and HOCl with HCl in sulfuric acid solutions. *Journal of Geophysical Research: Atmospheres, 106*(D20), 24259–24274. https://doi.org/10.1029/2000JD000181

[22] Solomon, S. (1999). Stratospheric ozone depletion: A review of concepts and history. *Reviews of Geophysics, 37*(3), 275–316. https://doi.org/10.1029/1999RG900008

[23] Solomon, S., Garcia, R. R., Rowland, F. S., & Wuebbles, D. J. (1986). On the depletion of Antarctic ozone. *Nature, 321*(6072), 755–758. https://doi.org/10.1038/321755a0

[24] Solomon, S., Daniel, J. S., Neely, R. R., Vernier, J. P., Dutton, E. G., & Thomason, L. W. (2011). The persistently variable "background" stratospheric aerosol layer and global climate change. *Science, 333*(6044), 866–870. https://doi.org/10.1126/science.1206027

[25] Solomon, S., Kinnison, D., Garcia, R. R., Bandoro, J., Mills, M., Wilka, C., ... & Höpfner, M. (2016). Monsoon circulations and tropical heterogeneous chlorine chemistry in the stratosphere. *Geophysical Research Letters, 43*(24), 12–624. https://doi.org/10.1002/2016GL071778

[26] Vernier, J. P., Thomason, L. W., Pommereau, J. P., Bourassa, A., Pelon, J., Garnier, A., ... & Vargas, F. (2011). Major influence of tropical volcanic eruptions on the stratospheric aerosol layer during the last decade. *Geophysical Research Letters, 38*(12). https://doi.org/10.1029/2011GL047563

[27] Wilka, C., Shah, K., Stone, K., Solomon, S., Kinnison, D., Mills, M., ... & Neely III, R. R. (2018). On the role of heterogeneous chemistry in ozone depletion and recovery. *Geophysical Research Letters, 45*(15), 7835-7842. https://doi.org/10.1029/2018GL078596.

[28] Wilka, C., Solomon, S., Cronin, T. W., Kinnison, D., & Garcia, R. (2021). Atmospheric Chemistry Signatures of an Equatorially Symmetric Matsuno–Gill Circulation Pattern. *Journal of the Atmospheric Sciences, 78*(1), 107–116. https://doi.org/10.1175/JAS-D-20-0025.1

Chapter 4

An Arctic Ozone Hole in 2020 If Not For the Montreal Protocol

Abstract

This chapter presents results from a "World Avoided" (WA) study, a term used in the literature to refer to simulations of alternate scenarios where the Montreal Protocol was never passed and CFCs continued to increase. Previous WA studies have looked at general ozone trends and past meteorologically extreme years: here we examine such a scenario for 2020 for the first time. Without the Montreal Protocol the already extreme Arctic ozone losses in boreal spring of 2020 would be expected to have produced an Antarctic-like ozone hole, based upon simulations performed using the Specified Dynamics version of the Whole Atmosphere Community Climate Model (SD-WACCM). In particular, the area of total ozone below 220 DU, a standard metric of Antarctic ozone hole size, would have covered about 20 million km^2. Record observed local low concentrations of 0.1 ppmv at some altitudes in the lower stratosphere seen by ozonesondes in March 2020 would have reached 0.01 ppmv, again similar to the Antarctic. Spring ozone depletion would have begun earlier and lasted longer without the Montreal Protocol, and by 2020 the year-round ozone depletion would have begun to dramatically diverge

This chapter is currently under review in Atmospheric Chemistry and Physics at `https://acp.copernicus.org/preprints/acp-2020-1297/`

from the observed case. This extreme year also provides an opportunity to test parameterizations of polar stratospheric cloud impacts on denitrification, and thereby to improve stratospheric models of both the real world and alternate scenarios. In particular, we find that decreasing the parameterized nitric acid trihydrate number density in SD-WACCM, which subsequently increases denitrification, improves the agreement with observations for both nitric acid and ozone. This study reinforces that the historically extreme 2020 Arctic ozone depletion is not cause for concern over the Montreal Protocol's effectiveness, but rather demonstrates that the Montreal Protocol indeed merits celebration for avoiding an Arctic ozone hole.

4.1 Introduction

In the 1970s, Molina and Rowland issued a prescient warning to humanity that the chlorofluorocarbons (CFCs) contained in popular refrigerants, building foams, and aerosol cans posed a danger to the stratospheric ozone layer (Molina and Rowland, 1974). This threat, initially thought to be a worry for the next century, suddenly transformed into a pressing concern with the discovery of unexpected, deep springtime depletion in the Antarctic polar vortex (Farman et al., 1985), which became known to the world as the "ozone hole." Subsequent work (Solomon et al., 1986) revealed that heterogeneous chemical reactions involving chlorine and bromine on the cold surfaces of Polar Stratospheric Clouds (PSCs) were the missing link in the sequence of steps leading to this deep depletion. PSCs are made of water ice, nitric acid trihydrate (NAT), or supercooled ternary solutions of water, nitric acid, and sulfur (STS), and several studies have highlighted a significant role for sedimentation of large NAT particles in the removal of HNO_3 from the lower stratosphere, or denitrification (Toon et al., 1986; Crutzen and Arnold, 1986). Definitions for what constitutes an ozone hole have been debated in the scientific literature (see Langematz et al., 2018 and references therein), but for purposes of comparison to the discovery of the Antarctic ozone hole and its impact on policy of the era, we use here the historical definition of total ozone area below 220 Dobson Units (Stolarksi et al., 1990). Another important metric

is extreme locally depleted ozone mixing ratios in the lower stratosphere (Hofmann et al., 1997), providing an important fingerprint for chemical ozone loss driven by chlorine chemistry on PSCs. In response to the increasing ozone depletion, the global community came together to pass the 1987 Montreal Protocol on Substances that Deplete the Ozone Layer, more commonly referred to as the Montreal Protocol. The Montreal Protocol, and its subsequent amendments during the 1990s, mandated the decrease and eventual cessation of worldwide production of ozone depleting substances (ODSs) such as CFCs (Birmpili, 2018).

Within the past few years, ever-stronger evidence for global ozone stabilization and a nascent Antarctic ozone recovery has emerged (Solomon et al., 2016; Sofieva et al., 2017; Chipperfield et al., 2017; Strahan and Douglass 2018). Despite uncertainties surrounding continuing CFC emissions from both scattered rogue production (Montzka et al., 2018) and existing stores in building foams and other banks (Lickley et al., 2020), the world appears to be on track for near-complete ozone recovery to near 1980s values as a result of decreasing ODSs by the second half of the 21st century (WMO 2018), and the Protocol has been ratified by every state represented at the United Nations. No other global environmental treaty can claim such a resounding success.

Success of the Montreal Protocol, however, should be measured not just by emission adherence but by the harm to the earth system and human society that its passage avoided. The first study on such a “World Avoided" (WA) by Prather et al. (1996) found strong evidence that Antarctic ozone depletion would have continued to worsen on average. Subsequent studies broadened to examine variability from year to year and at various longitudes. A decade later, Morgenstern et al. (2008) studied a WA in a more detailed three-dimensional model and found significant ozone decline in the upper stratosphere and polar vortices, a transition in the Arctic from dynamical to chemical control of ozone evolution, and major regional climate impacts caused by dynamical changes. The first fully interactive time-evolving global study of the world avoided by the Montreal Protocol, by Newman et al. (2009), found increasingly extreme impacts throughout the 21st century. Their simulations for the WA predicted

Arctic column ozone levels of 220 DU or less by 2030, with some minimum values within the vortex that low by 2020 in extreme cold years. The associated column depletion was predicted to yield a 550% increase in DNA damage when compared to 1980 by 2065 for NH midlatitudes. Chipperfield et al. (2015) examined the WA for the recent extreme cold year of 2011. They found that Arctic ozone levels would indeed have dropped below 220 DU in that year in the WA, but in a limited region which did not span the entire pole as in the Antarctic, as we discuss in Section 4.3.

The Arctic spring of 2020 displayed very cold temperatures and a stable polar vortex that led to record levels of Arctic PSCs and deep Arctic ozone depletion in the real world at some altitudes in the lower stratosphere, as has already been shown using both ozonesondes (Wohltmann et al., 2020) and satellites (Manney et al., 2020). While the classical definition of an ozone hole (a significant areal extent below 220 DU) did not occur in 2020, many news reports characterized it as such, sparking public uncertainty over whether humanity has really solved the problem of ozone depletion. Here we seek to examine the chemistry and ozone depletion of both the real world and of that obtained in a world without the Montreal Protocol to evaluate what 2020 implies for the Montreal Protocol's achievements in the context of Arctic ozone loss.

4.2 Methods and Data

4.2.1 Model

We use the Specified Dynamics version of NCAR's Whole Atmosphere Community Climate Model (SD-WACCM) to compare the ozone depletion and chemistry in a simulation of the real world (RW) to one in which ODSs continued to increase at 3.5% per year from the year 1985 onwards (WA). The assumption of 3.5% per year growth matches that used in the Garcia et al. (2012) World Avoided study and is a good approximation of the growth rates seen in years immediately prior to emissions controls, thus representing an illustrative "business as usual" alternate

trajectory. The Community Earth System Model, version 2 (CESM2) WACCM is a superset of the Community Atmosphere Model, version 6 (CAM6), which extends from the Earth's surface to the lower thermosphere (Gettelman et al., 2019). WACCM includes updated representations of boundary layer processes, shallow convection and liquid cloud macrophysics, and two-moment cloud microphysics with prognostic cloud mass and concentration (Danabasoglu et al., 2020). Aerosol representation for dust, sea-salt black carbon, organic carbon, and sulfate in three size categories is prognostic in this version (Mills et al., 2016). We use the specified dynamics (SD) version of WACCM, where the atmosphere below 50 km is nudged to the Modern-Era Retrospective Analysis for Research and Applications version 2 (MERRA-2; Gelaro et al., 2017) temperature and wind fields with a relaxation time of 50 hours. There are 88 vertical pressure grid levels from the ground to the thermosphere (∼140 km), with the altitude resolution increasing from ∼0.1 km near the surface to ∼1.0 km in the UTLS and ∼1-2 km in the stratosphere. The horizontal resolution is 1.95° × 2.5° in latitude and longitude. All model results are taken from a 24-hour average for each given day. The chemistry mechanism used in this study includes a detailed representation of the middle atmosphere, with a sophisticated suite of gas-phase and heterogeneous chemistry reactions including the O_x, NO_x, HO_x, ClO_x, and BrO_x reaction families (Kinnison et al., 2007). There are ∼100 chemical species and ∼300 chemical reactions. Reaction rates are updated following JPL 2015 recommendations (Burkholder et al., 2015). The model's volcanic sulfur loading is from the Neely and Schmidt (2016) database and has been updated through the Raiakoke eruption in 2019. Polar stratospheric clouds (PSCs) are present below ∼ 200 K as solid nitric acid trihydrate (NAT), water ice, and super-cooled ternary solutions (Solomon et al., 2015). As described further in Section 4.3, to simulate ozone loss more accurately we tested multiple values of the parameterized NAT particle number density controlling denitrification in this model, ranging from the default of 0.01 particles per cm^3 to 10^{-5} particles per cm^3, and chose the smallest value for the final RW and WA simulations.

The Real World runs use the Coupled Model Intercomparison Project phase 6 (CMIP6) hindcast scenario (Meinshausen et al., 2017) based on observations for the

evolution of ODSs and other emissions through 2014. The period 2015 through April 2020 uses the CMIP6 Shared Socioeconomic Pathways (SSP) 585 projection (O'Neill et al., 2016). The WA run assumes a 3.5% per year increase beginning in 1985 in all organic chlorine and bromine species, except for CH_3Cl, CH_2Br_2, and $CHBr_3$, which mainly have natural sources (Figure 4-S1). CH_3Br is assumed to be half from natural sources, half from anthropogenic, so that its increase is half that of the other ODSs.

4.2.2 Satellites

We compare SD-WACCM's total column ozone values to those observed by NASA's Ozone Monitoring Instrument (OMI) on the Earth Observing System (EOS) Aura satellite (Bhartia, 2012). OMI is a nadir-viewing wide-field-imaging spectrometer that continues the global total column ozone record from NASA's Total Ozone Mapping Spectrometer (TOMS). We use the Level 3 gridded data product here for comparison with SD-WACCM's daily column ozone values. Level 3 data is generated from high-quality only Level 2 data and is available on a daily basis. When calculating daily polar cap minimum total ozone values we filter data at solar zenith angles above 82° to remove spurious points.

We compare SD-WACCM's HNO_3 mixing ratios to those observed by NASA's Microwave Limb Sounder (MLS) on the EOS Aura satellite (Waters et al., 2006; Lambert et al., 2007). MLS has been continuously observing the upper atmosphere since its launch in 2004, although data gaps exist, including during the second half of March through early April 2020. MLS data was processed according to the flags and thresholds described in the Version 4.2x Level 2 Data Quality and Description Document. The vertical resolution of the HNO_3 data at the levels of interest is 3-4 km, with a reported measurement precision of $\pm$0.6 ppbv and a systematic uncertainty of $\pm$1.0 ppbv. MLS data was binned into a 5°×5° latitude-longitude grid before plotting.

4.2.3 Ozonesondes

We use balloon-based ozonesondes to examine ozone mixing ratios at individual levels and in vertical profiles. Ozonesondes are launched at regular intervals from multiple stations across the globe and collated by the World Ozone and Ultraviolet Data Centre. We use data from Resolute (74.86°N, -94.98°E), Ny-Ålesund (78.93°N, 11.88°E), Sodankyla (67.34°N, 26.51°E), Eureka (80.04°N, -86.18°E), Alert (82.49°N, -62.42°E), Lerwick (60.13°N, -1.18°E), and Thule (76.53°N, -68.74°E) to represent the historical record of ozone mixing ratios at 50 mb. All data in recent decades are from electrochemical concentration cell (ECC) ozonesondes, which have a precision of 3–5% and an overall uncertainty in ozone concentration of about ±10% up to 30km (Smit et al., 2007; Tarasick et al., 2021). The ozone sensor response time of ∼25s, for a typical balloon ascent rate of 4–5 m/s, gives ozonesondes a vertical resolution of about 100–150 meters. Pre-1980 data from Resolute are from older Brewer-Mast ozonesondes, which have a precision of about 5–10% (Kerr et al., 1994; Smit et al., 1998). For profile comparisons we use ECC ozonesoundings from Eureka Station, along with simultaneously measured temperatures.

4.3 Results

Figure 4-1 shows the total column ozone (TCO) that would have been expected in the World Avoided (top left) on the day of greatest ozone depletion in 2020 in the model, March 13th, compared to that expected and observed in the RW run (top right, bottom right) for the same day. The area meeting the standard definition of an ozone hole in the WA is nearly 20 million km^2, a comparable areal extent to many observed past Antarctic ozone holes, and the region below 150 DU stretches across the North Pole and over significant parts of Canada, Greenland, and Russia. By comparison, while the depletion in the RW case is clearly visible, it never reaches the 220 DU threshold for any significant area. Observations from OMI (lower right) support this, although the higher resolution satellite finds small, isolated patches below 220 DU. The difference between the WA and RW runs (lower left) is 20 DU

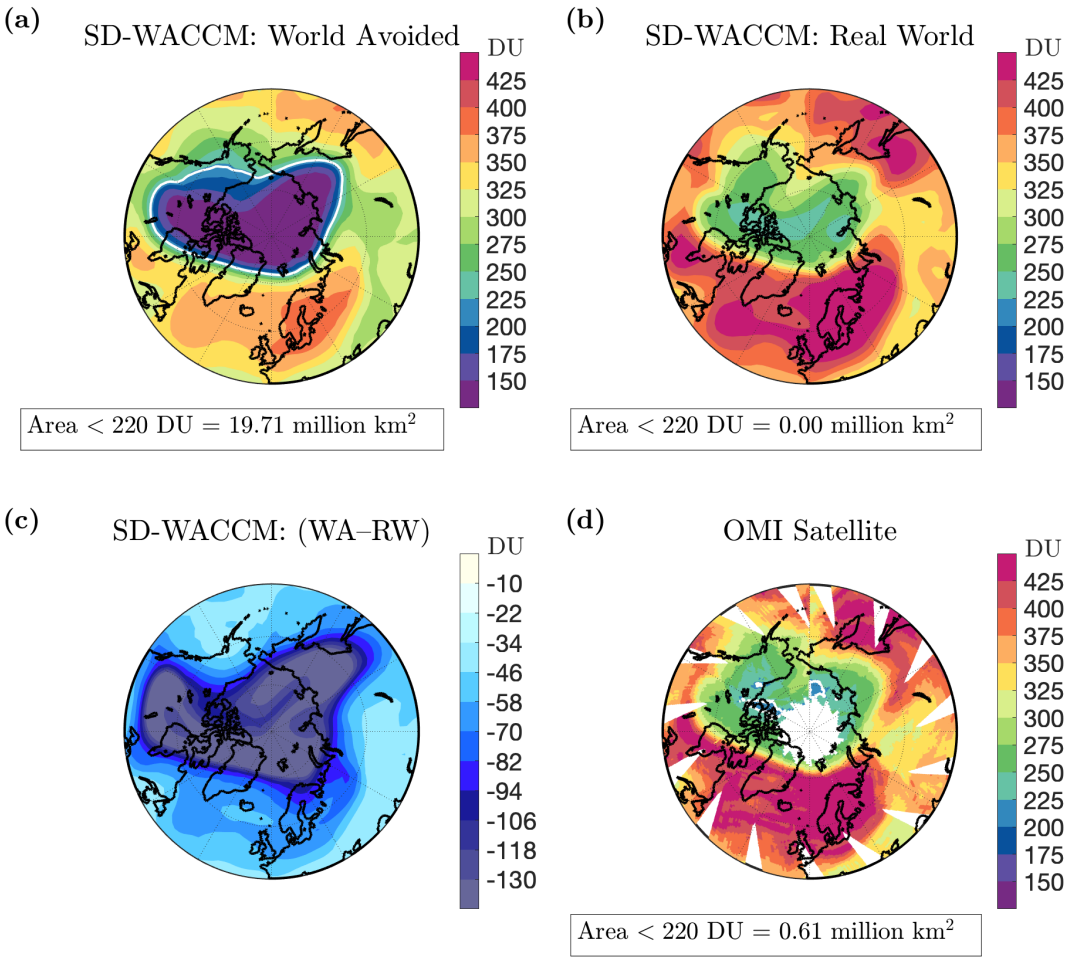

Figure 4-1: Total Column Ozone poleward of 30°N for March 13, 2020. **(a)** shows the World Avoided SD-WACCM run, **(b)** shows the Real World run, **(c)** shows the difference between them, and **(d)** shows the Total Column Ozone Level 3 product from the OMI satellite. All levels are in Dobson Units. Note the different scale on the **(c)** colorbar. The 220 DU contour is outlined in white.

or more throughout the Northern Hemisphere and maximizes at over 130 DU in the Arctic. We can compare this to another recent cold year, 2011 (Figure 4-S2), previously highlighted by others for its large Arctic ozone losses in a WA simulation (Chipperfield et al. 2015, compare our Figure 4-S2 with their Figure 3; we note that our study follows a slightly different WA emissions path, with a different partitioning between anthropogenic and natural emissions for CH_3Br in particular; compare our

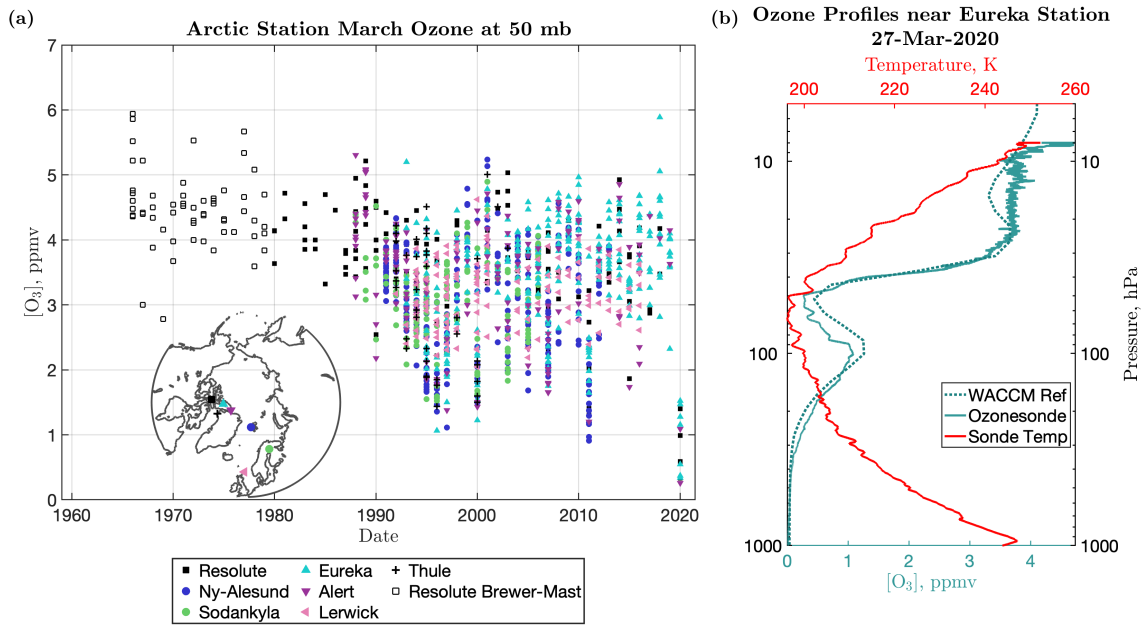

Figure 4-2: **(a)** Daily ozone values centered at 50 mb (±2.5 mb) from ozonesondes launched from various stations across the northern polar region in March. Measurements using less accurate methods are indicated with open symbols. The location of these stations is shown in the lower left corner of the panel. **(b)** Ozone (solid teal) and temperature (solid red) profiles taken at Eureka station on March 27, 2020, compared to the SD-WACCM Real World run's (dotted teal) vertical profile at the nearest model gridpoint.

Figure 4-S1 with their Figure 1a). In our simulations, the expected Arctic ozone hole in 2011 is much smaller in area than in 2020 (11.08 million km^2 vs 19.71 million km^2). The difference is partly due to the increased chlorine loading in the WA nine years later, but we also note that, while 2011 was an extremely cold year, 2020 had lower minimum ozone values that lasted longer than in 2011, with record fractions of the polar vortex being below the PSC temperature formation threshold for a longer period of time (Wohltmann et al., 2020; Inness et al., 2020). In summary, without the Montreal Protocol, 2020's combination of extreme meteorology and increased chlorine loading would have resulted in unprecedented Arctic ozone depletion and an Arctic ozone hole comparable in areal extent to those of the Antarctic, with accompanying large impacts on UV levels throughout the Arctic.

To confirm the historically anomalous nature of 2020 and to evaluate our model's

performance in more detail, we examine a time series of measurements at the 50 mb pressure level from archived Arctic ozonesondes, shown in the left panel of Figure 4-2. Because 2020 displayed very large local changes in Arctic ozone, the less-precise measurements from older Brewer-Mast sondes are also valuable for this purpose and are shown with open symbols. The long ozonesonde record allows us to compare to historical values predating the start of the satellite era in 1979, which is especially important for ozone trends as there may have been some depletion already by that time. Figure 4-2 shows ozone values for available days in March, stacked by year, and demonstrates that 2020 displays ozone amounts lower than any other year in the record at this altitude (including 2011, which displays the next deepest depletion). This is especially apparent in the log-scale version in Figure 4-S3.

The right panel of Figure 4-2 compares the vertical profile of ozone at the nearest SD-WACCM grid point in the RW simulation (dotted teal line) to Eureka station ozonesonde data (solid teal line) for March 27, 2020, showing some of the lowest values of stratospheric ozone ever recorded in the Arctic. Eureka is near the center of the lowest total ozone on this date and is representative of the region based upon the model, and on comparisons with other high-Arctic sites, which show similar profiles. The figure shows that the largest depletion here tracks the lowest local temperatures of the profile (temperature shown in solid red). Although temperature histories can also be important, as activation can persist in air parcels which previously encountered cold air but are currently above the temperature threshold for PSC formation, this broadly supports the view that much of 2020's Arctic ozone loss was related to widespread local cold temperatures increasing the efficiency of heterogeneous reactions on PSCs (Wohltmann et al., 2020; Manney et al., 2020). Figure 4-2 illustrates that the SD-WACCM model successfully captures the observed behavior at this site under these extreme conditions.

We next test how SD-WACCM's nitric acid trihydrate (NAT) number density count relates to calculated denitrification (Fahey et al., 2001) using comparisons to nitric acid observations from the Microwave Limb Sounder (MLS) instrument onboard the AURA satellite (Waters et al., 2006) and ozonesonde profiles. Polar stratospheric

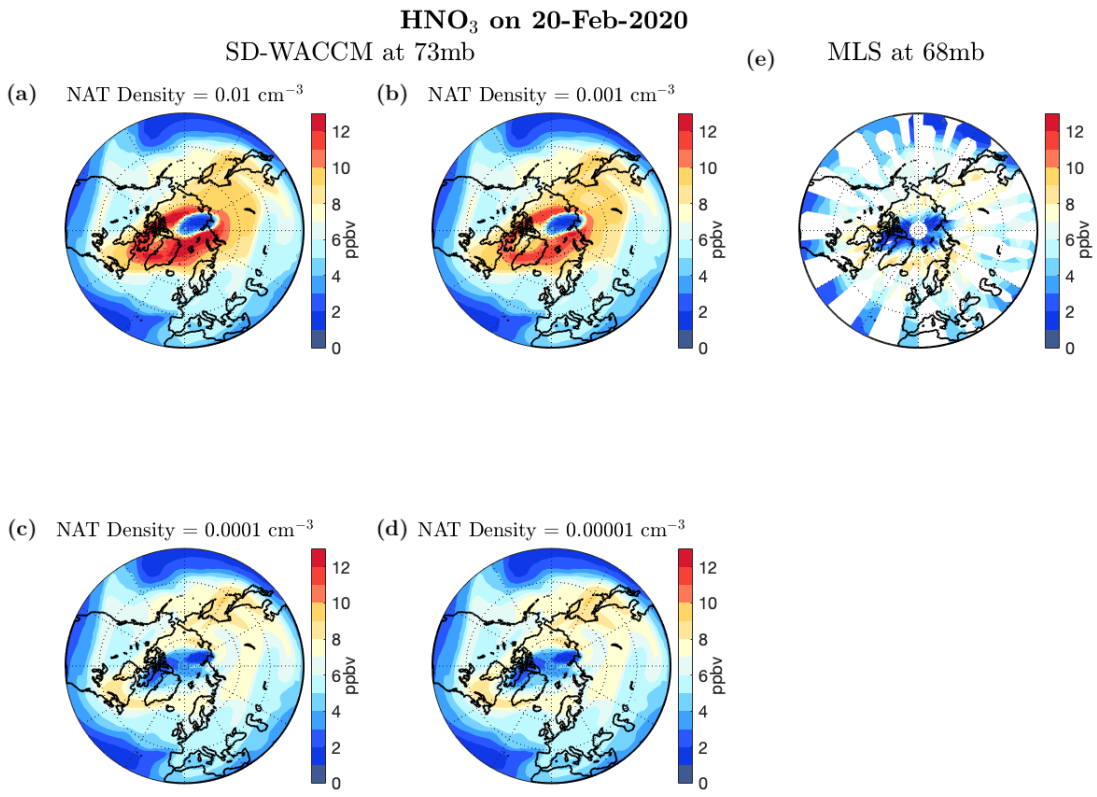

Figure 4-3: HNO_3 in ppbv for February 20, 2020, for different NAT parameterizations in SD-WACCM **(a-d)** compared to MLS **(e)**. In order of increasing denitrification, the NAT density is **(a)** 0.01 cm^{-3}, **(b)** 0.001 cm^{-3}, **(c)** 0.0001 cm^{-3}, and **(d)** 0.00001 cm^{-3}. Panel **(a)** shows the previous standard SD-WACCM parameterization and panel **(d)** shows the chosen parameter value used in the RW and WA simulations. All SD-WACCM figures show the 73 mb level; MLS shows the 68 mb level. Antarctic maps are discussed in Chapter 6.

clouds not only activate chlorine through heterogeneous chemical processing but also denitrify the atmosphere through removal of HNO_3 from the gas phase and subsequent sedimentation. Removing HNO_3 reduces the abundance of NO_2, which in turn enhances active chlorine (i.e., ClO abundances) by reducing $ClONO_2$ formation rates, effecting ozone destruction chemistry. Initial comparisons of ozone profiles to both ozonesonde and MLS data showed that the model's standard approach with a NAT density of 0.01 cm^{-3} (Wegner et al., 2013) was denitrifying too little. As a lower NAT particle density corresponds to larger individual particles, decreasing this parameter

increases denitrification by increasing the settling velocity of the particles. Figure 4-3 shows the progression of four increasingly denitrified RW runs from (a) to (d). Although the coverage of MLS data swaths (e) makes it difficult to distinguish which of the two highest ((c) and (d)) denitrification levels might be a better representation, the two lower denitrification levels (panels (a) and (b)) are much poorer matches to the observations. We ultimately found that a case adopting a NAT particle density of 10^{-5} particles per cm^3 resulted in the closest match to observed ozone profiles throughout a wide vertical range throughout the spring (Figure 4-4a for Eureka on March 27, and Figure 4-S4 for other times at Eureka along with the Alert and Resolute stations) and matched the observed MLS HNO_3 profiles better than other choices (Figure 4-4b), and so chose this value for our RW and WA simulations. As all of our RW runs adopt observed temperatures insofar as they are represented by the MERRA-2 reanalysis, this study illustrates that accurate representation of denitrification (i.e., not only accurate temperature-driven reaction efficiencies but also PSC microphysics impacts) is key for ozone depletion under 2020 Arctic conditions.

In Figure 4-5 we examine the evolution of daily minimum TCO by day of the year from January 2010 to the end of April 2020 for the polar cap north of 70°N, with days in 2020 marked as open circles rather than points. We compare the RW (teal markers) to observations from the OMI satellite (blue markers) and compare both with the WA (orange markers). Dramatic differences are obtained in the calculated and observed 2020 evolution of the daily minimum TCO value over the Arctic polar cap by day of the year for the past decade in Figure 4-5 compared to the preceding years and especially for the World Avoided. Prior to 2020, while the WA case is often lower than the other two, it is often still within the range of TCO values seen in the RW and OMI time series. Furthermore, both the RW run and the OMI observations for 2020 spring display lower values than many WA springs, illustrating the key role of the unusually cold temperatures in addition to chlorine in driving the depletion in 2020. The WA spring of 2020 both displays levels of depletion previously unseen in the data or either simulation early in the spring and stays depleted longer than any other year. Furthermore, its apparent dip compared to the rest of the year

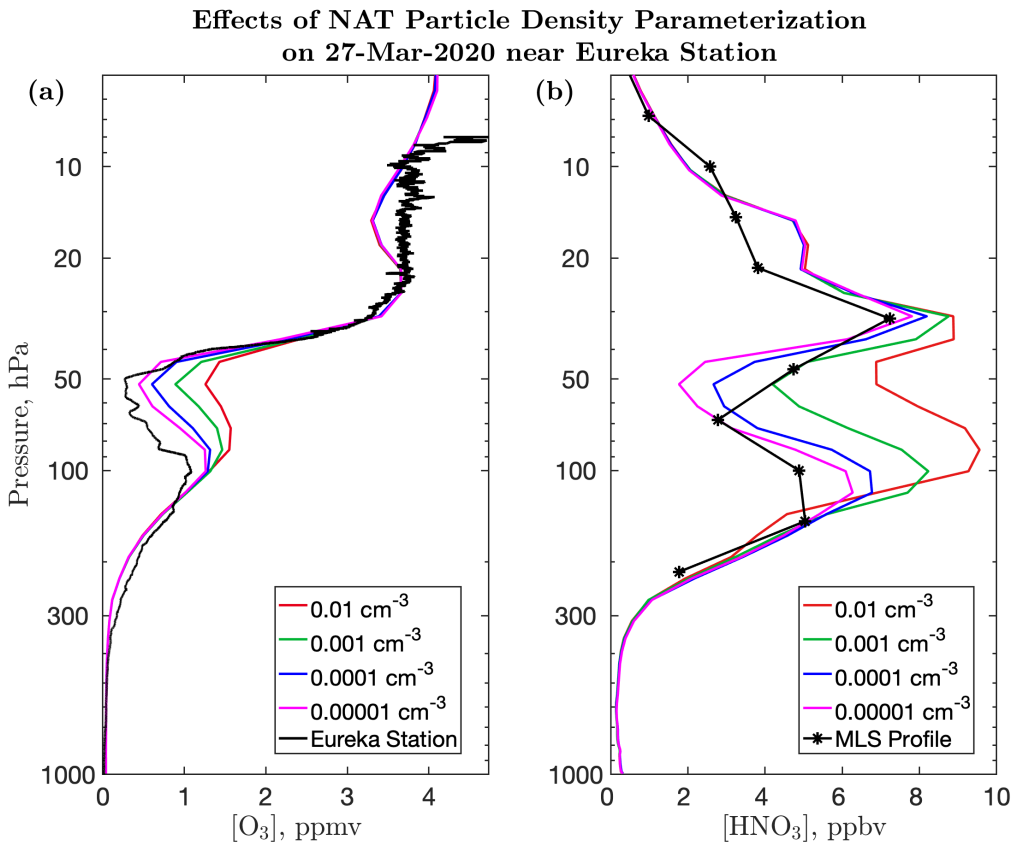

Figure 4-4: Comparison of ozone profiles **(a)** and nitric acid profiles **(b)** for four different SD-WACCM simulations at the gridpoint nearest Eureka Station for March 27, 2020, with ozonesonde data from Eureka Station shown for comparison in **(a)** and the nearest MLS profile on that day shown for comparison in **(b)**. Note that MLS has very few levels in the lower stratosphere, shown by black points. This is the same date as shown in Figure 4-2b, and the magenta ozone profile corresponds to the dotted teal ozone profile shown in that figure.

resembles typical Antarctic ozone evolution (shown in Figure 4-S5) rather than the typical Arctic behavior.

The effects of higher chlorine loading in the WA scenario on vertical ozone profiles are also significant (Figure 4-6, left panel). While both the RW run and ozonesonde data display a limited height region of extremely low ozone, the WA has almost no ozone left throughout the lower stratosphere. This resembles typical Antarctic depletion more than any previous year in the Arctic (Figure 4-6, right panel, with ozonesonde comparison). Depletion in the lower stratosphere reaches these low values

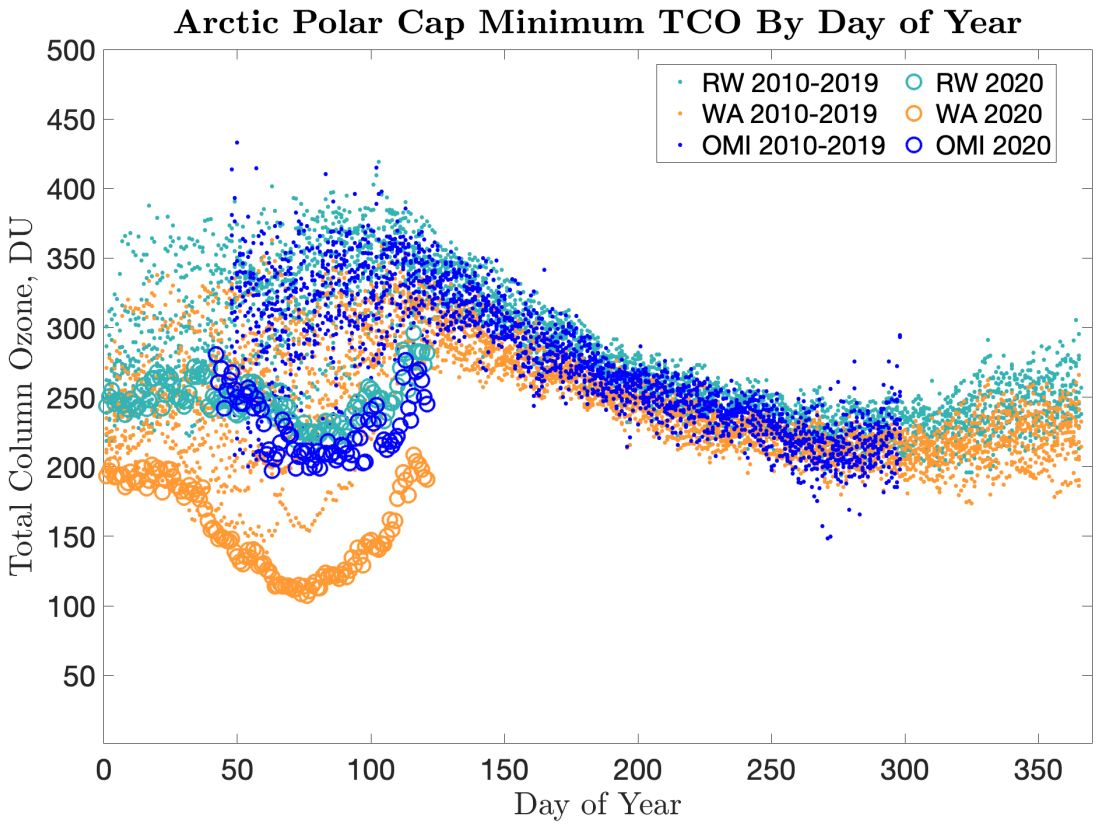

Figure 4-5: Minimum total column ozone simulated by SD-WACCM from 70°N to 90°N from January 2010 through the end of April 2020, plotted by day of the year. Teal markers refer to the reference run and orange markers to the world avoided run. Blue markers refer to observations by the OMI Satellite. Dots indicate days from 2010–2019 and open circles indicate days in 2020.

more quickly in the WA, and persists longer (Figure 4-S6). At higher altitudes, where gas phase depletion identified by Molina and Rowland (1974) is dominant, substantial increases in depletion are also obtained (see below).

A characteristic finding of WA studies is that substantial polar ozone depletion eventually persists year-round (Newman et al., 2009; Garcia et al., 2012). We can see the first indication of such behavior in our WA simulation for 2020 as shown in Figure 4-7, where the RW and WA total ozone time series are shown for the past decade (top panel), along with their difference (bottom panel). While for the first few years of the decade the summertime and autumnal differences between the scenarios remain low and fairly constant, after 2014 a noticeable trend towards increasing column

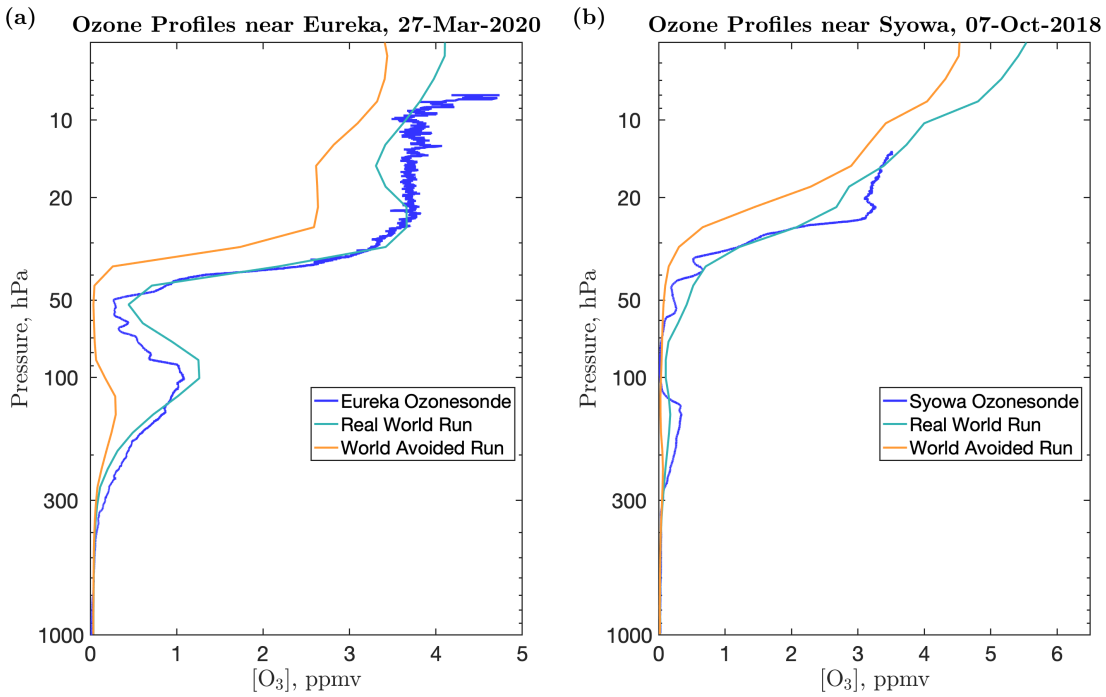

Figure 4-6: Comparison between the Real World (teal) and World Avoided (orange) ozone profiles in SD-WACCM at the gridpoint **(a)** nearest to Eureka station (80.04°N, -86.18°E) for March 27, 2020 and **(b)** nearest to Syowa station in the Antarctic (69.00°S, 39.58°E) for October 7, 2018. Ozonesonde profiles from the stations are shown for comparison in blue.

difference year-round emerges. Much of this summertime difference is due to the gas-phase depletion, as demonstrated by the change in the profiles and increased partial column differences at higher altitudes (Figure 4-S7). It is also noteworthy that while the spring of 2020 is anomalously depleted in the WA as previously shown, the spring ozone values obtained in 2018 and 2019 are also much further from their RW counterparts, demonstrating the growing impact of the Montreal Protocol even for less cold years.

4.4 Discussion and Conclusions

We have demonstrated that, were it not for the Montreal Protocol, in 2020 we should have expected the first Antarctic-like ozone hole to occur over the Arctic, an area with

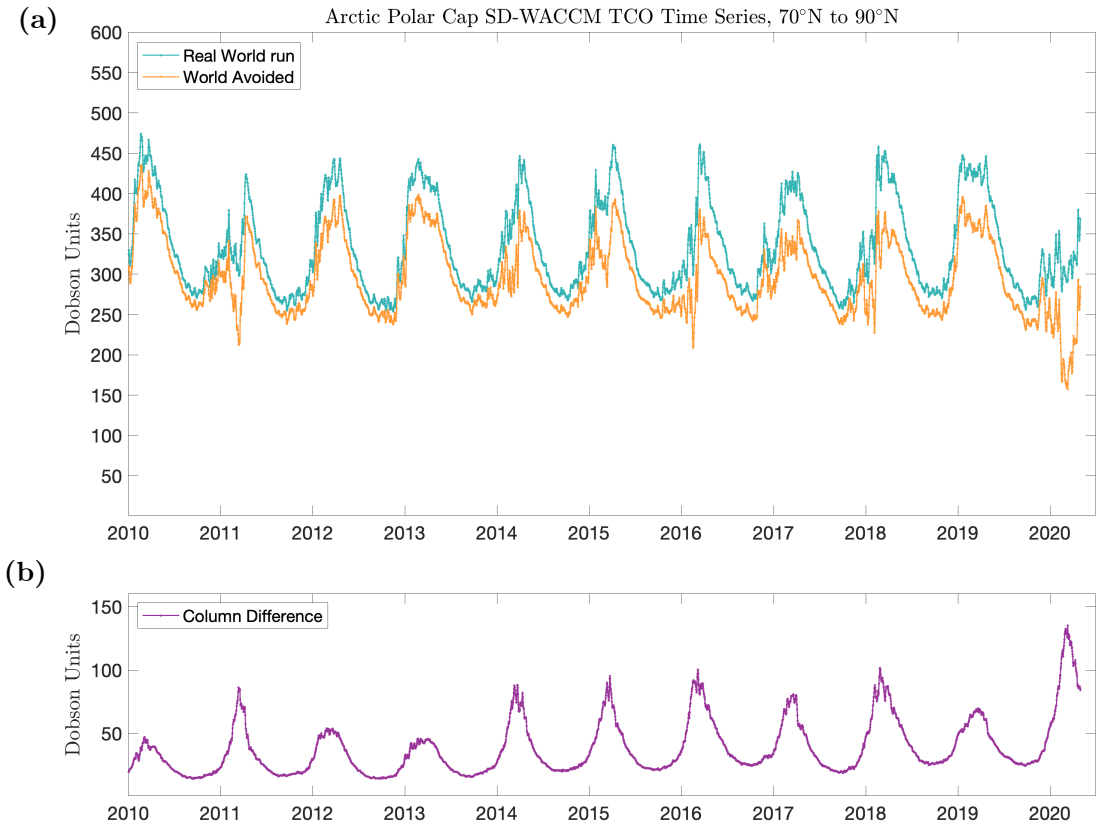

Figure 4-7: **(a)** Time series of mean SD-WACCM total column ozone across the polar cap for the Real World scenario (teal) and World Avoided scenario (orange) from January 2010 through April 2020. **(b)** The difference between the two.

a substantial human population and vibrant ecosystem. The Arctic ozone hole would have begun earlier and persisted longer (see Figure 4-S6) than the headline-grabbing 2020 ozone depletion in the real world did, with ozone all but completely destroyed over a large vertical extent of the lower stratosphere. Furthermore, our simulations support the view that there have already been substantial year-round benefits from the Montreal Protocol for the Arctic. Finally, nitric acid observations and modeling for 2020 help improve our understanding of the role of denitrification in accurately assessing Arctic ozone loss, and further refinements of this will be the subject of future studies.

The main limitation of using a model constrained to real-world meteorology is

Table 4-1: Surface UV Index for the SD-WACCM grid-point nearest to Fairbanks, USA (64.84°N, 147.7°W), Yellowknife, Canada (62.46°N, 114.22°W), Tromsø, Norway (69.66°N, 18.94°E), and Murmansk, Russia (68.96°N, 33.08°E). UV Index is calculated for March 31 and April 30 for both the RW and WA simulations using total column ozone and solar zenith angle at noon under clear-sky conditions in each grid-point.

	RW March 31	WA March 31	RW April 30	WA April 30
Fairbanks	1.15	1.44	2.49	3.06
Yellowknife	1.62	2.52	3.05	3.75
Tromsø	1.12	1.93	2.32	2.75
Murmansk	1.27	2.39	2.19	2.66

that by design it eliminates any feedbacks that changes in ozone would have had on the meteorology. These are worthy of investigation in future free-running model simulations, especially in the context of potential increasing stratospheric Arctic cold extremes from climate change, which have been debated in the literature (Rex et al., 2004). In addition to the increased radiative forcing from increasing ODSs, ozone itself is a potent local greenhouse gas, and ozone depletion of the magnitude simulated here would significantly alter the temperature profile in the stratosphere and perhaps in the troposphere as well. Resultant changes in stratospheric dynamics could potentially have then led to changes in surface climate and sea ice (Smith et al., 2018; Stone et al., 2019; Stone et al., 2020). Surface UV increases could be especially important during the Arctic summer, when the vast majority of biological growth takes place. A coupled biosphere model would be required to fully investigate such effects, but we can estimate the change in surface UV during late March and April 2020 by calculating the clear-sky UV Index at noon for the SD-WACCM grid-point nearest four northern cities using the procedure outlined in Burrows et al., 1994, with the results shown in Table 4-1. While the UV Indices at the end of March in the WA run show substantial percentage increases (from 25% to 88%), the absolute values are still quite small due to the large zenith angles in the Arctic spring. By the end of April, however, there are still substantial differences between the runs, despite active ozone depletion having ceased for the year, reinforcing that there are increasing year-round impacts, as seen in Figure 4-7.

The benefits to society and the earth system achieved by the global community's

adherence to the Montreal Protocol grow with each passing year and can be dramatically documented in cold years with ozone depletion-favoring meteorology – in particular, 2020. As we progress further into the 21st century, studies of the world we avoided will continue to be relevant to both stratospheric science and environmental policy. When the Montreal Protocol was signed, the sophisticated modeling systems used for this and similar studies that can precisely simulate an alternate world did not yet exist. The basic science was, however, sound enough, and the risk clear enough, that society acted nonetheless. Here we have shown that our increased knowledge of what we would have faced has justified this past prudence.

4.5 Supplemental Figures

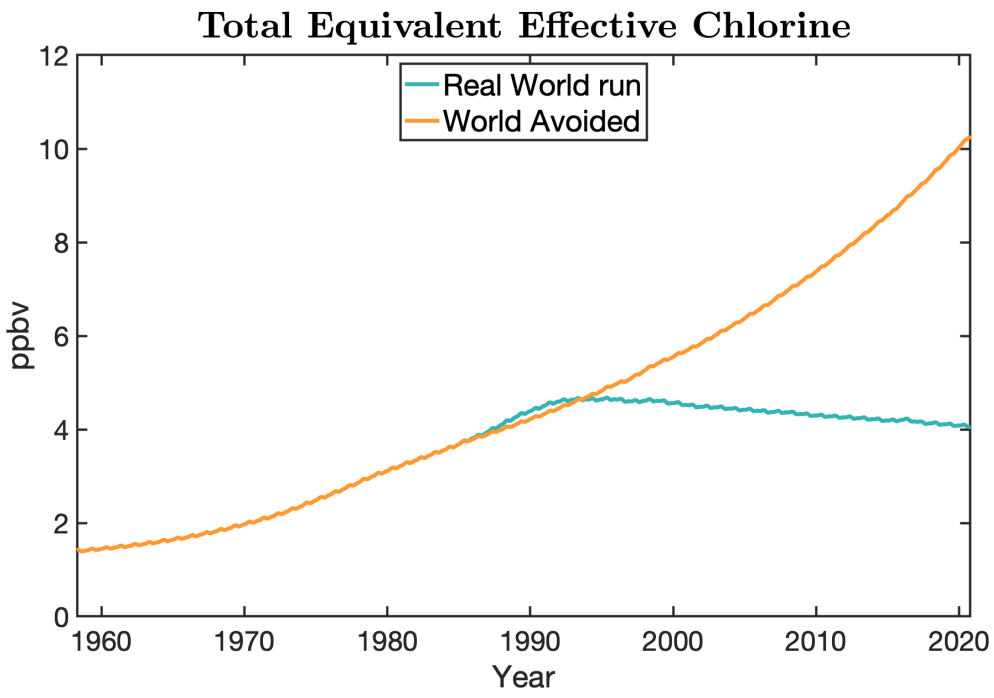

Figure 4-S1: Evolution of stratospheric Total Equivalent Effective Chlorine in ppbv, globally averaged, in the Real World run and the World Avoided, calculated as a linear combination of Cl_y and Br_y, with Br_y given weighting factors of 60 in the midlatitudes and 65 in the polar regions. The two diverge beginning in 1985 as described in Section 4.2.1.

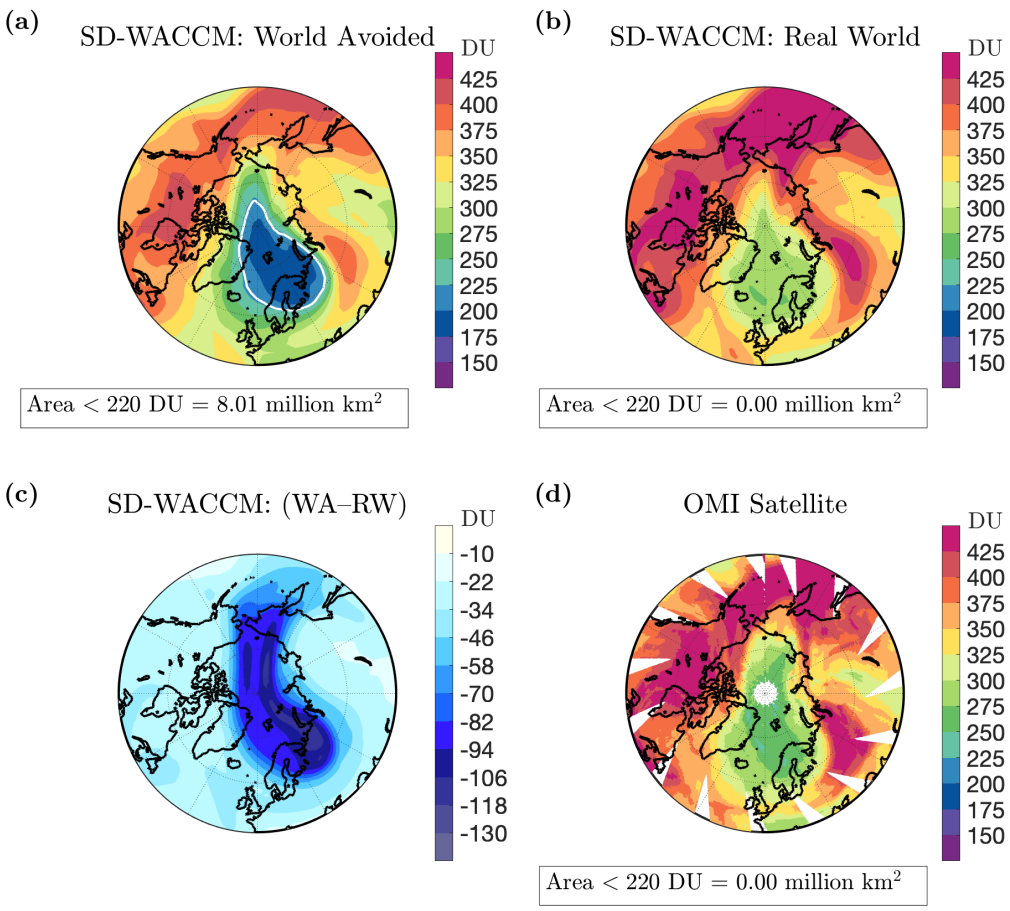

Figure 4-S2: As for Figure 4-1, but for 2011.

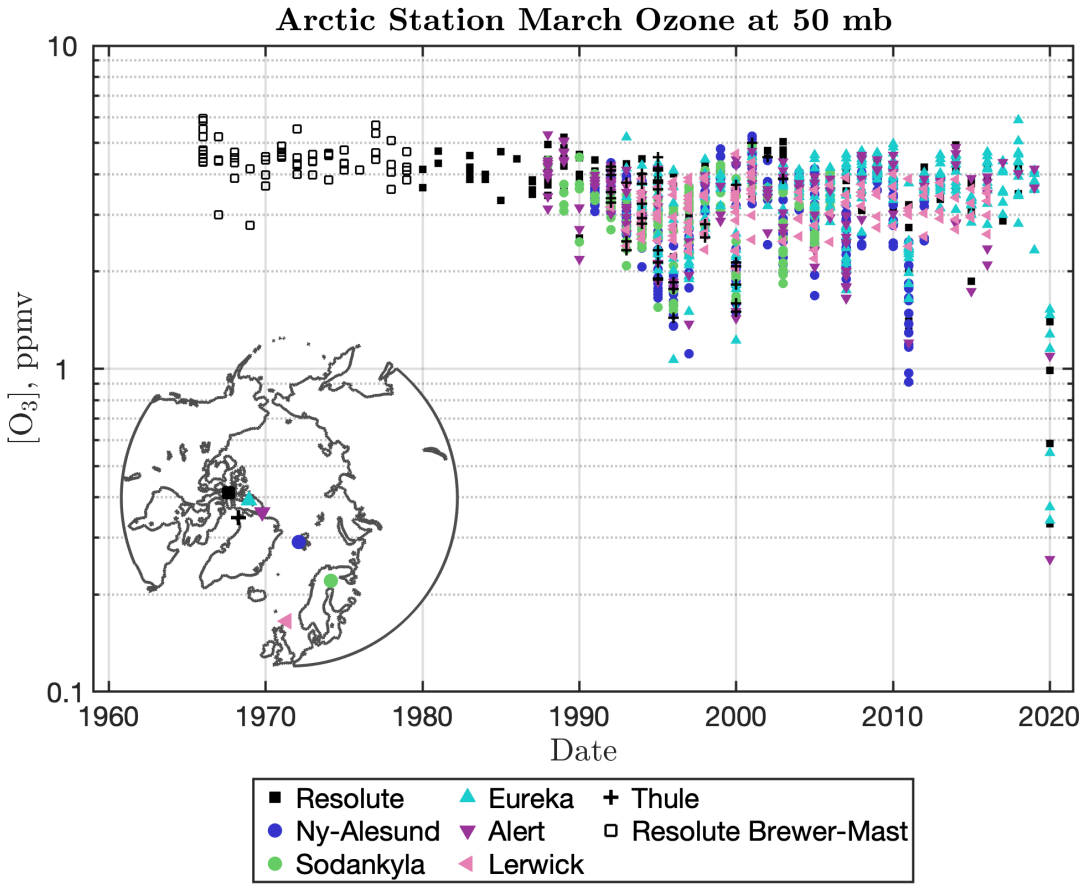

Figure 4-S3: As for the left panel of Figure 4-2, but in log-scale.

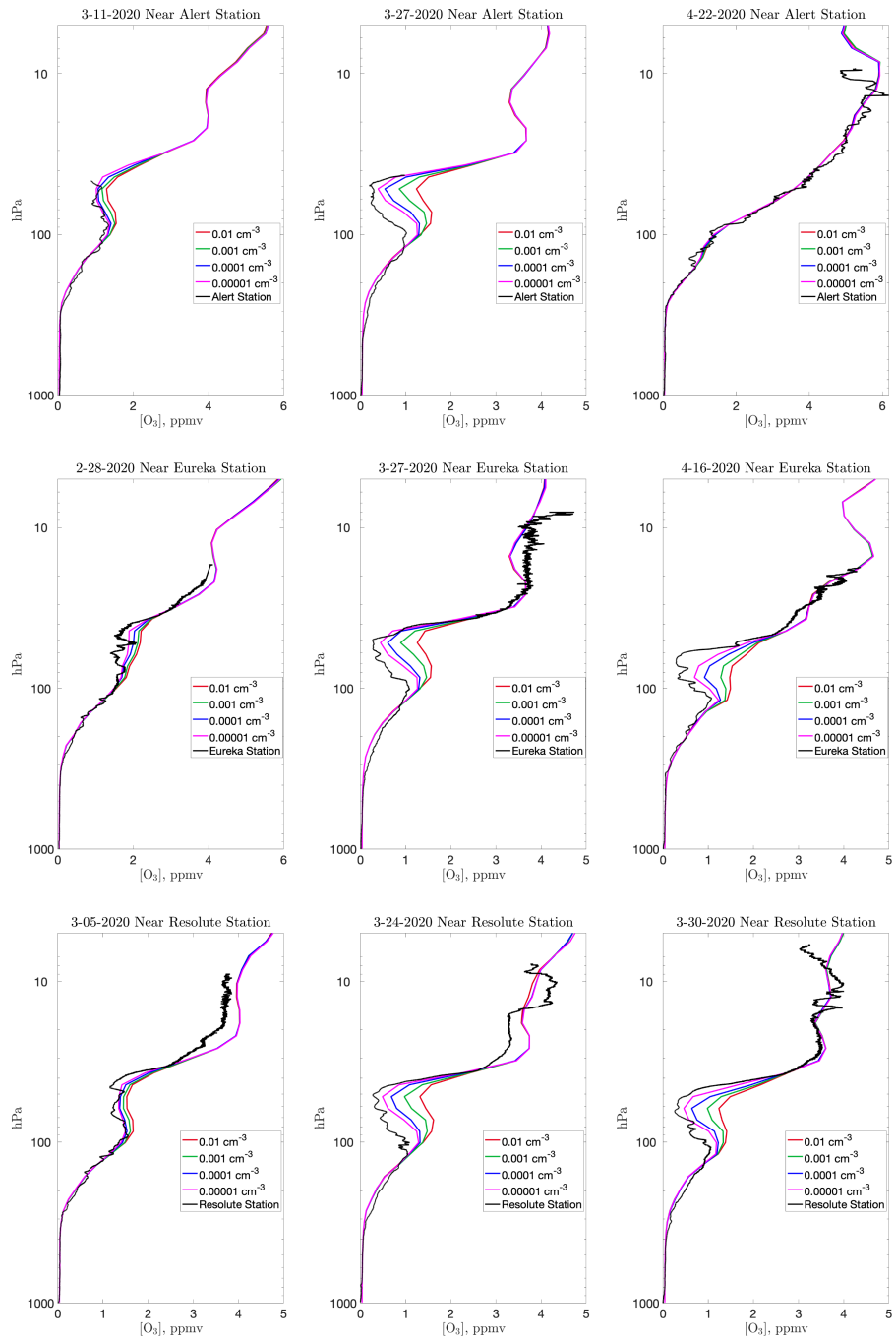

Figure 4-S4: Comparison of ozone profiles for four different SD-WACCM simulations at SD-WACCM gridpoints nearest **(top)** Alert, **(middle)** Eureka, and **(bottom)** Resolute Stations for days in Spring 2020 where ozonesoundings exist and reach at least to the middle stratosphere for a station. Note that the middle panel of the middle row is the same as Figure 4-4a in the main text.

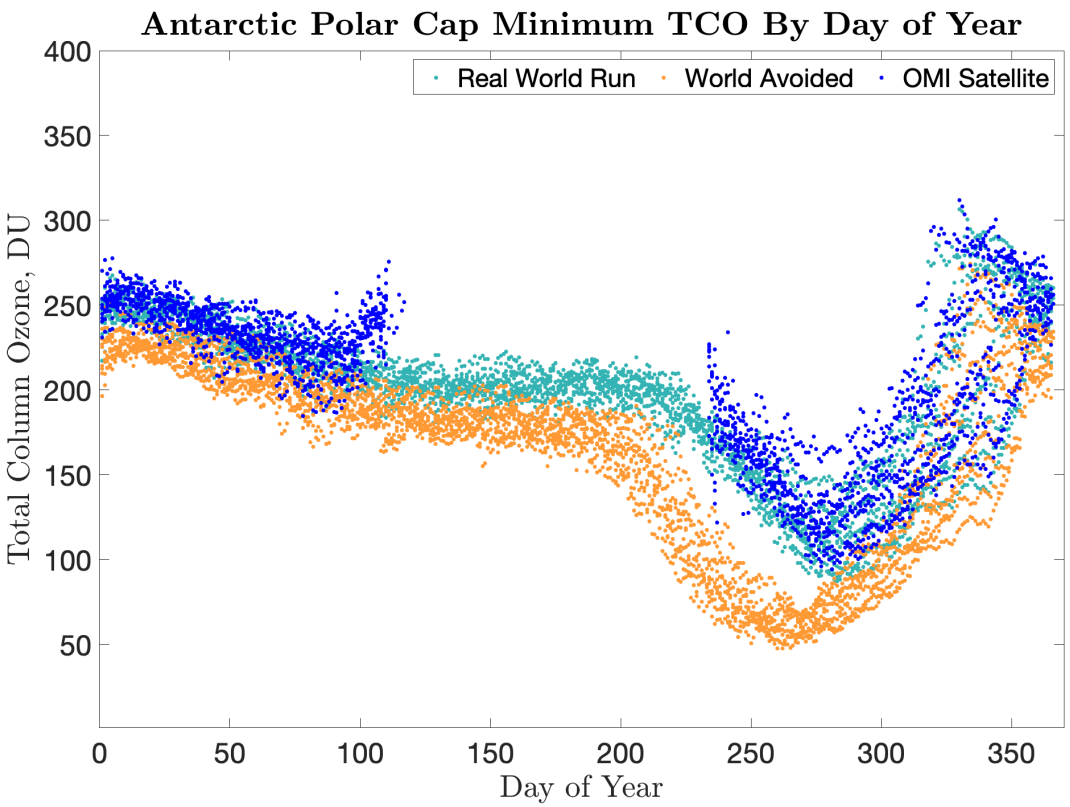

Figure 4-S5: As for Figure 4-5, but for the Antarctic.

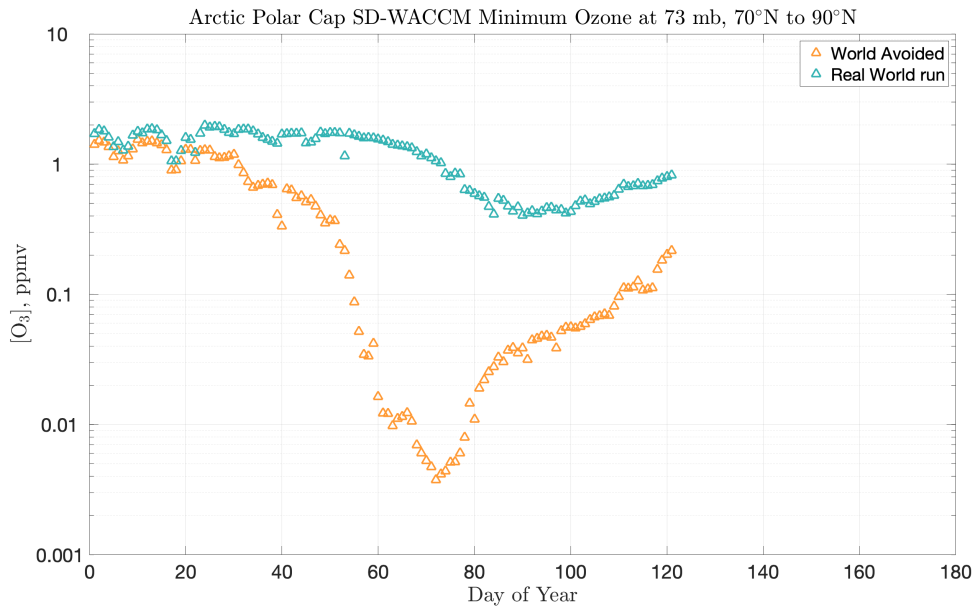

Figure 4-S6: Minimum ozone mixing ratios across the polar cap (70°N–90°N, all longitudes) for each day in 2020 for Real World (teal) and World Avoided (orange) runs in SD-WACCM at 73 mb.

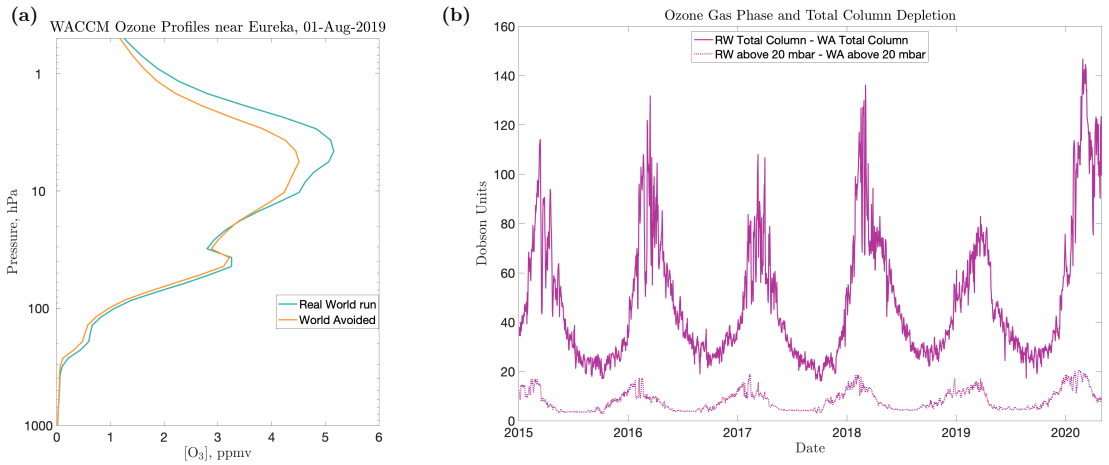

Figure 4-S7: **(a)** Comparison between the Real World (teal) and World Avoided (orange) profiles in SD-WACCM at the model gridpoint nearest to Eureka station for August 1st, 2019. Note the y-axis goes to lower pressures than the profiles in Figures 4-2 and 4-5. **(b)** Comparison between the total column ozone depletion and the partial column ozone depletion at altitudes above 20 mb in the Real World versus World Avoided runs.

THIS PAGE INTENTIONALLY LEFT BLANK

References

[1] Bhartia, P. K.: Data from "OMI/Aura TOMS-Like ozone and radiative cloud fraction L3 1 day 0.25 degree x 0.25 degree V3," (2012). NASA Goddard Space Flight Center, Goddard Earth Sciences Data and Information Services Center (GES DISC), Accessed: October 15th 2020. 10.5067/Aura/OMI/DATA3002

[2] Birmpili, T. (2018). Montreal Protocol at 30: The governance structure, the evolution, and the Kigali Amendment. *Comptes Rendus Geoscience, 350*(7), 425–431. https://doi.org/10.1016/j.crte.2018.09.002

[3] Burkholder, J. B., Sander, S. P., Abbatt, J. P. D., Barker, J. R., Huie, R. E., Kolb, C. E., ... & Wine, P. H. (2015). Chemical kinetics and photochemical data for use in atmospheric studies: Evaluation number 18. Technical Report, Pasadena, CA: Jet Propulsion Laboratory, National Aeronautics and Space Administration. https://trs.jpl.nasa.gov/handle/2014/45510

[4] Burrows, W.R., Vallée, M., Wardle, D.I., Kerr, J.B., Wilson, L.J. and Tarasick, D.W. (1994). The Canadian operational procedure for forecasting total ozone and UV radiation. *Meteorological Applications, 1*(3), 247–265. https://doi.org/10.1002/met.5060010307

[5] Chipperfield, M. P., Bekki, S., Dhomse, S., Harris, N. R., Hassler, B., Hossaini, R., ... & Weber, M. (2017). Detecting recovery of the stratospheric ozone layer. *Nature, 549*(7671), 211–218. https://doi.org/10.1038/nature23681

[6] Chipperfield, M. P., Dhomse, S. S., Feng, W., McKenzie, R. L., Velders, G. J., & Pyle, J. A. (2015). Quantifying the ozone and ultraviolet benefits already achieved by the Montreal Protocol. *Nature Communications, 6*(1), 1–8. https://doi.org/10.1038/ncomms8233

[7] Crutzen, P. J., & Arnold, F. (1986). Nitric acid cloud formation in the cold Antarctic stratosphere: A major cause for the springtime 'ozone hole'. *Nature, 324*(6098), 651–655. https://doi.org/10.1038/324651a0

[8] Danabasoglu, G., Lamarque, J. F., Bacmeister, J., Bailey, D. A., DuVivier, A. K., Edwards, J., ... & Strand, W. G. (2020). The Community Earth System Model version 2 (CESM2). *Journal of Advances in Modeling Earth Systems, 12*(2). https://doi.org/10.1029/2019MS001916

[9] Fahey, D. W., Gao, R. S., Carslaw, K. S., Kettleborough, J., Popp, P. J., Northway, M. J., ... & Von König, M. (2001). The detection of large HNO_3-containing particles in the winter Arctic stratosphere. *Science, 291*(5506), 1026–1031.https://doi.org/10.1126/science.1057265

[10] Farman, J. C., Gardiner, B. G., & Shanklin, J. D. (1985). Large losses of total ozone in Antarctica reveal seasonal ClO_x/NO_x interaction. *Nature, 315*(6016), 207–210. https://doi.org/10.1038/315207a0

[11] Garcia, R. R., Kinnison, D. E., & Marsh, D. R. (2012). "World avoided" simulations with the whole atmosphere community climate model. *Journal of Geophysical Research: Atmospheres, 117*(D23). https://doi.org/10.1029/2012JD018430

[12] Gelaro, R., McCarty, W., Suárez, M. J., Todling, R., Molod, A., Takacs, L., ... & Zhao, B. (2017). The modern-era retrospective analysis for research and applications, version 2 (MERRA-2). *Journal of Climate, 30*(14), 5419–5454. https://doi.org/10.1175/JCLI-D-16-0758.1

[13] Gettelman, A., Mills, M. J., Kinnison, D. E., Garcia, R. R., Smith, A. K., Marsh, D. R., ... & Randel, W. J. (2019). The whole atmosphere community climate model version 6 (WACCM6). *Journal of Geophysical Research: Atmospheres, 124*(23), 12380–12403. https://doi.org/10.1029/2019JD030943

[14] Hofmann, D. J., Oltmans, S. J., Harris, J. M., Johnson, B. J., & Lathrop, J. A. (1997). Ten years of ozonesonde measurements at the south pole: Implications for recovery of springtime Antarctic ozone. *Journal of Geophysical Research: Atmospheres, 102*(D7), 8931–8943. https://doi.org/10.1029/96JD03749

[15] Inness, A., Chabrillat, S., Flemming, J., Huijnen, V., Langenrock, B., Nicolas, J., ... & Razinger, M. (2020). Exceptionally low Arctic stratospheric ozone in spring 2020 as seen in the CAMS reanalysis. *Journal of Geophysical Research: Atmospheres, 125*(23), e2020JD033563. https://doi.org/10.1029/2020JD033563

[16] Kerr, J. B., Fast, H., McElroy, C. T., Oltmans, S. J., Lathrop, J. A., Kyro, E., ... & Tsukagoshi, Y. (1994). The 1991 WMO international ozonesonde intercomparison at Vanscoy, Canada. *Atmosphere-Ocean, 32*(4), 685–716. https://doi.org/10.1080/07055900.1994.9649518

[17] Kinnison, D. E., Brasseur, G. P., Walters, S., Garcia, R. R., Marsh, D. R., Sassi, F., ... & Simmons, A. J. (2007). Sensitivity of chemical tracers to meteorological parameters in the MOZART-3 chemical transport model. *Journal of Geophysical Research: Atmospheres, 112*(D20). https://doi.org/10.1029/2006JD007879

[18] Lambert, A., Read, W. G., Livesey, N. J., Santee, M. L., Manney, G. L., Froidevaux, L., ... & Atlas, E. (2007). Validation of the Aura Microwave Limb Sounder middle atmosphere water vapor and nitrous oxide measurements.

Journal of Geophysical Research: Atmospheres, 112(D24). https://doi.org/10.1029/2007JD008724

[19] Langematz, U. and Tully, M. (lead authors), Calvo, N., Dameris, M., Laat, J. de., Klekociuk, A., ... & Young, P. (2018) Polar Stratospheric Ozone: Past, Present, and Future, Chapter 4 in WMO Scientific Assessment of Ozone Depletion. *UNEP/WMO Scientific Assessment of Ozone Depletion: 2018 (Report)*, 58.

[20] Lickley, M., Solomon, S., Fletcher, S., Velders, G. J., Daniel, J., Rigby, M., ... & Stone, K. (2020). Quantifying contributions of chlorofluorocarbon banks to emissions and impacts on the ozone layer and climate. *Nature Communications, 11*(1), 1–11. https://doi.org/10.1038/s41467-020-15162-7

[21] Manney, G. L., Livesey, N. J., Santee, M. L., Froidevaux, L., Lambert, A., Lawrence, Z. D., ... & Fuller, R. A. (2020). Record-low Arctic stratospheric ozone in 2020: MLS observations of chemical processes and comparisons with previous extreme winters. *Geophysical Research Letters, 47*(16), e2020GL089063. https://doi.org/10.1029/2020GL089063

[22] Meinshausen, M., Vogel, E., Nauels, A., Lorbacher, K., Meinshausen, N., Etheridge, D. M., ... & Weiss, R. (2017). Historical greenhouse gas concentrations for climate modelling (CMIP6). *Geoscientific Model Development, 10*(5), 2057–2116. https://doi.org/10.5194/gmd-10-2057-2017

[23] Mills, M. J., Schmidt, A., Easter, R., Solomon, S., Kinnison, D. E., Ghan, S. J., ... & Gettelman, A. (2016). Global volcanic aerosol properties derived from emissions, 1990–2014, using CESM1 (WACCM). *Journal of Geophysical Research: Atmospheres, 121*(5), 2332–2348. https://doi.org/10.1002/2015JD024290

[24] Molina, M. J., & Rowland, F. S. (1974). Stratospheric sink for chlorofluoromethanes: Chlorine atom-catalysed destruction of ozone. *Nature, 249*(5460), 810–812. https://doi.org/10.1038/249810a0

[25] Montzka, S. A., Dutton, G. S., Yu, P., Ray, E., Portmann, R. W., Daniel, J. S., ... & Elkins, J. W. (2018). An unexpected and persistent increase in global emissions of ozone-depleting CFC-11. *Nature, 557*(7705), 413–417. https://doi.org/10.1038/s41586-018-0106-2

[26] Morgenstern, O., Braesicke, P., Hurwitz, M. M., O'Connor, F. M., Bushell, A. C., Johnson, C. E., & Pyle, J. A. (2008). The world avoided by the Montreal Protocol. *Geophysical Research Letters, 35*(16). https://doi.org/10.1029/2008GL034590

[27] Neely, R. R., and Schmidt, A.: "VolcanEESM: Global volcanic sulphur dioxide (SO2) emissions database from 1850 to present - Version 1.0." (2016). https://doi.org/10.5285/76ebdc0b-0eed-4f70-b89e-55e606bcd568

[28] Newman, P. A., Oman, L. D., Douglass, A. R., Fleming, E. L., Frith, S. M., Hurwitz, M. M., ... & Velders, G. J. M. (2009). What would have happened to the ozone layer if chlorofluorocarbons (CFCs) had not been regulated?. *Atmospheric Chemistry and Physics, 9*(6), 2113–2128. https://doi.org/10.5194/acp-9-2113-2009

[29] O'Neill, B. C., Tebaldi, C., Vuuren, D. P. V., Eyring, V., Friedlingstein, P., Hurtt, G., ... & Sanderson, B. M. (2016). The scenario model intercomparison project (ScenarioMIP) for CMIP6. *Geoscientific Model Development, 9*(9), 3461–3482. https://doi.org/10.5194/gmd-9-3461-2016

[30] Prather, M., Midgley, P., Rowland, F. S., & Stolarski, R. (1996). The ozone layer: The road not taken. *Nature, 381*(6583), 551–554. https://doi.org/10.1038/381551a0

[31] Rex, M., Salawitch, R. J., von der Gathen, P., Harris, N. R. P., Chipperfield, M. P., & Naujokat, B. (2004). Arctic ozone loss and climate change. *Geophysical Research Letters, 31*(4). https://doi.org/10.1029/2003GL018844

[32] Smit, H. G., & Kley, D. (1998, September). JOSIE: The 1996 WMO International intercomparison of ozonesondes under quasi flight conditions in the environmental simulation chamber at Jülich. In *Proceedings of the XVIII Quadrennial Ozone Symposium* (pp. 971–974).

[33] Smit, H. G., Straeter, W., Johnson, B. J., Oltmans, S. J., Davies, J., Tarasick, D. W., ... & Posny, F. (2007). Assessment of the performance of ECC-ozonesondes under quasi-flight conditions in the environmental simulation chamber: Insights from the Juelich Ozone Sonde Intercomparison Experiment (JOSIE). *Journal of Geophysical Research: Atmospheres, 112*(D19). https://doi.org/10.1029/2006JD007308

[34] Smith, K. L., Polvani, L. M., & Tremblay, L. B. (2018). The impact of stratospheric circulation extremes on minimum Arctic sea ice extent. *Journal of Climate, 31*(18), 7169–7183. https://doi.org/10.1175/JCLI-D-17-0495.1

[35] Sofieva, V. F., Kyrölä, E., Laine, M., Tamminen, J., Degenstein, D., Bourassa, A., ... & Bhartia, P. K. (2017). Merged SAGE II, Ozone_cci and OMPS ozone profile dataset and evaluation of ozone trends in the stratosphere. *Atmospheric Chemistry and Physics, 17*(20), 12533–12552. https://doi.org/10.5194/acp-17-12533-2017

[36] Solomon, S., Garcia, R. R., Rowland, F. S., & Wuebbles, D. J. (1986). On the depletion of Antarctic ozone. *Nature, 321*(6072), 755–758. https://doi.org/10.1038/321755a0

[37] Solomon, S., Ivy, D. J., Kinnison, D., Mills, M. J., Neely, R. R., & Schmidt, A. (2016). Emergence of healing in the Antarctic ozone layer. *Science, 353*(6296), 269–274. https://doi.org/10.1126/science.aae0061

[38] Solomon, S., Kinnison, D. E., Bandoro, J., & Garcia, R. R. (2015). Simulation of polar ozone depletion: An update. *Journal of Geophysical Research: Atmospheres, 120*(15), 7958–7974. https://doi.org/10.1002/2015JD023365

[39] Stolarski, R. S., Schoeberl, M. R., Newman, P. A., McPeters, R. D., & Krueger, A. J. (1990). The 1989 Antarctic ozone hole as observed by TOMS. *Geophysical Research Letters, 17*(9), 1267–1270. https://doi.org/10.1029/GL017i009p01267

[40] Stone, K. A., Solomon, S., Kinnison, D. E., Baggett, C. F., & Barnes, E. A. (2019). Prediction of Northern Hemisphere regional surface temperatures using stratospheric ozone information. *Journal of Geophysical Research: Atmospheres, 124*(12), 5922–5933. https://doi.org/10.1029/2018JD029626

[41] Stone, K. A., Solomon, S., & Kinnison, D. E. (2020). Prediction of Northern Hemisphere regional sea ice extent and snow depth using stratospheric ozone information. *Journal of Geophysical Research: Atmospheres, 125*(22), e2019JD031770. https://doi.org/10.1029/2019JD031770

[42] Strahan, S. E., & Douglass, A. R. (2018). Decline in Antarctic ozone depletion and lower stratospheric chlorine determined from Aura Microwave Limb Sounder observations. *Geophysical Research Letters, 45*(1), 382–390. https://doi.org/10.1002/2017GL074830

[43] Tarasick, D. W., Smit, H. G., Thompson, A. M., Morris, G. A., Witte, J. C., Davies, J., ... & Vömel, H. (2021). Improving ECC ozonesonde data quality: Assessment of current methods and outstanding issues. *Earth and Space Science, 8*, e2019EA000914. https://doi.org/10.1029/2019EA000914

[44] Toon, O. B., Hamill, P., Turco, R. P., & Pinto, J. (1986). Condensation of HNO_3 and HCl in the winter polar stratospheres. *Geophysical Research Letters, 13*(12), 1284–1287.https://doi.org/10.1029/GL013i012p01284

[45] Waters, J. W., Froidevaux, L., Harwood, R. S., Jarnot, R. F., Pickett, H. M., Read, W. G., ... & Walch, M. J. (2006). The earth observing system microwave limb sounder (EOS MLS) on the Aura satellite. *IEEE Transactions on Geoscience and Remote Sensing, 44*(5), 1075–1092. https://doi.org/10.1109/TGRS.2006.873771

[46] Wegner, T., Kinnison, D. E., Garcia, R. R., & Solomon, S. (2013). Simulation of polar stratospheric clouds in the specified dynamics version of the whole atmosphere community climate model. *Journal of Geophysical Research: Atmospheres, 118*(10), 4991–5002. https://doi.org/10.1002/jgrd.50415

[47] Wohltmann, I., von der Gathen, P., Lehmann, R., Maturilli, M., Deckelmann, H., Manney, G. L., ... & Rex, M. (2020). Near-complete local reduction of Arctic stratospheric ozone by severe chemical loss in spring 2020. *Geophysical Research Letters, 47*(20), e2020GL089547.https://doi.org/10.1029/2020GL089547

[48] World Meteorological Organization (WMO), Scientific Assessment of Ozone Depletion 2018. Global ozone research and monitoring project. *Report No. 58*, Geneva, Switzerland, (2018).

Chapter 5

Accounting for the Effects of Gravity Waves on Chemistry in the WACCM Model

Abstract

In this chapter I present results from the first set of simulations coupling SD-WACCM6's orographic gravity wave parameterization to the chemistry module so that the latter takes into account temperature perturbations (T') produced by the passage of sub-grid scale orographic gravity waves rather than responding to the mean background temperature alone. Such effects are especially important for microphysical processes and chemical reactions that vary nonlinearly with temperature, such as PSC formation and evaporation, heterogeneous chlorine activation, and thermal decomposition of the tropospheric pollutant PAN. To account for this, orographic gravity wave T' are sub-cycled through the chemistry module every three minutes, or ten times per chemistry time-step, for 2010–2011. I compare our results to a reference run without this connection and quantify the magnitude of the effects on several important chemical species near known orographic hotspots. Finally, I conduct preliminary investigations into verifying our results with satellite data for both ClO and T'. I discuss future steps in improving model computational efficiency and conducting more in-depth observational comparisons at the end of each associated section.

5.1 Background

As shown in Figure 1-2 of this thesis, the heterogeneous chemistry reactions which control the rate of chlorine activation, and the resulting ozone depletion, have an extremely nonlinear increase with decreasing temperature. Therefore, for example, a chlorine-containing air parcel which spends half its time at 190 K and half its time at 200 K will experience more activation than an air parcel which resides at a steady 195 K for the same amount of time. This effect is especially important at average temperatures slightly above the threshold for rapid activation, as any excursions to colder temperatures will cause a large increase in total activation. Temperature perturbations can have an additional nonlinear effect in the polar regions where PSCs form. PSC particles that rapidly crystalize at temperatures below their formation threshold do not evaporate immediately when brought back above that temperature threshold. Instead, they will continue to provide surfaces for heterogeneous reactions for a finite time at higher ambient temperatures than PSCs are normally expected to occur.

The combined impact of these two effects has been known in the polar regions for several decades. In 1994, Murphy and Ravishankara compared chlorine reaction rates along trajectories of air parcels near the sharp temperature gradient at the edge of the Antarctic polar vortex. They found that reaction rates calculated using mean temperatures of these trajectories completely missed a high "tail" of activation caused by the coldest temperatures the air parcels encountered. Reactions 1.1–1.3 were consistently underestimated, in the most extreme cases by factors of several hundred. In 1998, Carslaw et al. investigated this phenomenon in the Arctic, and concluded that accounting for the negative temperature perturbations from orographic gravity waves could help explain the underestimation of Arctic ozone depletion seen in models at the time.

GCMs' spatial resolution has increased along with computing power, but the vertical resolution of most models remains of order a few kilometers in much of the stratosphere and the horizontal resolution of order one degree, requiring the

parameterization of small scale dynamics and their resulting temperature fluctuations. Gravity waves in particular are a current focus of model improvement, as they are a major source of fine scale structure in the atmosphere and also an important component of the physics behind multiple atmospheric processes, but both their sources and propagation require sub-grid scale parameterizations (Scinocca & McFarlane, 2000; Richter, Sassi, & Garcia, 2010; Zou et al., 2021; Fritts and Alexander, 2003). Gravity waves are generated by various sources, including flow over orography, convection, and frontal systems. They vertically transport horizontal momentum high into the atmosphere until they reach critical levels or become unstable enough to turbulently break, depositing their energy and momentum into the mean flow (Fritts and Alexander, 2003, and references therein). Accurately simulating this momentum deposition is key to correctly representing the circulation in the stratosphere and mesosphere, including the Brewer-Dobson Circulation and the Quasi-Biennial Oscillation.

While there has been a concerted effort to improve gravity wave parameterizations in models to better represent these dynamics, and while these changes are known to modify the chemical composition through changing transport and circulation-induced temperature shifts (Garcia et al., 2017; Richter, Sassi, & Garcia, 2010), less attention has been paid to the direct impact on chemistry from temperature perturbations described above, with only a few GCMs explicitly accounting for them. Orr et al. (2015) successfully included the temperature fluctuations from an updated gravity wave parameterization in the UK Met Office Unified Model, and found that it enhanced regional PSCs by up to 50% in July over the Antarctic Peninsula. Weimer et al., (2020) used a nested grid configuration around the Antarctic Peninsula in the global chemistry model ICON-ART, and found that it also improved the comparison between the model and the observations. Our current study seeks to couple the gravity wave parameterization in the WACCM model to the chemistry world-wide in a chemically accurate and computationally efficient manner. A novel aspect of this current study is that we consider not only the impact on PSC microphysics in the polar regions but also the direct temperature effect on chemistry rates in the tropics and midlatitudes.

5.2 Model Implementation

This study uses the SD-WACCM6 model with an updated NAT parameterization, both of which were described previously in Chapter 4.2. The gravity wave parameterization, which we are directly connecting to the chemistry for the first time, is described in more detail here.

WACCM uses the McFarlane (1987) orographic source, the Beres et al. (2005) convective source, and the Richter, Sassi, & Garcia (2010) frontal source gravity wave parameterizations. For this study, we consider only the effects of the orographic gravity wave parameterization on chemistry, although we will extend this to include the other sources in later work. The McFarlane parameterization was recently modified as described in Garcia et al. (2017) to address the Southern Hemisphere "cold pole bias" which was causing too much ozone depletion in the Antarctic spring. It is important to recognize that improving gravity wave parameterizations is an active area of research, and we intend our chemical coupling to remain robust to improvements in these parameterization in the future.

The MERRA-2 reanalysis fields that nudge SD-WACCM's winds and temperature have a time-step of 6 hours and only pass information about the mean temperature in a grid box to the chemistry module, which itself has a time-step of 30 minutes. The gravity wave parameterization contains more detailed information, but prior to this study had no linkage to the chemistry module beyond its effects on the mean temperature and winds; thus the chemistry module had no information on the range of temperatures that air parcels in a grid box might experience within a time-step. There are multiple ways to remedy this and account for the effects of gravity waves on temperature. We are focusing on methods in which the temperature perturbation can be expressed as a sine wave perturbation (T') to the mean temperature as a function of quantities output by the gravity wave source parameterization. The relatively straightforward link between T' and vertical displacement for the orographic gravity wave parameterization, summarized below, is a major reason that the orographic gravity wave parameterization is the first one we are linking to the chemistry. Future

coupling of the chemistry to the frontal and convective source parameterizations will need different formulations.

To derive T' we begin with the linearized, thermodynamic equation for orographic gravity waves with a phase speed of zero with no diabatic heating:

$$\bar{U}\frac{\partial T'}{\partial x} = -w'\left(\frac{d\bar{T}}{dz} + \frac{\kappa\bar{T}}{H}\right)$$

where H is the scale height, κ is the ratio of specific heats, and $\bar{U}$ and $\bar{T}$ are the model grid-cell wind normal to the orography and background temperature.

We then extract the vertical displacement amplitude of the gravity wave due to the orographic perturbation, $h'(z)$, from the gravity wave parameterization and relate it to the vertical velocity:

$$w' = \bar{U}\frac{\partial h'}{\partial x}$$

Combining the above and assuming that all gravity wave quantities have x-dependence of the form e^{ikx}, we arrive at:

$$T' = -h'\left(\frac{d\bar{T}}{dz} + \frac{\kappa\bar{T}}{H}\right)$$

We finish by modeling the temperature perturbation as a sine wave modulating the background mean temperature:

$$T = \bar{T} + |T'|\sin\left(\frac{2\pi n}{N}\right) \quad n = 1, 2, ..., N$$

This form allows us to input the combined background and gravity wave perturbation temperature to the chemistry module as a single value, and allows us to easily increase or decrease the frequency of the chemistry cycling by increasing or decreasing the total number of steps, N, within the full chemistry time-step. Large values of N will increase computational time; as discussed further below, the optimal sample rate will be determined by testing.

An underlying assumption of this linkage is that the chemistry model time-step

of 30 minutes is long enough to sample all phases of the wave. We can estimate the accuracy of this assumption by calculating the intrinsic period of several typical orographic gravity waves:

$$\tau = \frac{L_x}{U}$$

Such waves generally have scales of tens to a few hundreds of kilometers and phase speeds near zero (Bacmeister, 1993; Fritts & Alexander, 2003). Using background wind speeds of 10 m/s and 25 m/s we find periods of:

$$\frac{100 \text{ km}}{10 \text{ m/s}} = 166.7 \text{ min} \qquad \frac{100 \text{ km}}{25 \text{ m/s}} = 66.67 \text{ min}$$

$$\frac{25 \text{ km}}{10 \text{ m/s}} = 41.67 \text{ min} \qquad \frac{25 \text{ km}}{10 \text{ m/s}} = 16.67 \text{ min}$$

Our assumption that all phases of the wave are sampled within a chemistry time-step should therefore be valid for most orographic gravity waves under consideration, but may fail for small wavelengths in very strong winds. We will revisit this assumption once our initial results are fully analyzed to quantify what level of bias this may introduce.

Three approaches to sampling the orographic gravity wave temperature perturbation distribution are listed below, representing time-step-based sampling, statistical-based sampling, and random sampling:

1. Sample the temperature perturbation at a 3-minute time-step and sub-cycle the chemistry 10 times.

2. Pass the mean, maximum, and minimum of the temperature perturbation each cycle to the chemistry.

3. Stochastically sample the temperature distribution a certain number of times.

The two key metrics by which we judge the coupling scheme are accuracy in accounting for orographic gravity wave effects and computational efficiency of implementation. We have therefore begun with Method 1, as it is the most reliably

accurate, and have run simulations for 2010–2011 for both a reference case (REF) and the new configuration (GW). Once we have characterized the expected effects on the chemistry, we will revisit the other methods to see if any of them provide a faster method of coupling without unacceptably degrading the increased chemical accuracy. A modified version of one of these methods may also be the optimal choice (for example, sampling at a 5-minute time-step or passing the quartiles of the temperature perturbation to the chemistry).

5.3 Changes to Heterogeneous Chemistry

We begin our analysis by examining the impact of this new parameterization connection on heterogeneous chlorine activation from Reactions 1.1–1.3. We focus on several distinct regions around the globe that are known to be orographic hotspots of gravity wave activity, such as the Andes, Rockies, and Antarctic Peninsula, or were important to previous analyses, in the case of the EASM region. The EASM region is referred to as the Tibetan Plateau region here in order to emphasize the orographic nature of the current gravity wave effects. In Figure 5-1, the latitude–longitude boxes used to define the Andes, the Tibetan Plateau, the Rockies, and the Antarctic Peninsula regions are plotted with |T'| daily mean model output. Individual days and levels for each box were chosen to give a sense of typical |T'| perturbations during months with significant gravity wave activity. Note that there are many gridpoints without any activity at all; these zero values are omitted from subsequent analysis of T' magnitude unless otherwise indicated.

In Figure 5-2, the percentage change in ClO, one of the most direct indicators of chlorine activation, is shown for the zonal mean for (left) September 2011 for the southern polar regions and (right) for July 2011 for the tropics and subtropics. Red colors correspond to an increase in ClO, and thus likely activation, with the new GW configuration. Note that while there are very large changes near the equator in the righthand plot, concentration levels are quite small here and so even a small change in activation may register a big signal. However, we know there is already activation

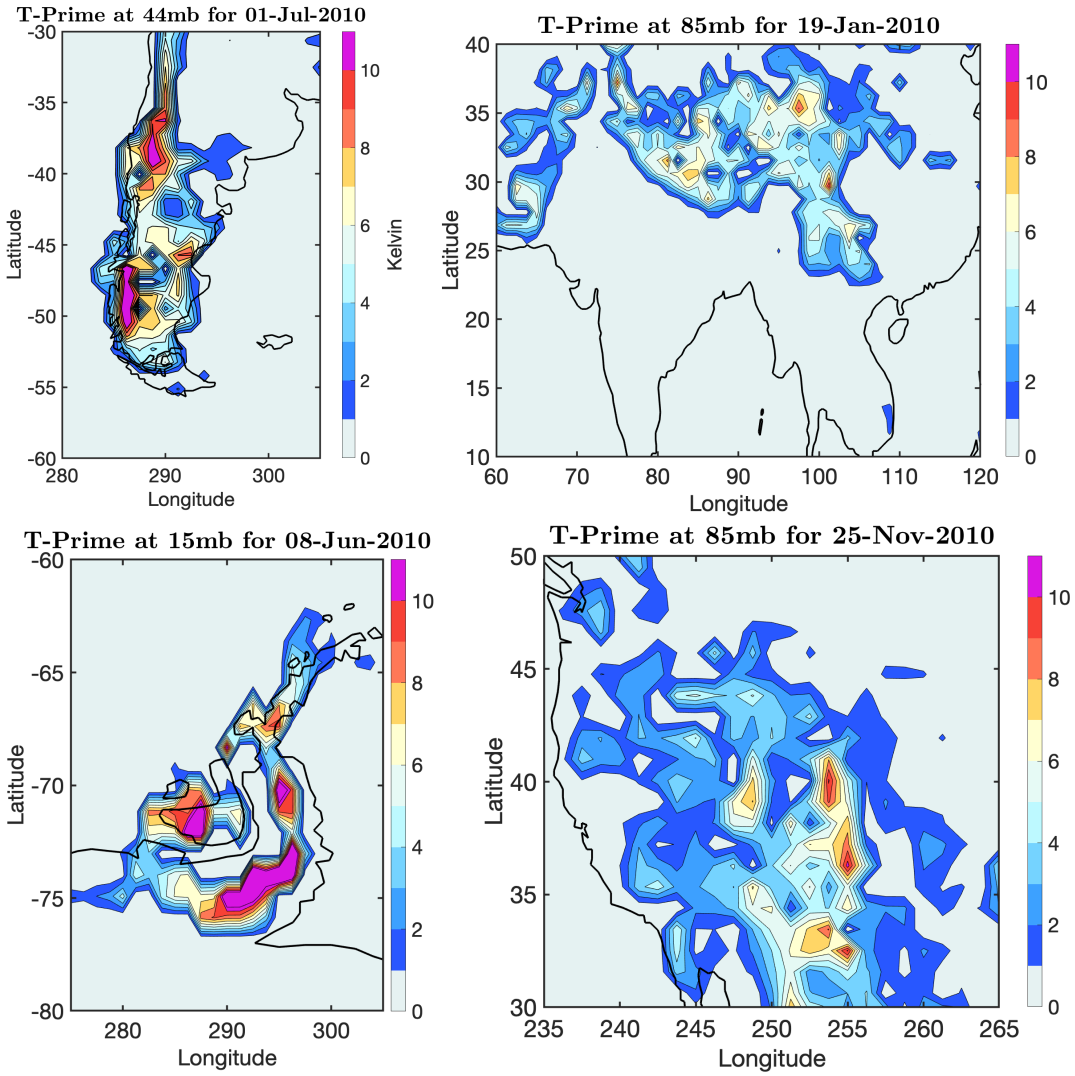

Figure 5-1: Geographic regions used to analyze chemistry and T-primes. Clockwise from upper left they are referred to as the Andes, the Tibetan Plateau, the Rockies, and the Antarctic Peninsula. T-prime contours are the absolute values from orographic gravity wave activity for a single day and pressure level.

in July 2011 due to the effect of the EASM as explained in Chapter 1, so this is a promising region for further investigation. The Antarctic region shows little change in the lower stratosphere where most of the ozone depletion occurs. This may be due to the fact that ozone is already so low that further depletion is difficult, so that this new linkage expands the vertical range of chlorine activation but has little effect as lower saturated levels. Alternately, the temperatures in this region may be cold enough that gravity wave perturbations matter little and activation occurs rapidly

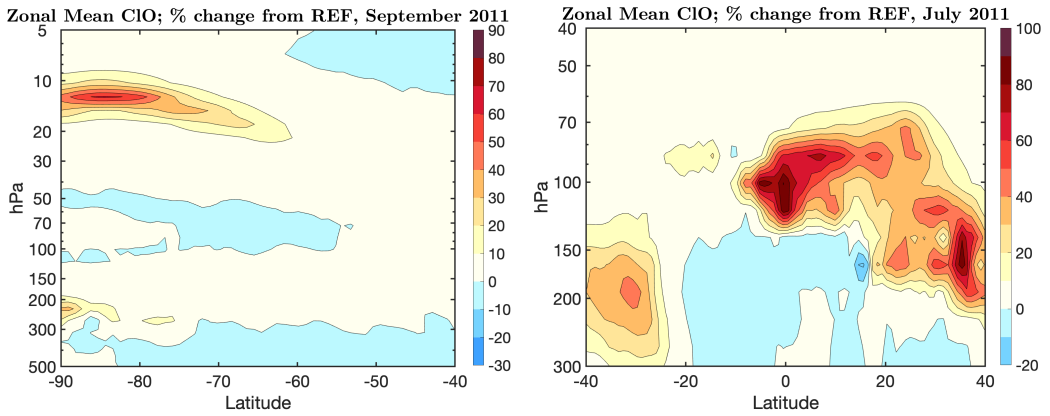

Figure 5-2: Zonal mean percentage change in ClO from the reference run to the new configuration for **(left)** southern polar regions for September 2011 and **(right)** tropical and subtropical regions for July 2011. Note the difference in vertical scale. Red colors are positive and thus correspond to cases where ClO was higher in the GW run.

regardless. The major changes here are in the mid-to-upper stratosphere, which may be partly due to changes in the rates of gas-phase reactions as well as heterogeneous ones.

To investigate these signs of chlorine activation changes further, we examine daily-resolution time series for multiple fields of interest, as well as the background temperatures ($\overline{T}$) and T' magnitudes. We begin by looking at 15 mb over the Antarctic Peninsula, which based on Figures 5-1 and 5-2 we expect to be a likely area of increased activation. Figure 5-3 shows time series of fields of interest for a single grid-cell in this region. The top left panel shows |T'|, and we can see that there are indeed regular temperature swings of up to 12 K. The first few of these in August correspond to slightly decreased reaction rates for the $ClONO_2$ + H_2O reaction (second panel down on the left) and the $ClONO_2$ + HCl reaction (second panel down on the right), which may be a result of this reaction saturating at the lowest temperatures, or possibly due to quicker early depletion of the reactants HCl and $ClONO_2$. It should also be noted that these are only the reactions on sulfate aerosols; examination of reactions on water ice (not shown) indicated very little additional activation, most likely because the altitude is too high for PSCs.

HCl and $ClONO_2$ decrease in the GW run and ClO increases, as we would expect

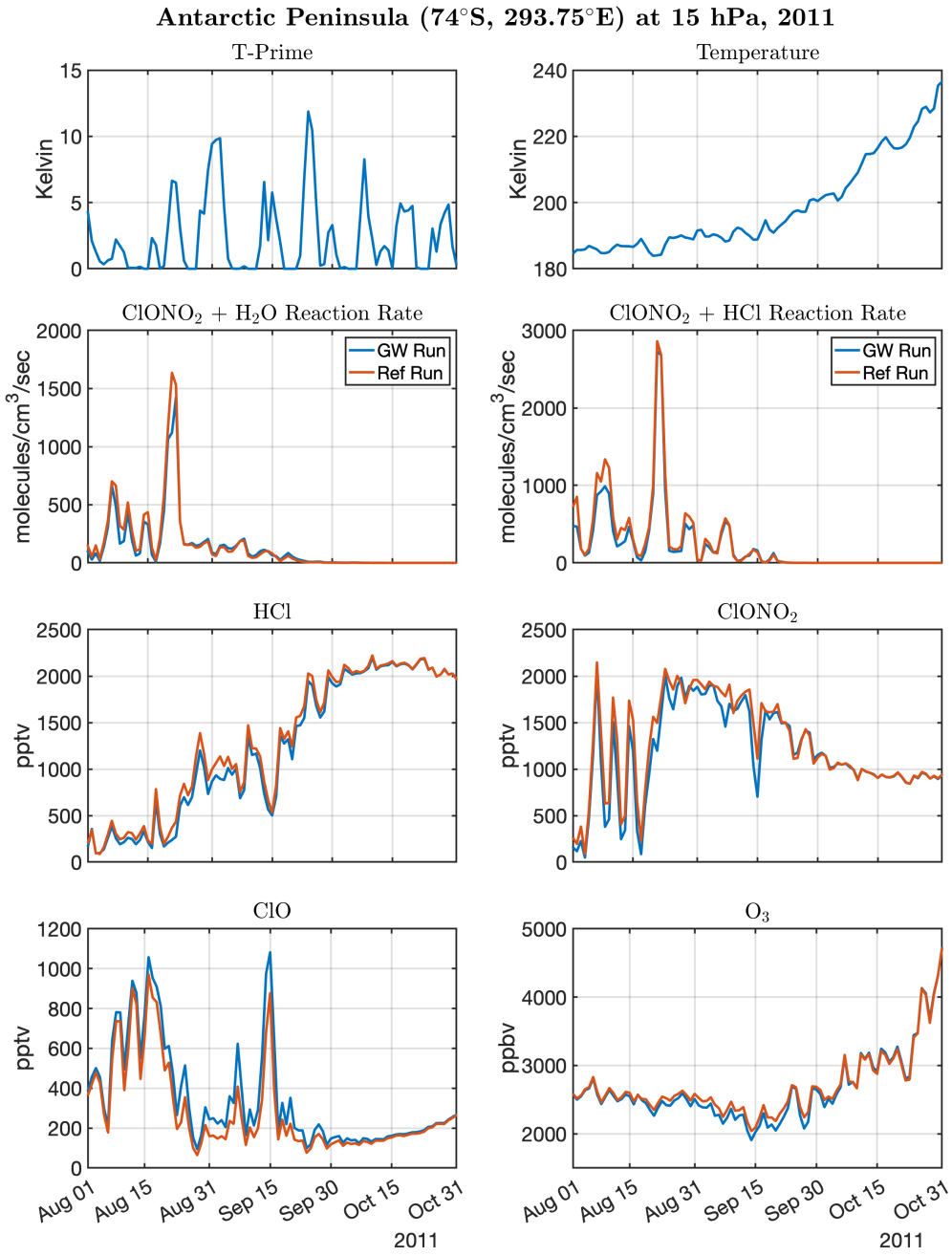

Figure 5-3: Time Series of |T'|, $\overline{T}$, the $ClONO_2$ + H_2O reaction rate, the $ClONO_2$ + HCl reaction rate, [HCl], [$ClONO_2$], [ClO], and [O_3] in a single grid-cell over the Antarctic Peninsula at 15 mb. Blue lines show the GW run and orange lines show the REF run. The time range is from August 1, 2011 to October 31, 2011.

to see as a signature of activation. Ozone decreases more in the GW run for the second half of August and September, which may impact the rate at which the ozone

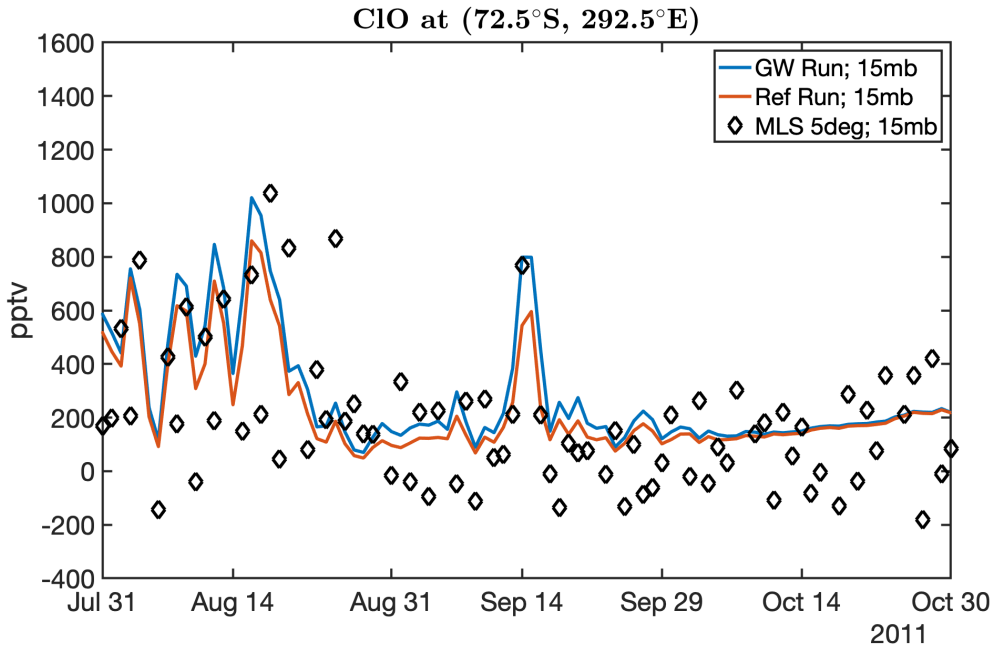

Figure 5-4: Time series of [ClO] over the Antarctic Peninsula at 15 mb for the GW (blue) and REF (orange) runs at the same grid-cell shown in Figure 5-3 and for MLS data (black diamonds). The MLS data have been binned by 5°latitude × longitude and the coordinates in the title refer to the center of the MLS grid-cell, not the SD-WACCM grid-cell.

hole forms. By October, however, the two runs are nearly identical despite continued gravity wave activity. Comparing the absolute temperature plot to the |T'| plot and ClO plots reveals the reason for this. While GW activity persists until the end of October, the mean temperature begins rising mid-September, and soon reaches a point where even temperature swings of order 10 K are no longer large enough to result in very efficient activation. In general, when the ambient temperature is below ∼200 K, the effect of gravity wave temperature fluctuations is to trigger intermittent but strong activation.

The magnitude of the ClO changes between the GW and REF runs is large enough to potentially be distinguishable by satellite observations. We examine ClO data from NASA's Microwave Limb Sounder (MLS) onboard the EOS AURA satellite (Waters et al., 2006). The ClO MLS data was processed according to the flags and thresholds described in the Version 5.0x Level 2 and 3 Data Quality and Description Document, and binned into a 5°×5° latitude-longitude grid before plotting. The data resolution

in the stratosphere is $\sim 3-4.5$ km, with a reported measurement precision of ± 0.1 ppbv and a systematic uncertainty of $\pm 0.02-0.03$ ppbv for the 15 hPa pressure level. As the ClO mixing ratios are reported to have significant biases for pressures at 68 hPa and lower down, we restrict our analysis to the higher levels.

Figure 5-4 compares the same time series of ClO shown in Figure 5-3 to the closest MLS grid-point at 15 hPa. We see that the MLS ClO levels in general match SD-WACCM6's quite well, with enhancement during August and briefly in mid-September and lower levels the rest of the year. Visually the highest MLS observations are a better match to the GW run than the REF run, and the peaks near August 20th and September 15th are within the reported measurement uncertainty and precision listed above for the GW run only. However, this is only one time series, and while several other individual grid-points were also examined and showed similar results, a more thorough investigation of MLS's variability in this region is required to quantify the true uncertainty in this season before the results can be considered statistically significant. Nevertheless, this is a promising sign that adding in activation from gravity wave temperature perturbations has improved the model's performance under certain conditions in the Antarctic Peninsula region.

We next examine the activation seen in the right panel of Figure 5-2 in the subtropics. Figure 5-5 shows the same time series as Figure 5-3 but for a single grid-cell in the Tibetan Plateau region at 85 mb. The time series now span the boreal summer months, when the EASM is most active and when we found activation in WACCM4 previously (Solomon el al., 2016), although we note that the future inclusion of convective gravity wave effects may be more important here than the orographic impacts, as the latter are largest in boreal winter. Ambient concentrations of chlorine species are much lower than in the Antarctic, and the reaction rates are very intermittent. Although there are several clear activation events in late June and early July, they do not appear to correspond to the gravity wave activity in this grid cell. It is possible that there is short-range transport from nearby grid-cells, or from other levels, and examination of adjacent grid-cells (not shown) confirms that the reaction rates themselves vary significantly from location to location. However,

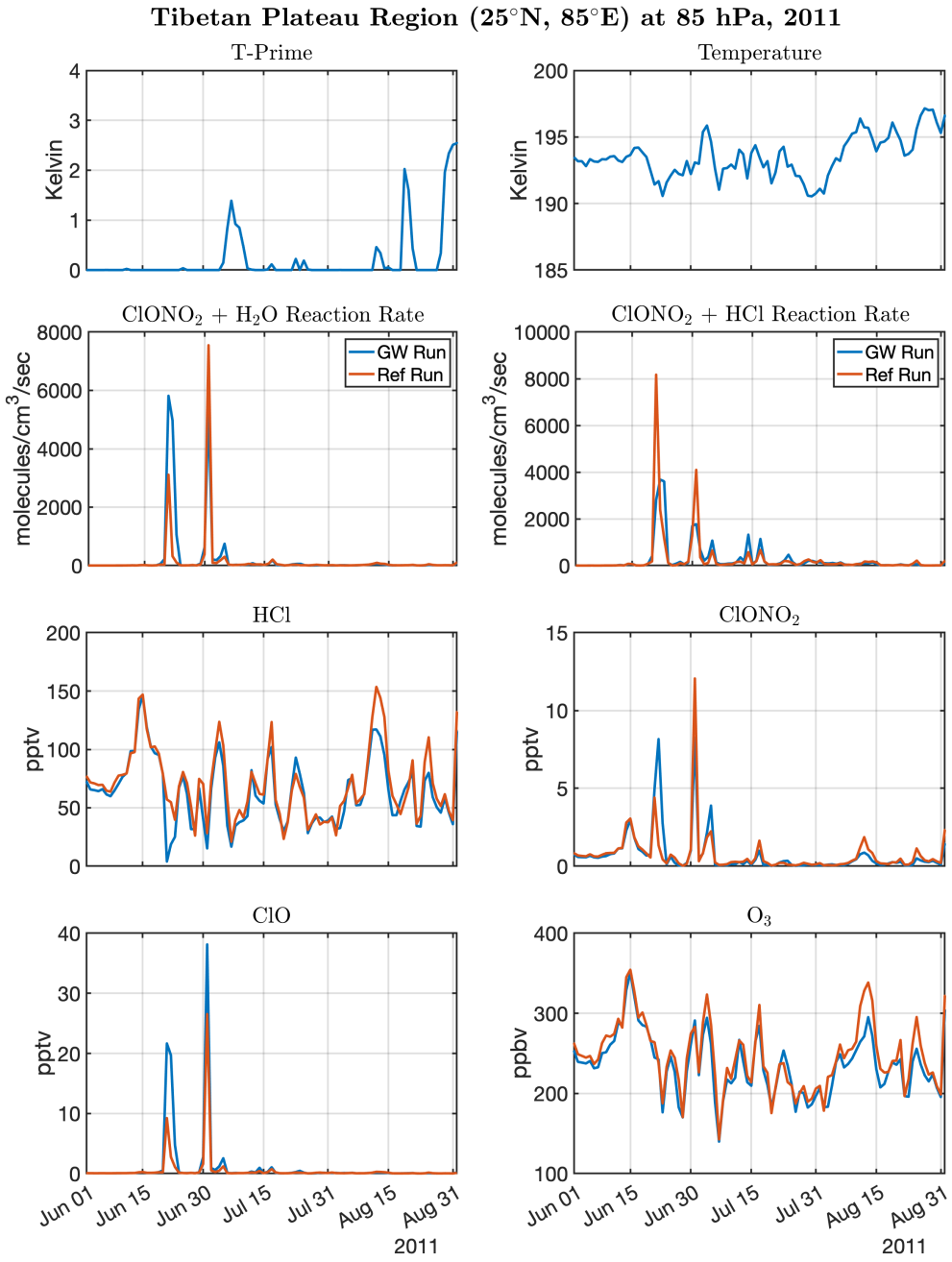

Figure 5-5: As for Figure 5-3 but for a grid-cell in the Tibetan Plateau region at 85 mb from June 1, 2011 to August 31, 2011.

the reaction rate spikes near June 20th do correspond to a clear decrease in HCl and increase in ClO. There does not appear to be much of a signal in ozone itself – while there are differences between the GW and REF runs in ozone, they do not correspond to ClO activation but may be due to the random firing of convection that will always

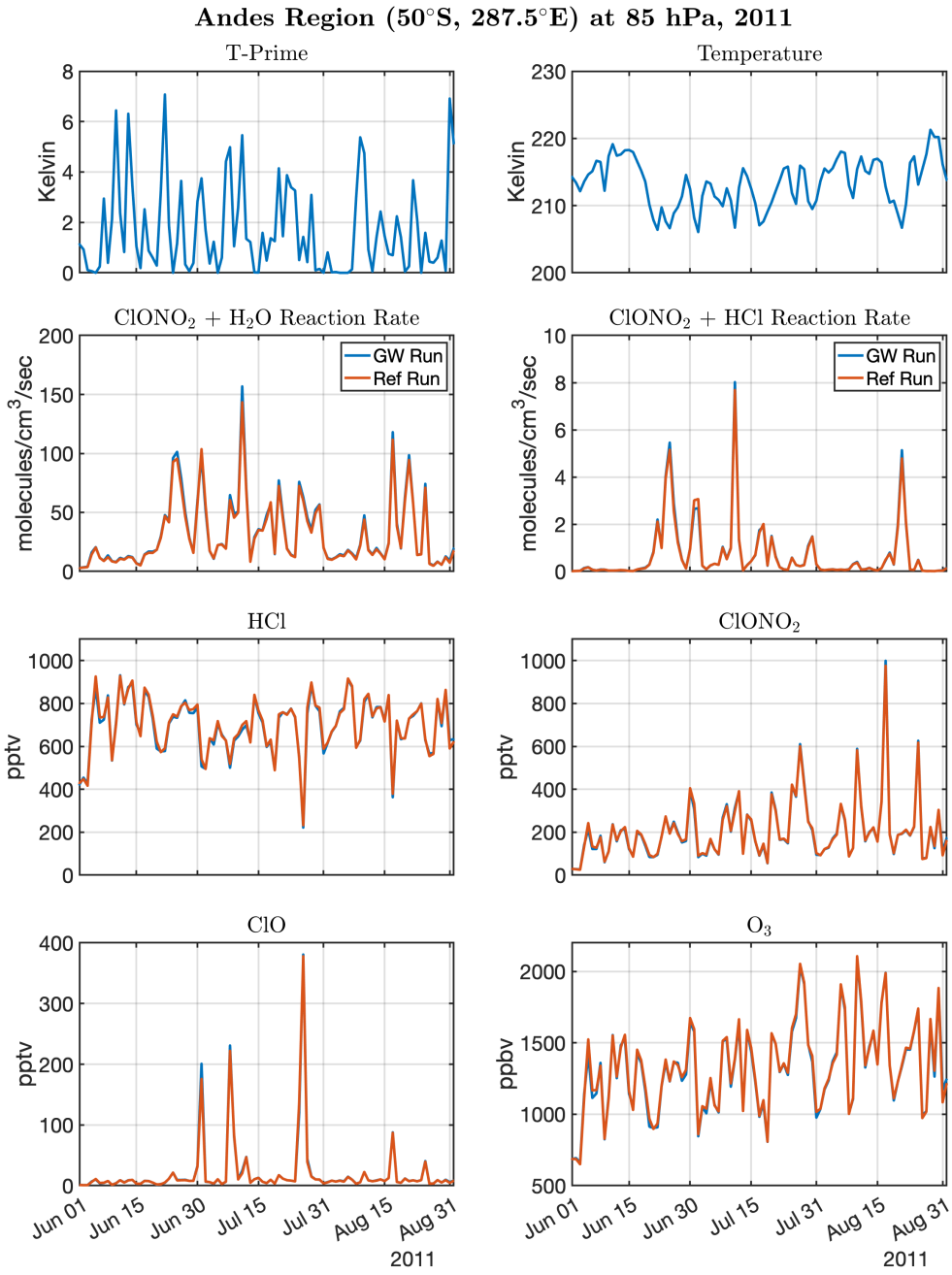

Figure 5-6: As for Figure 5-3 but for a grid-cell in the Andes region at 85 mb from June 1, 2011 to August 31, 2011.

differ slightly between any two WACCM runs. The impact of convection is explored further in the next section.

Finally, we look at the same plot for a point in the Andes region. Despite frequent and robust gravity wave activity, there is little change in the chemistry

between the GW and REF runs. The ambient temperature once again provides the solution: at 210–215 K, even the largest T' amplitudes of ∼7 K cannot decrease the temperature enough for significant change in the activation, unlike in the Tibetan Plateau region, which hovers between 190–195 K, the region where Reactions 1.1–1.3 are most sensitive to temperature perturbations.

5.4 Changes to Other Chemistry

While we have focused so far on the heterogeneous reactions associated with chlorine activation and therefore anthropogenic ozone depletion, gravity wave temperature perturbations will impact any chemical species with reaction rates that are strongly nonlinear with chemistry. One example of another species of interest is peroxyacetyl nitrate (PAN; chemical formula $CH_3C(O)OONO_2$). PAN is a volatile organic compound (VOC) and its lifetime of several weeks in the upper troposphere makes it a vector for the transport of NO_x pollution to remote regions, and also an important tracer of such (Moore & Remedios, 2010; Wiegele et al., 2012). The dominant loss process of PAN in the lower and middle troposphere is thermal decomposition, but this is extremely temperature-dependent and once in the upper troposphere loss via photolysis dominates (Talukdar et al., 1995). Given this dependency, gravity wave temperature perturbations have the potential to modify the transport of this important pollutant in significant ways, as faster thermal decomposition will result in less PAN reaching the upper troposphere and slower thermal decomposition will result in the opposite.

The left panel of Figure 5-7 shows theoretical calculations of PAN's lifetime against thermal decomposition as a function of altitude for the US 1976 Standard Atmosphere (blue line), compared with the lifetime against photolysis (taken from Talukdar et al., 1995; see their Figure 6). The red dashed lines show hypothetical temperature perturbations of ±10 K from the Standard Atmosphere, and the black line shows the mean loss rate of these perturbations. It can be clearly seen that the imposition of symmetric temperature perturbations of this magnitude shifts the altitude at which

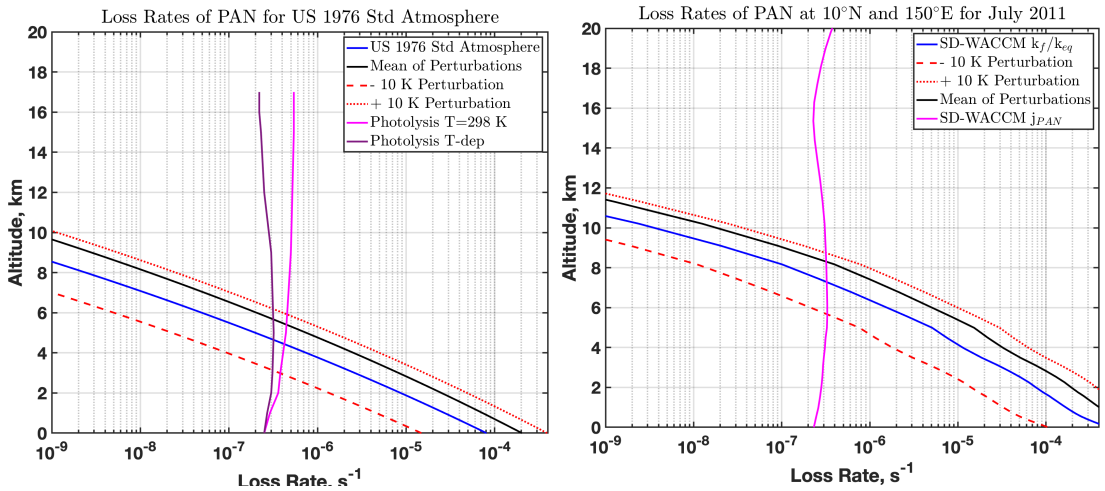

Figure 5-7: Atmospheric thermal decomposition and photolysis loss rate of PAN as a function of altitude. **(left)** Thermal decomposition rates for the US 1976 Standard Atmosphere temperature profile (blue) and that same profile with ±10 K perturbations (red dashed and dotted) are compared against the thermal decomposition rate calculated as the average of the perturbations. Two variations of the photolysis rate with height (teal and orange) are taken from Figure 6 of Talukdar et al., 1995. **(right)** The same but for the mean July 2011 tropical temperature profile at 10°N 150°E in the SD-WACCM model. The photolysis rate is calculated internally by the model.

photolysis becomes the dominant loss process higher by a kilometer or more. The right panel of Figure 5-7 shows the same but for a typical tropical summer profile over the Pacific Warm Pool, here represented by the mean July 2011 SD-WACCM temperature profile at 10°N, 150°E. The photolysis rate in the right panel is the model output for that month and grid-cell. While thermal decomposition dominates until higher in the atmosphere for the tropical profile compared with the US Standard Atmosphere, the effect of gravity wave perturbations is the same for both, with the warm perturbations dominating and skewing the thermal decomposition faster than it would be otherwise. All else being equal, this type of gravity wave activity will therefore tend to decrease the amount of PAN that makes it into the upper troposphere.

To see what effect this has on the full chemistry fields we look at the changing distribution of PAN over the course of several weeks in the GW and REF runs. Figure 5-8 shows the global distribution of PAN in the GW simulation for the 118 hPa (top) and 313 hPa (bottom) pressure levels for a series of four five-day increments from

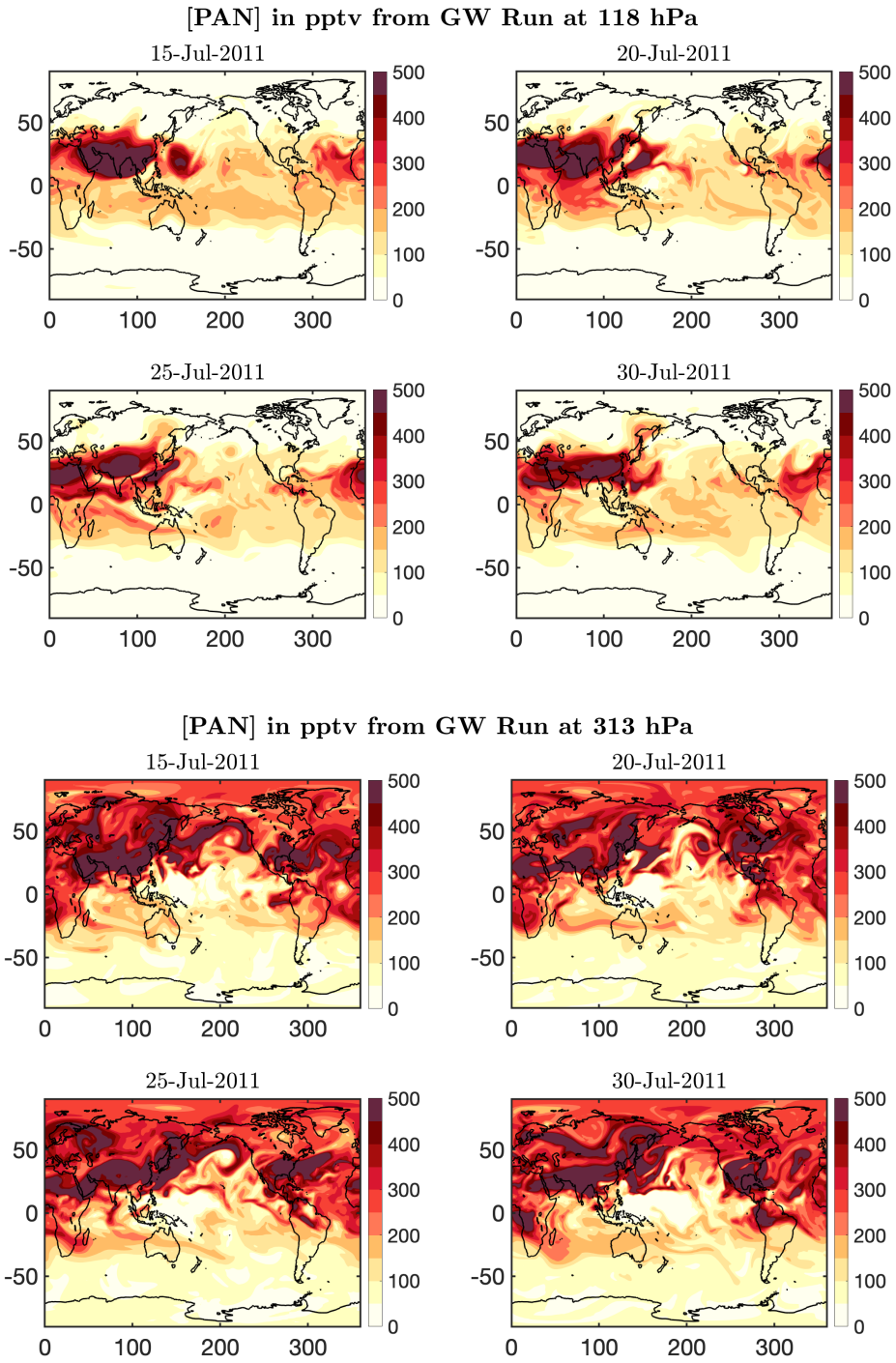

Figure 5-8: Global distribution of PAN on **(top)** the 118 hPa level and **(bottom)** the 313 hPa level in the SD-WACCM model over two weeks in July 2011. Note that 118mb is in the stratosphere in the polar regions but the upper troposphere in the tropics.

July 15 – July 30, 2011. The 118 mb level is located in the stratosphere for large portions of the globe, but is usually in the upper troposphere in the tropics. In general, PAN concentrations are larger over populated regions associated with high pollution such as India and China, but the transport effects can clearly be seen. The swirl of high values over the middle of the Pacific Ocean at 313 mb is a particularly striking example, and examination of the fields across panels confirms that this blob is transported from pollution hotspots over Asia.

Figure 5-9 shows the percentage changes in the GW simulation (5-8) compared to the reference simulation. Positive values correspond to increases in the mixing ratio of PAN in the GW simulation and thus imply a longer lifetime; negative values correspond to decreases and imply a shorter lifetime. While much of the globe shows small changes in either direction, the equatorial Pacific displays regions of strong but very localized increase, with adjacent regions showing strong local decreases as well on some days. Examination of the week-to-week evolution shows that some of the enhancement appears to originate over the Indonesian region and is transported across the Pacific, although there may also be hotspots near South America. At first pass this suggests that the new gravity wave linkage is implying farther transport of pollution from some sources in WACCM, which would be contrary to what would be expected from Figure 5-7. However, a more plausible explanation for at least some of this effect appears to be the differences in convection between the GW and REF runs. Although both are relaxed to MERRA-2 meteorology at the grid-scale level, sub-grid-scale convection is parameterized separately and can introduce chaotic fluctuations in otherwise identical tropical fields. Looking at precipitation fields in Figure 5-S1, which is a good marker of convection, it is apparent that the differences between the two runs, even in the monthly mean, are clustered around regions that also show large difference in PAN concentrations. It is likely that there is a combination of true gravity wave impacts and random convective changes at work here, but more investigation is needed. Future runs of multiple years are expected to help quantify the average magnitude of convective-induced variability for a given region and season, allowing us to isolate true changes to pollution transport from

gravity wave temperature perturbations.

5.5 Verification with Observations

The temperature perturbations from the gravity wave parameterization is not a field that WACCM typically outputs and must be derived from internal model quantities. Given this, there are no existing verifications for the value of T' for WACCM6 of which we are aware. Therefore, in order to have confidence in the previously discussed results, we must verify that the temperature perturbations being passed to the chemistry are in fact correct. To do this we compare the values from WACCM to dry temperature profiles derived from the Constellation Observing System for Meteorology, Ionosphere and Climate (COSMIC) micro-satellite array (UCAR COSMIC Program, 2006; Anthes et al., 2008). COSMIC is a joint US/Taiwanese mission that uses radio occultation receivers to measure dry temperature via the phase delay in GPS signals. The major advantages of COSMIC are its high sample rate, around 1500-2000 profiles distributed semi-randomly around the globe for the period under consideration here, and its high vertical resolution of 1 km or better in the stratosphere (Wright et al., 2011). While COSMIC has limited coverage over the poles, it has good coverage over the Andes, Rockies, and Tibetan Plateau regions in which we are interested.

There are several methods for extracting temperature perturbations from high resolution profiles. One commonly used technique (Wang & Geller 2003; Nath et al. 2009), is to fit a polynomial to each individual profile to get the background temperature, which is then subtracted from the original profile, leaving the perturbations. An example of this is given in Figure 5-10 using a second-order polynomial for a profile on January 1, 2010. This method is well-verified for finding gravity waves with wavelengths shorter than the fitting window, although it cannot account for larger waves (Wang & Geller 2003; Wang & Alexander, 2009). This is a particular problem in the winter over orography such as the Andes, where vertical wavelengths can be long (M. J. Alexander, personal communication). Indeed, when we compare

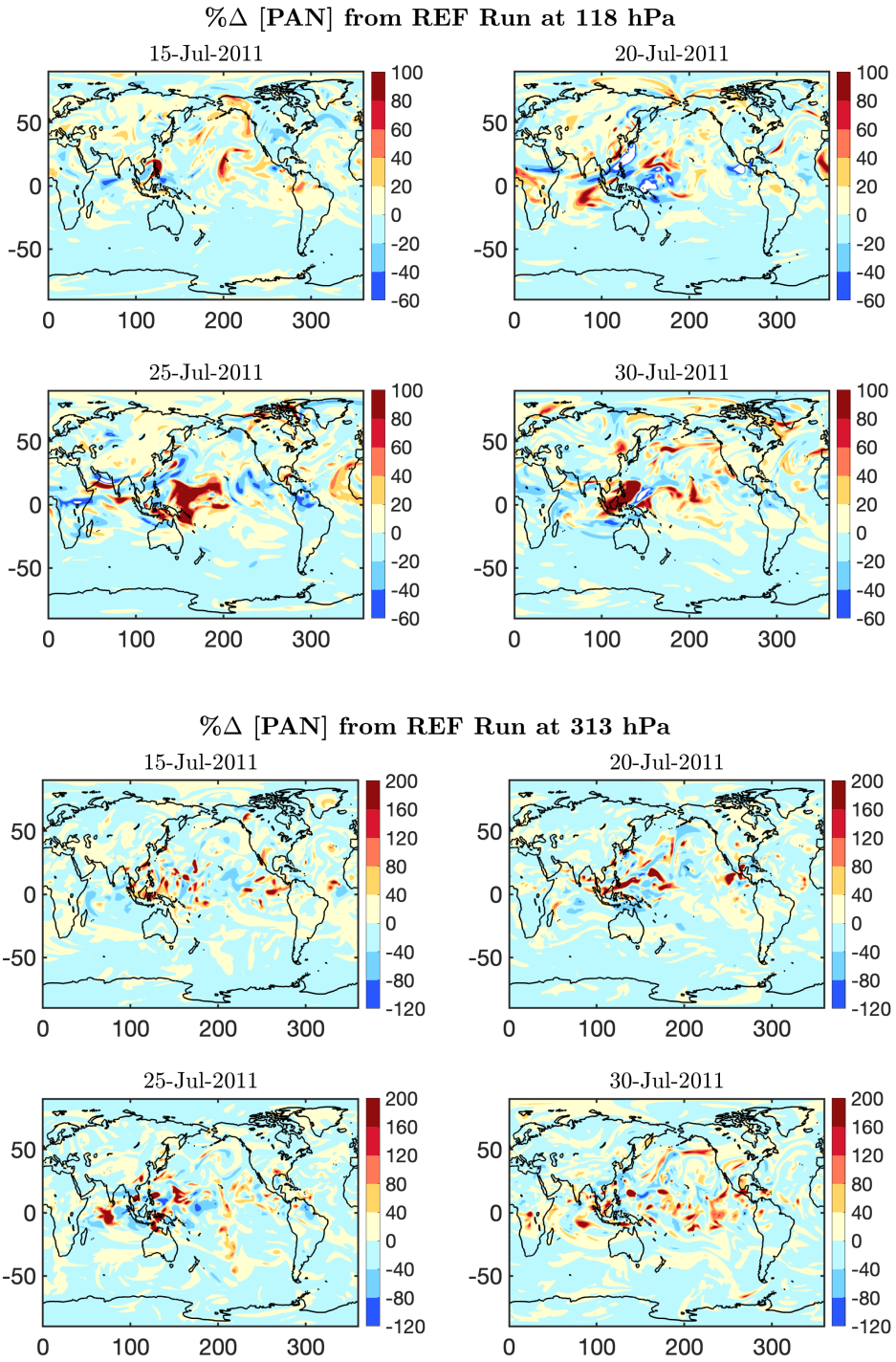

Figure 5-9: Global distribution of percentage change from reference run in PAN concentrations on **(top)** the 118 hPa level and **(bottom)** the 313 hPa level in the SD-WACCM model over two weeks in July 2011. Positive values correspond to increased concentrations in the GW run. Note the different colorbar scales.

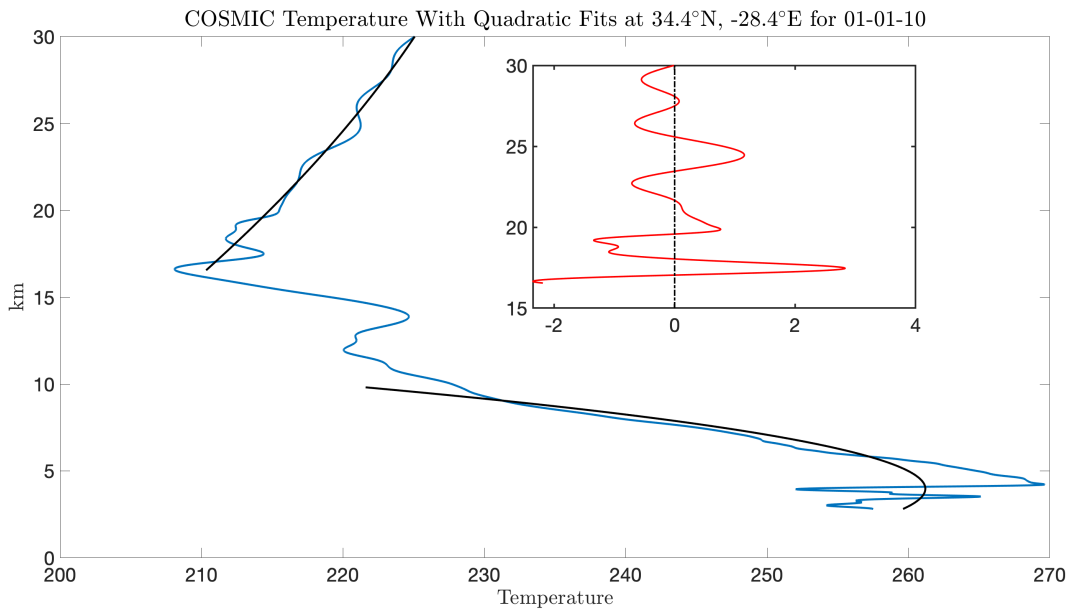

Figure 5-10: COSMIC dry temperature profile on January 1, 2010 with second-order polynomial fits and **(inset)** temperature perturbations from 17 km to 30 km altitude remaining after subtraction of the fitted profile.

distributions of the magnitude of temperature perturbations derived from polynomial fits to COSMIC data with WACCM's |T'| in the Andes box over 2010–2011, as shown in Figure 5-S2 and Table 5-1, it is apparent that the distribution matches fairly well in austral summer at the two higher levels but quite poorly in austral winter. There is also a poorer match to the 85 mbar level regardless of month, which may be due to the difficulty of obtaining good fits near the tropopause.

While the initial polynomial fit method appears to work well in summer months away from the tropopause, a more detailed approach is necessary for winter and other instances when gravity wave wavelengths are large. In such instances, temperature perturbations can be calculated by first finding and then subtracting a common mean background profile from multiple COSMIC measurements. A well-tested method for this is to bin COSMIC profiles into 10°× 15° latitude-longitude boxes, then perform an S-transform (a continuous wavelet-like analysis, see Stockwell et al., 1996) as a function of longitude for each latitude and altitude to obtain the zonal wavenumbers 0–6 to represent the background temperature. This background temperature is

interpolated back to the positions of the COSMIC profiles and subtracted from each profile as before to obtain temperature perturbations (Wang & Alexander, 2009; Wang & Alexander, 2010; Xu et al., 2018). Applying this technique to the 2010–2011 COSMIC data in the regions of interest will be the next phase of observational work and will indicate the reliability of WACCM's calculated large temperature perturbations.

Table 5-1: Statistical Properties of |Temperature Perturbation| Distributions seen in COSMIC and WACCM at 31 mb, 44 mb, and 85 mb within the Andes box. The 31 mb distributions are plotted in Figure 5-S2

Month	Mean 31mb	Std Dev 31mb	Mean 44mb	Std Dev 44 mb	Mean 85mb	Std Dev 85mb
			COSMIC			
Dec	1.72	1.63	2.72	1.46	2.43	0.914
Jan	1.20	0.689	2.36	1.55	2.20	0.820
Feb	1.34	1.75	2.00	1.10	2.06	0.909
Mar	1.59	1.71	2.58	2.20	2.07	0.735
Apr	2.27	1.15	2.78	1.11	2.74	1.31
May	2.31	1.71	2.33	0.869	2.73	1.52
Jun	1.80	0.642	2.40	0.928	2.47	1.18
Jul	1.90	0.917	2.68	1.48	2.84	1.38
Aug	1.75	0.890	2.52	2.67	2.28	1.38
Sep	1.74	1.54	2.00	1.01	2.06	1.02
Oct	1.68	1.18	2.03	0.911	2.08	0.781
Nov	1.60	1.16	1.93	0.906	2.16	1.08
			WACCM			
Dec	3.65	2.66	5.22	3.40	8.49	2.47
Jan	0.810	0.672	2.07	0.854	7.44	1.57
Feb	1.10	0.613	2.23	0.825	6.64	1.56
Mar	4.03	1.70	4.54	1.28	7.50	1.42
Apr	8.52	2.03	8.02	1.79	8.92	1.73
May	10.92	2.86	10.00	2.60	9.32	2.21
Jun	12.50	3.75	11.34	3.21	9.98	2.10
Jul	11.36	3.08	10.28	2.69	9.11	1.86
Aug	10.92	4.07	9.78	3.54	8.74	2.11
Sep	12.54	4.23	11.24	3.56	9.24	2.26
Oct	11.31	5.18	10.01	3.99	8.45	2.08
Nov	8.43	4.40	8.33	3.73	8.00	2.16

5.6 Conclusions

We have successfully connected the orographic gravity wave parameterization to the chemistry module in the WACCM6 model for the first time by subcycling the chemistry through a temperature perturbation passed from the gravity wave parameterization. Preliminary analysis suggests that there are significant short-term changes in chemistry for both stratospheric heterogeneous reactions and potentially also tropospheric transport of pollutants. Furthermore, the changes in chlorine activation are large and sufficiently persistent to be seen in monthly-mean fields. Time series over the Antarctic Peninsula in SD-WACCM and MLS show better agreement when this new linkage is included, and the type of aircraft-based ClO observations described in Chapter 3 in the tropics could also distinguish between the reference and gravity wave enhanced cases.

As the chemical impacts of gravity wave temperature perturbations depend upon both the magnitude of T' and the background temperature, regions with relatively warm background temperatures and large-amplitude waves (such as the Andes) often do not exhibit as large of changes in activation as regions with colder background temperatures and smaller amplitude waves (such as the monsoonal region and the edge of the polar vortex). Given the cold temperatures seen in the deep tropics near the tropopause, the impacts of Matsuno-Gill circulations on heterogeneous chemistry described in Chapter 3 are expected to be very sensitive to gravity wave perturbations. However, as much of the gravity wave in that region comes from convection rather than orography, full investigation must wait until the convective gravity wave source parameterization can be connected to the chemistry as well as the orographic one. Finally, the magnitude of the temperature perturbations WACCM is now passing to the chemistry is in the process of being verified by comparison to COSMIC. Should this process show that the temperature perturbations are too large, as is known to be the case for the unadjusted momentum deposition, the derivation will need to be modified or scaled. Once temperature perturbation magnitudes are satisfactory, we will assess the computational cost of the current implementation and decide if a more efficient method is worth pursuing.

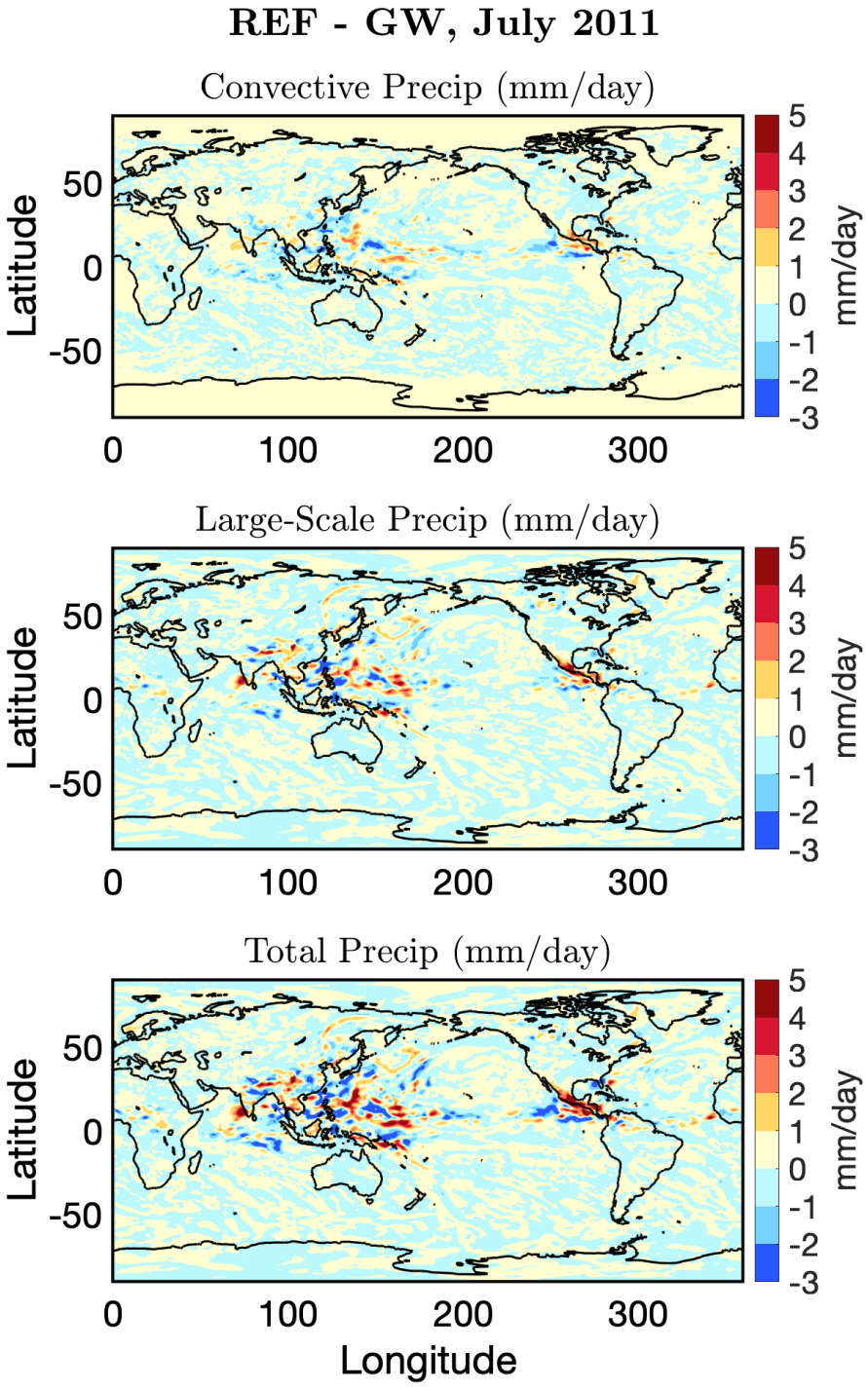

Figure 5-S1: Global distribution of precipitation change in mm/day for July 2011 between the REF and GW runs for **(top)** convective precipitation, **(middle)** large-scale precipitation, and **(bottom)** total precipitation fields.

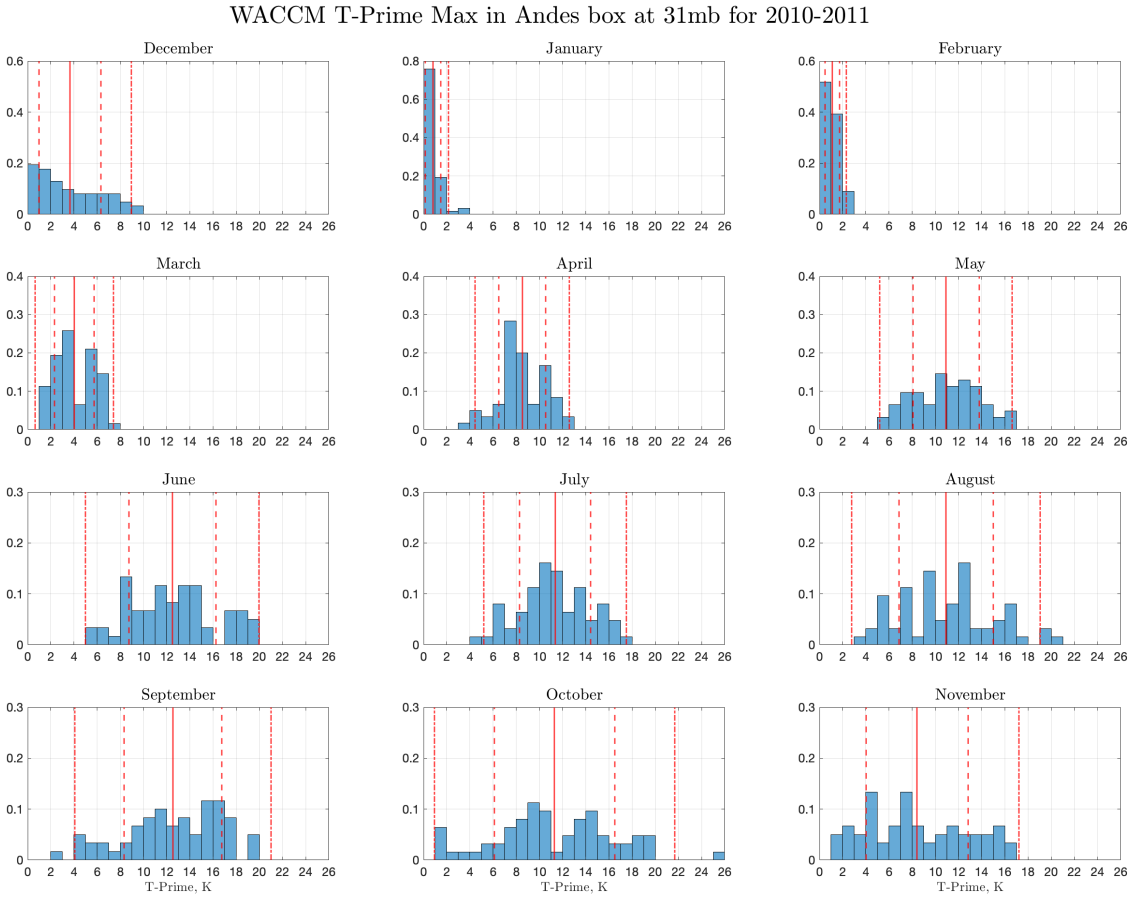

Figure 5-S2: Probability distributions of |T'| in **(top)** WACCM and **(bottom, next page)** COSMIC. Each month contains profiles from both 2010 and 2011 for the Andes box defined in Figure 5-1 at 31 mb. Solid red lines indicate the means; dashed lines indicate ±1 standard deviation and dot-dashed lines indicate ±2 standard deviations.

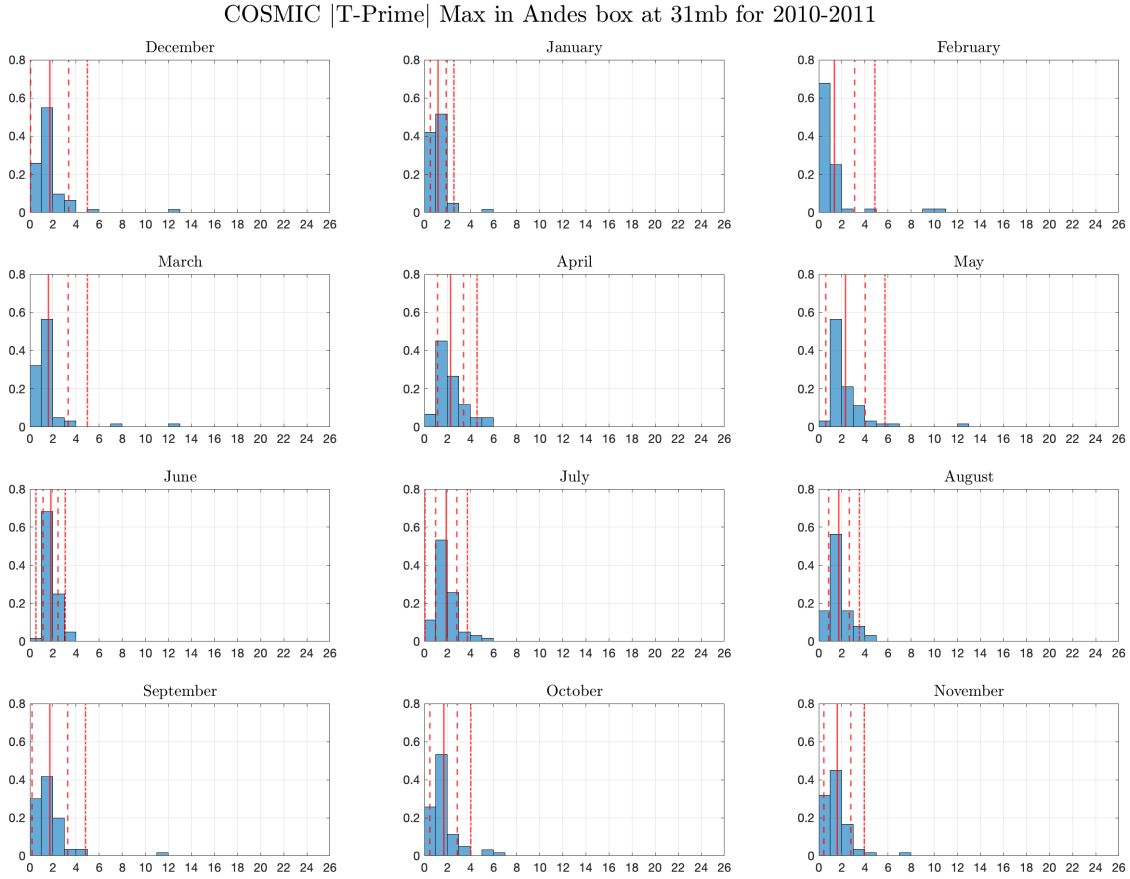

Figure 5-S2: (continued from previous page)Probability distributions of |T'| in **(top, previous page)** WACCM and **(bottom)** COSMIC. Each month contains profiles from both 2010 and 2011 for the Andes box defined in Figure 5-1 at 31 mb. Solid red lines indicate the means; dashed lines indicate ±1 standard deviation and dot-dashed lines indicate ±2 standard deviations.

References

[1] Anthes, R. A., Bernhardt, P. A., Chen, Y., Cucurull, L., Dymond, K. F., Ector, D., ... & Zeng, Z. (2008). The COSMIC/FORMOSAT-3 mission: Early results. *Bulletin of the American Meteorological Society, 89*(3), 313–334. https://doi.org/10.1175/BAMS-89-3-313

[2] Bacmeister, J. T. (1993). Mountain-wave drag in the stratosphere and mesosphere inferred from observed winds and a simple mountain-wave parameterization scheme. *Journal of Atmospheric Sciences, 50*(3), 377–399. https://doi.org/10.1175/1520-0469(1993)050<0377:MWDITS>2.0.CO;2

[3] Beres, J. H., Garcia, R. R., Boville, B. A., & Sassi, F. (2005). Implementation of a gravity wave source spectrum parameterization dependent on the properties of convection in the Whole Atmosphere Community Climate Model (WACCM). *Journal of Geophysical Research: Atmospheres, 110*(D10). https://doi.org/10.1029/2004JD005504

[4] Carslaw, K. S., Wirth, M., Tsias, A., Luo, B. P., Dörnbrack, A., Leutbecher, M., ... & Peter, T. (1998). Increased stratospheric ozone depletion due to mountain-induced atmospheric waves. *Nature, 391*(6668), 675–678. https://doi.org/10.1038/35589

[5] Fritts, D. C., & Alexander, M. J. (2003). Gravity wave dynamics and effects in the middle atmosphere. *Reviews of Geophysics, 41*(1). https://doi.org/10.1029/2001RG000106

[6] Garcia, R. R., Smith, A. K., Kinnison, D. E., de la Cámara, Á., & Murphy, D. J. (2017). Modification of the gravity wave parameterization in the Whole Atmosphere Community Climate Model: Motivation and results. *Journal of Atmospheric Sciences, 74*(1), 275–291.https://doi.org/10.1175/JAS-D-16-0104.1

[7] McFarlane, N. A. (1987). The effect of orographically excited gravity wave drag on the general circulation of the lower stratosphere and troposphere. *Journal of Atmospheric Sciences, 44*(14), 1775–1800. https://doi.org/10.1175/1520-0469(1987)044<1775:TEOOEG>2.0.CO;2

[8] Moore, D. P., & Remedios, J. J. (2010). Seasonality of Peroxyacetyl nitrate (PAN) in the upper troposphere and lower stratosphere using the MIPAS-E instrument. *Atmospheric Chemistry and Physics, 10*(13), 6117–6128. https://doi.org/10.5194/acp-10-6117-2010

[9] Murphy, D. M., & Ravishankara, A. R. (1994). Temperature averages and rates of stratospheric reactions. *Geophysical Research Letters, 21*(23), 2471–2474. https://doi.org/10.1029/94GL02287

[10] Nath, D., Venkat Ratnam, M., Jagannadha Rao, V. V. M., Krishna Murthy, B. V., & Vijaya Bhaskara Rao, S. (2009). Gravity wave characteristics observed over a tropical station using high-resolution GPS radiosonde soundings. *Journal of Geophysical Research: Atmospheres, 114*(D6). https://doi.org/10.1029/2008JD011056

[11] Orr, A., Hosking, J. S., Hoffmann, L., Keeble, J., Dean, S. M., Roscoe, H. K., ... & Braesicke, P. (2015). Inclusion of mountain-wave-induced cooling for the formation of PSCs over the Antarctic Peninsula in a chemistry–climate model. *Atmospheric Chemistry and Physics, 15*(2), 1071–1086. https://doi.org/10.5194/acp-15-1071-2015

[12] Richter, J. H., Sassi, F., & Garcia, R. R. (2010). Toward a physically based gravity wave source parameterization in a general circulation model. *Journal of the Atmospheric Sciences, 67*(1), 136–156. https://doi.org/10.1175/2009JAS3112.1

[13] Scinocca, J. F., & McFarlane, N. A. (2000). The parametrization of drag induced by stratified flow over anisotropic orography. *Quarterly Journal of the Royal Meteorological Society, 126*(568), 2353–2393. https://doi.org/10.1002/qj.49712656802

[14] Solomon, S., Kinnison, D., Garcia, R. R., Bandoro, J., Mills, M., Wilka, C., ... & Höpfner, M. (2016). Monsoon circulations and tropical heterogeneous chlorine chemistry in the stratosphere. *Geophysical Research Letters, 43*(24), 12–624. https://doi.org/10.1002/2016GL071778

[15] Stockwell, R. G., Mansinha, L., & Lowe, R. P. (1996). Localization of the complex spectrum: the S transform. *IEEE Transactions on Signal Processing, 44*(4), 998–1001. https://doi.org/10.1109/78.492555

[16] Talukdar, R. K., Burkholder, J. B., Schmoltner, A. M., Roberts, J. M., Wilson, R. R., & Ravishankara, A. R. (1995). Investigation of the loss processes for peroxyacetyl nitrate in the atmosphere: UV photolysis and reaction with OH. *Journal of Geophysical Research: Atmospheres, 100*(D7), 14163–14173. https://doi.org/10.1029/95JD00545

[17] UCAR COSMIC Program, 2006: COSMIC-1 Data Products Level 2. UCAR/NCAR – COSMIC, Access date March 15, 2021. https://doi.org/10.5065/ZD80-KD74

[18] Wang, L., & Alexander, M. J. (2009). Gravity wave activity during stratospheric sudden warmings in the 2007–2008 Northern Hemisphere winter. *Journal of Geophysical Research: Atmospheres, 114*(D18). https://doi.org/10.1029/2009JD011867

[19] Wang, L., & Alexander, M. J. (2010). Global estimates of gravity wave parameters from GPS radio occultation temperature data. *Journal of Geophysical Research: Atmospheres, 115*(D21). https://doi.org/10.1029/2010JD013860

[20] Wang, L., & Geller, M. A. (2003). Morphology of gravity-wave energy as observed from 4 years (1998–2001) of high vertical resolution US radiosonde data. *Journal of Geophysical Research: Atmospheres, 108*(D16). https://doi.org/10.1029/2002JD002786

[21] Waters, J. W., Froidevaux, L., Harwood, R. S., Jarnot, R. F., Pickett, H. M., Read, W. G., ... & Walch, M. J. (2006). The earth observing system microwave limb sounder (EOS MLS) on the Aura satellite. *IEEE Transactions on Geoscience and Remote Sensing, 44*(5), 1075–1092. https://doi.org/10.1109/TGRS.2006.873771

[22] Weimer, M., Buchmüller, J., Hoffmann, L., Kirner, O., Luo, B., Ruhnke, R., ... & Braesicke, P. (2020). Mountain-wave induced polar stratospheric clouds and their representation in the global chemistry model ICON-ART. *Atmospheric Chemistry and Physics Discussions*, 1–42. https://doi.org/10.5194/acp-2020-1156

[23] Wiegele, A., Glatthor, N., Höpfner, M., Grabowski, U., Kellmann, S., Linden, A., ... & Clarmann, T. V. (2012). Global distributions of C_2H_6, C_2H_2, HCN, and PAN retrieved from MIPAS reduced spectral resolution measurements. *Atmospheric Measurement Techniques, 5*(4), 723–734. https://doi.org/10.5194/amt-5-723-2012

[24] Wright, C. J., Rivas, M. B., & Gille, J. C. (2011). Intercomparisons of HIRDLS, COSMIC and SABER for the detection of stratospheric gravity waves. *Atmospheric Measurement Techniques, 4*(8), 1581–1591. https://doi.org/10.5194/amt-4-1581-2011

[25] Xu, X., Yu, D., & Luo, J. (2018). The spatial and temporal variability of global stratospheric gravity waves and their activity during sudden stratospheric warming revealed by COSMIC measurements. *Advances in Atmospheric Sciences, 35*(12), 1533–1546. https://doi.org/10.1007/s00376-018-5053-1

[26] Zou, L., Hoffmann, L., Griessbach, S., Spang, R., & Wang, L. (2021). Empirical evidence for deep convection related stratospheric cirrus clouds over North

America. *Atmospheric Chemistry and Physics Discussions,* 1–30. https://doi.org/10.5194/acp-2021-90

Chapter 6

Future Work and Conclusions

In this chapter I describe the most important avenues for future work building upon the findings of this thesis, with the exception of the gravity wave work in Chapter 5, as that has already been discussed. I finish this chapter, and this thesis, with a summary of the most important findings and a brief reflections.

6.1 Observing Chlorine Activation in the Tropical Upper Troposphere Lower Stratosphere

One of the most significant findings of Chapter 3 was the double bulls-eye of enhanced ClO over the tropical Pacific that is only present with heterogeneous chemistry. This can act as a spatial fingerprint: if observations were to detect similar structures in the fall or spring, it would be very strong evidence for heterogeneous chlorine activation. Unfortunately, observations of ClO in the region in question are sparse. The levels of enhancement, of order a few tens of pptv, are much lower than the sensitivity of any satellite that measures it. Aircraft campaigns, which could almost certainly observe those levels, are limited in the tropical stratosphere in general, and even more rarely measure ClO. $ClONO_2$, which provided a good indicator of chlorine activation in the monsoon region in Solomon et al., 2016, has similar limitations.

Species in the NO_y family may provide a better target for observation in the tropical UTLS. Depletion of NO_2 has already been shown to be a possibility (Figure 3-4b). Despite NO_2's higher background concentrations, however, there are still no satellites with sufficiently high spatial resolution in the tropics to reliably observe it. This is due in part to the geographic coverage of recent chemistry-focused satellites, and in part to the fact that lower stratospheric retrievals in the tropics are frequently contaminated by the presence of high clouds. However, HNO_3 shows more promise. As can be seen in Figure 6-1, runs with and without tropical heterogeneous chemistry in WACCM4 (Chem-Dyn-Vol and NoHet40NS; these are the same ones used in Chapter 3) in July 2011 are visually distinct, with mixing ratios around the EASM's anticyclone several hundred pptv higher in the presence of heterogeneous chemistry.

This difference can be quantified by analyzing the distribution of values within a chosen geographic range, and the resulting PDFs are visually well-separated (Figure 6-2), with the Chem-Dyn-Vol run peaking at higher value than the NoHet40NS run ever reaches. Unfortunately, observations from the MIPAS satellite (Clarmann et al., 2009) fall between the two distributions and don't clearly indicate which one is correct, with both the range and shape heavily dependent on the resolution the instrument is binned to. It's difficult to tell *a priori* if this is due to the model being incorrect, the data having an offset, or the data being noisy. However, recent work by Zambri et al., 2020 in the subpolar regions demonstrated that finding the underlying statistical distribution functions that best match different data and model runs is able to account for offset data and can help in distinguishing when chlorine activation is present. WACCM6 recently updated its set of MIPAS colocated profiles as well, which would help to eliminate spatial differences between the model and observations.

The combination of the updated model and new analysis techniques justify a fresh examination of whether old instruments were able to observe tropical chlorine activation as simulated by Solomon et al, 2016 and Wilka et al., 2021. Finally, if the new gravity wave connection results in significant increases in tropical or subtropical chlorine activation, those studies should be revisited to see what magnitude of response we might expect to find in observational data.

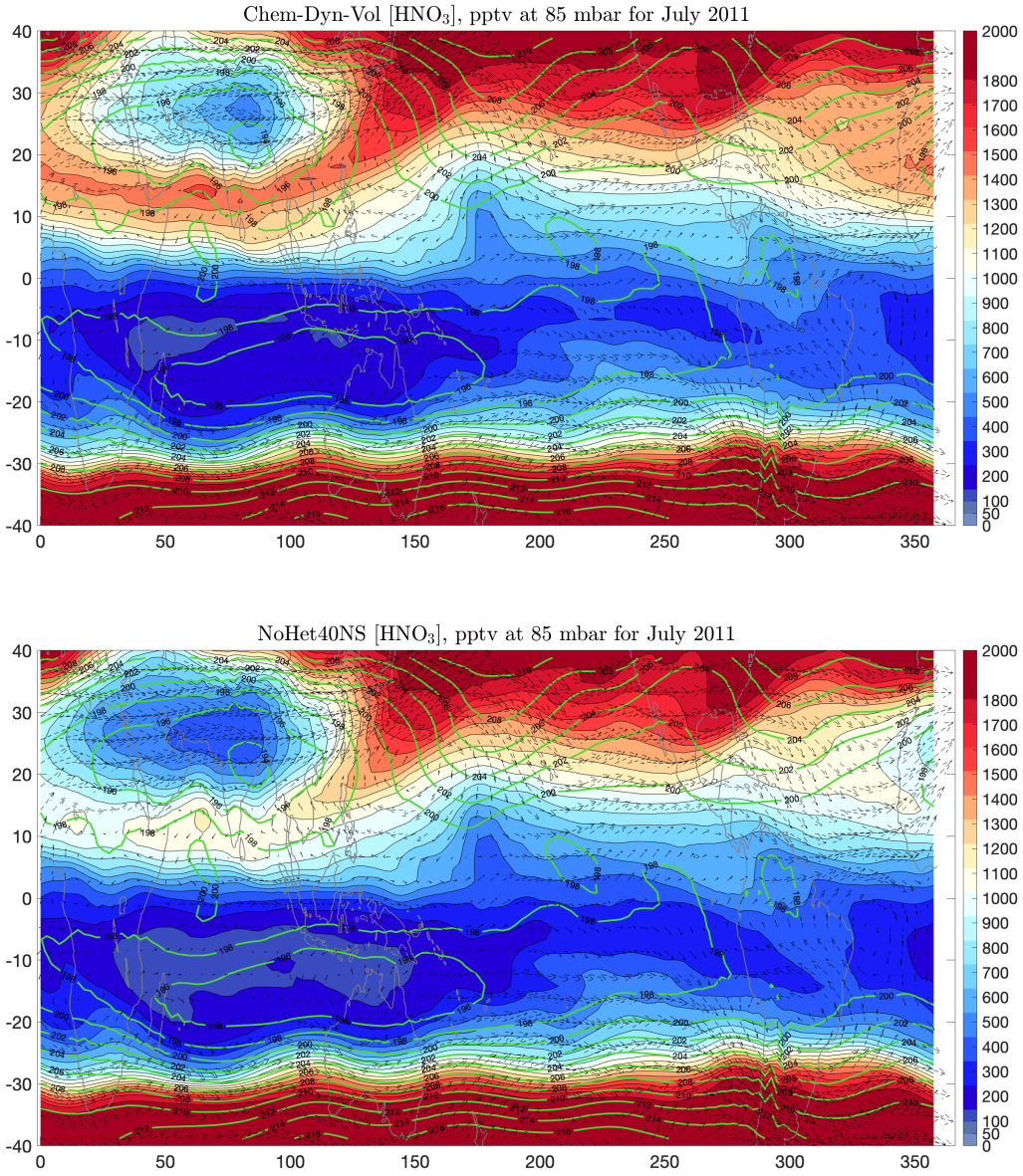

Figure 6-1: Distribution of HNO_3 for July 2011 at 85 mbar in the SD-WACCM4 model **(top)** with all heterogeneous chemical reactions turned on and **(bottom)** with chlorine heterogeneous chemical reactions turned off between 40°N and 40°S. Details of the simulations are given in Chapter 3.

6.2 Refining WACCM's NAT Parameterization

In Chapter 4, SD-WACCM6's denitrification proved too sluggish to accurately simulate the extreme Arctic ozone depletion in the spring of 2020. To remedy this, we

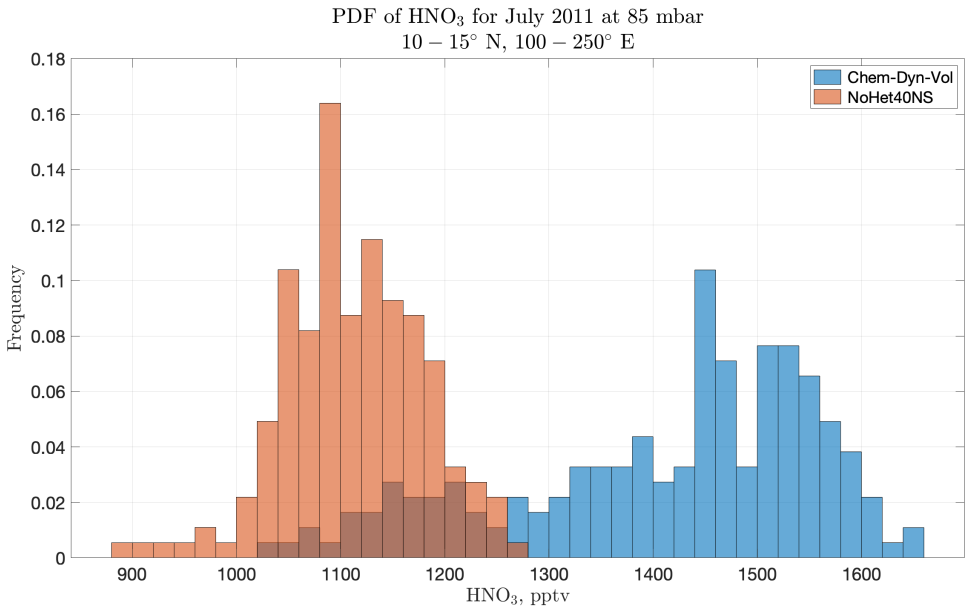

Figure 6-2: Frequency of HNO_3 concentrations, normalized, for July 2011 at 85 mb in Chem-Dyn-Vol vs NoHet40NS. Details of these simulations are given in Chapter 3.

increased the size of the NAT particles, causing more HNO_3 to sediment out of the stratosphere and preventing NO_2 from recombining with ClO and short-circuiting ozone depletion too early. The new NAT parameterization works well when the Arctic experiences extremely cold temperatures and stable vortex (such as in 2020 and 2011), but we have not fully tested it against average conditions, or against years with anomalously warm conditions. Furthermore, while we examined several profiles in the Southern Hemisphere and compared them to ozonesondes launched at Syowa Station (as in the right panel of Figure 4-6), and found the ozone depletion levels satisfactory, we have not yet carried out a systematic assessment of the new parameterization on Antarctic ozone depletion.

Following the procedure from Chapter 4, we begin by looking at HNO_3 maps over the Antarctic from different denitrification runs and comparing those against MLS observations. In Figure 6-3 we look at August 1, 2019, as ozone depletion was getting underway and before the sudden stratospheric warming (SSW) that dominated the ozone evolution of that year occurred. While MLS's coverage is patchy, the deep

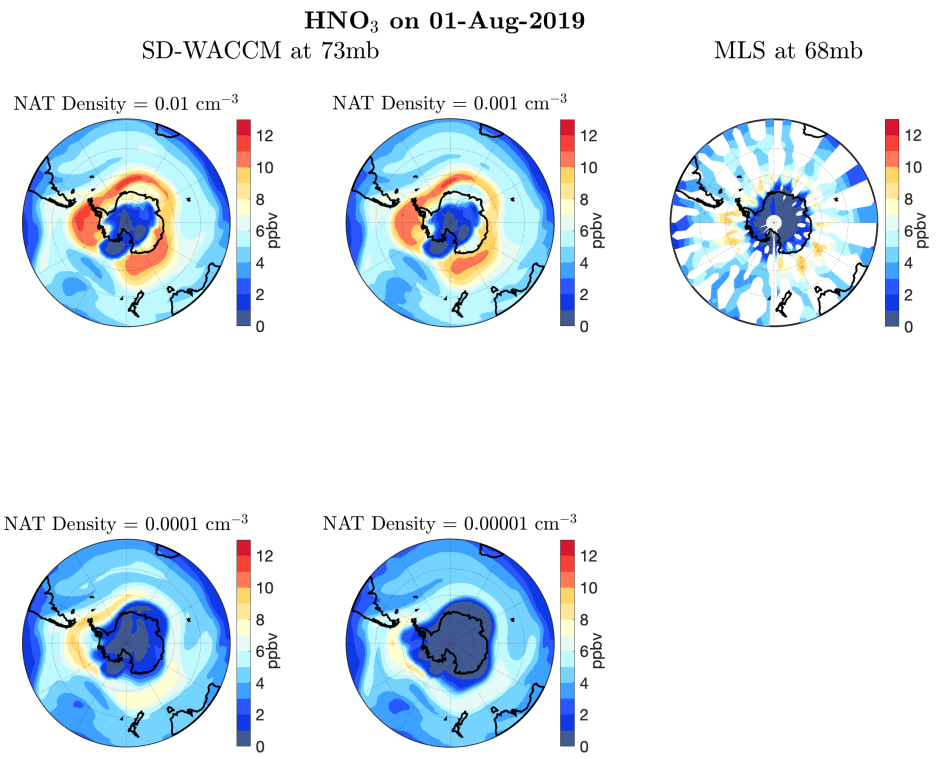

Figure 6-3: HNO_3 in ppbv for August 1, 2019, for different NAT parameterizations in SD-WACCM **(a-d)** compared to MLS **(e)**. In order of increasing denitrification, the NAT density is **(a)** 0.01 cm^{-3}, **(b)** 0.001 cm^{-3}, **(c)** 0.0001 cm^{-3}, and **(d)** 0.00001 cm^{-3}. Panel **(a)** shows the previous standard SD-WACCM NAT parameter value and panel **(d)** shows the parameter value ultimately used in the RW and WA simulations. All SD-WACCM figures show the 73 mb level; MLS shows the 68 mb level.

denitrification over Antarctica itself compares better to the two more-denitrified simulations. The ring of high HNO_3 around the edge of the vortex looks most similar to the run with a NAT density of 0.00001 cm^{-3} (the third-most denitrified).

Looking forward in time to HNO_3 maps for September 1st in Figure 6-4, both of the higher denitrification runs now seem to be over-denitrifying. MLS appears to fall between the second and third most denitrified runs for October 1st in Figure 6-5. While the NAT parameter that matches MLS appears to shift depending on how far into the austral spring we look, it is clear for all of these days that WACCM's

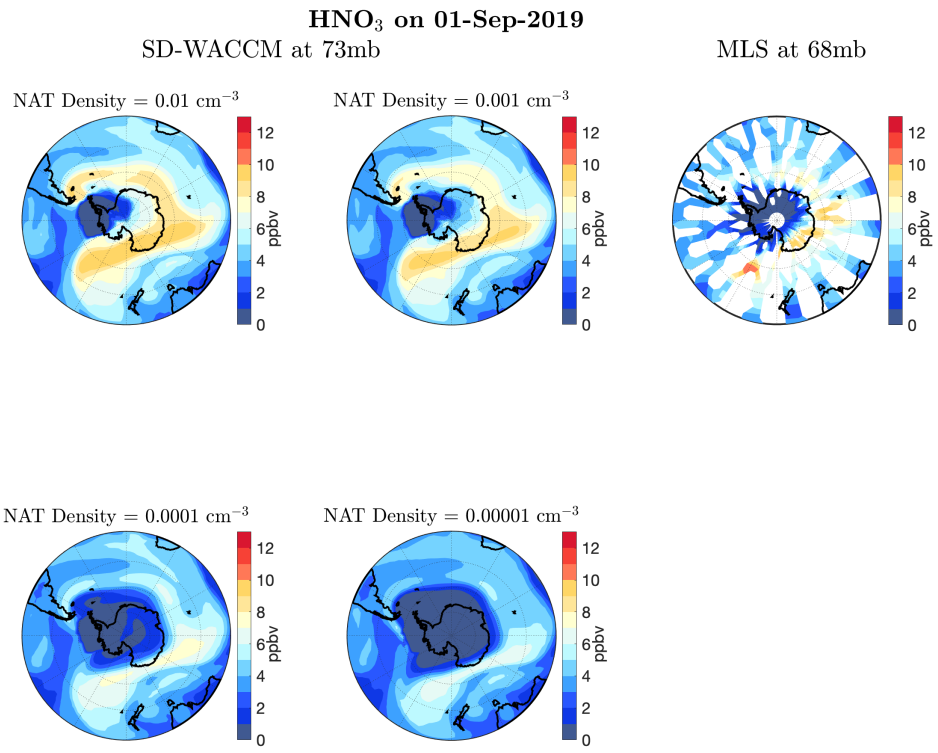

Figure 6-4: As in Figure 6-3 but for September 1, 2019.

previous NAT parameterization denitrifies too little. This helps confirm that we have implemented a needed change in the model, although the final parameter value may not be the same as used in Chapter 4. Furthermore, as cooling rates matter along with absolute temperatures in determining rates of NAT formation (Toon et al., 1986; Fahey et al., 2001), it is possible that different parameter values are needed for the different hemispheres.

Two additional important caveats to keep in mind are: (1) that MLS itself has a coarse averaging kernel and at times large uncertainties, and (2) this year, as previously stated, experienced a rare Southern Hemisphere SSW, and so in its own way is also very atypical (de Laat and van Weele, 2011; Safieddine et al., 2020). To address the first we will also look at data from a range of Antarctic ozonesonde stations as well as MLS, and to address the second we will examine more years. This will be the subject of immediate followup work.

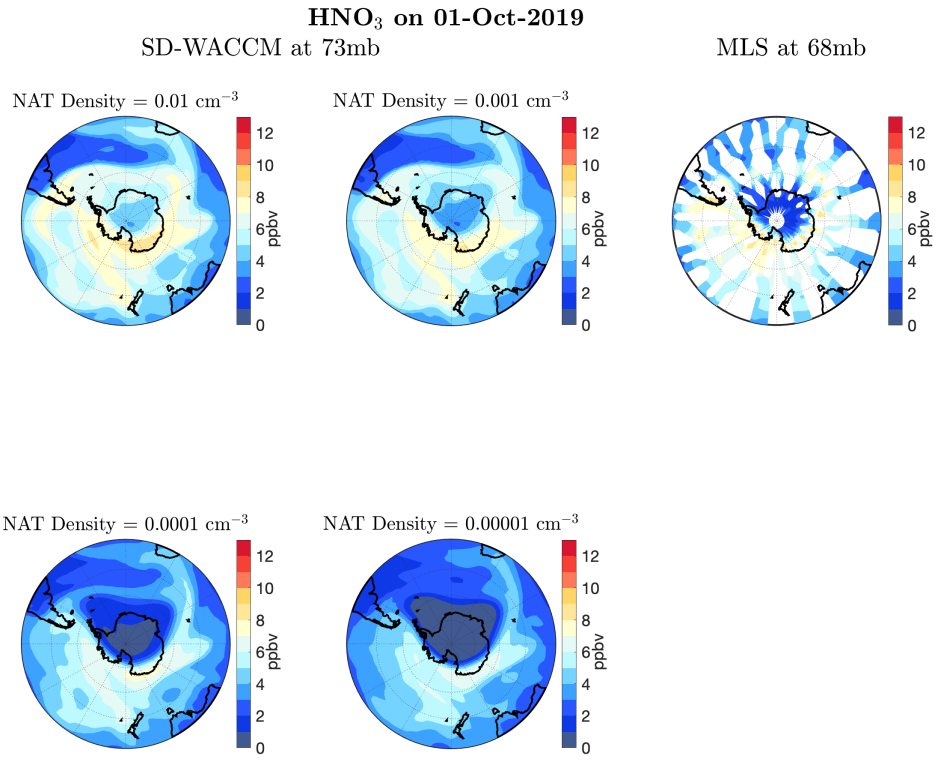

Figure 6-5: As in Figure 6-3 but for October 1, 2019.

6.3 Conclusions

This thesis has expanded our knowledge of the interactions between natural variability and anthropogenic trends, refined the representation of multiple key processes in a cutting-edge climate model, and assessed the impact of a major international environmental treaty.

In Chapter 2, I investigated how volcanic aerosols modulated anthropogenically driven ozone trends. I found that one must account for both large and moderate-sized eruptions in order to accurately model this important form of natural variability. I showed that a period of volcanic quiescence at the beginning of the ozone recovery period and a flurry of moderate-sized eruptions a decade later acted like a seesaw on the recovery trend, raising its rate at the start and depressing it toward the end of the time period under consideration. This study helped to put large variations in the rate of ozone healing into context, and helped show that periods of slower recovery are to be expected.

In Chapter 3, I extended our knowledge of the temporal and geographical range over which heterogeneous reactions can activate chlorine by tracing well-known tropical dynamics circulations through to their effects on stratospheric chemistry. I demonstrated a previously unknown pathway for dynamical influence on chemical composition in the tropical UTLS, and provided a clear target for attempts to observe these reactions using multiple chemical species, some potential ways of which are described in this chapter.

In Chapter 4, I assessed the effectiveness of the Montreal Protocol by examining how much more ozone depletion we would have seen in its absence. I showed that, without the protocol, we would have seen the first genuine Arctic ozone hole, which would have exposed the rich Arctic ecosystem and a large human population to increased UV levels. As part of this study, I compared ozone and nitric acid in the WACCM6 model to satellite and balloon-based data and helped to improve the model's representation of denitrification for extremely cold years. Possible further refinements to this parameterization are discussed earlier in this chapter and will be the subject of future work.

In Chapter 5, I examined the impact on chemistry in the WACCM6 model from connecting the gravity wave parameterization to the chemical module for the first time. I investigated the sensitivity of both stratospheric chlorine activation chemistry and tropospheric pollution transport to temperature perturbations, and found important differences from the reference case in both daily time series and monthly means. Finally, I began to compare both the chlorine chemistry response and the temperature perturbations themselves to satellite data.

My work is driven by a desire to better understand the fundamental science behind policy-relevant issues, and by a belief that the best science takes place when we care deeply about both the process of and the motivation behind our work. To quote Rosalind Franklin, "science and everyday life cannot and should not be separated." As anthropogenic threats to the biosphere such as ozone depletion and climate change disproportionately impact the most vulnerable communities, ensuring that policy is based on sound science is a vital component of environmental justice.

References

[1] Clarmann, T. V., Höpfner, M., Kellmann, S., Linden, A., Chauhan, S., Funke, B., ... & Versick, S. (2009). Retrieval of temperature, H_2O, O_3, HNO_3, CH_4, N_2O, $ClONO_2$ and ClO from MIPAS reduced resolution nominal mode limb emission measurements. *Atmospheric Measurement Techniques, 2*(1), 159–175. https://doi.org/10.5194/amt-2-159-2009

[2] Fahey, D. W., Gao, R. S., Carslaw, K. S., Kettleborough, J., Popp, P. J., Northway, M. J., ... & Von König, M. (2001). The detection of large HNO_3-containing particles in the winter Arctic stratosphere. *Science, 291*(5506), 1026–1031.https://doi.org/10.1126/science.1057265

[3] De Laat, A. T. J., & Van Weele, M. (2011). The 2010 Antarctic ozone hole: Observed reduction in ozone destruction by minor sudden stratospheric warmings. *Scientific Reports, 1*(1), 1–8. https://doi.org/10.1038/srep00038

[4] Safieddine, S., Bouillon, M., Paracho, A. C., Jumelet, J., Tence, F., Pazmino, A., ... & Clerbaux, C. (2020). Antarctic ozone enhancement during the 2019 sudden stratospheric warming event. *Geophysical Research Letters, 47*(14), e2020GL087810. https://doi.org/10.1029/2020GL087810

[5] Solomon, S., Kinnison, D., Garcia, R. R., Bandoro, J., Mills, M., Wilka, C., ... & Höpfner, M. (2016). Monsoon circulations and tropical heterogeneous chlorine chemistry in the stratosphere. *Geophysical Research Letters, 43*(24), 12–624. https://doi.org/10.1002/2016GL071778

[6] Toon, O. B., Hamill, P., Turco, R. P., & Pinto, J. (1986). Condensation of HNO_3 and HCl in the winter polar stratospheres. *Geophysical Research Letters, 13*(12), 1284–1287. https://doi.org/10.1029/GL013i012p01284

[7] Wilka, C., Solomon, S., Cronin, T. W., Kinnison, D., & Garcia, R. (2021). Atmospheric Chemistry Signatures of an Equatorially Symmetric Matsuno–Gill Circulation Pattern. *Journal of the Atmospheric Sciences, 78*(1), 107–116. https://doi.org/10.1175/JAS-D-20-0025.1

[8] Zambri, B., Kinnison, D. E., & Solomon, S. (2020). Subpolar activation of halogen heterogeneous chemistry in austral spring. *Geophysical Research Letters,* e2020GL090036. https://doi.org/10.1029/2020GL090036